Investigation of performance of oxide and TMD based photodetecting structures

Ph.D. Thesis

By

RUCHI SINGH

DEPARTMENT OF ELECTRICAL ENGINEERING

INDIAN INSTITUTE OF TECHNOLOGY INDORE

DECEMBER 2022

Investigation of performance of oxide and TMD based photodetecting structures

A THESIS

Submitted in partial fulfillment of the
requirements for the award of the degree
of
DOCTOR OF PHILOSOPHY

by

RUCHI SINGH

DEPARTMENT OF ELECTRICAL ENGINEERING
INDIAN INSTITUTE OF TECHNOLOGY INDORE
DECEMBER 2022

INDIAN INSTITUTE OF TECHNOLOGY INDORE

I hereby certify that the work which is being presented in the thesis entitled **INVESTIGATION OF PERFORMANCE OF OXIDE AND TMD BASED PHOTODETECTING STRUCTURES** in the partial fulfillment of the requirements for the award of the degree of **DOCTOR OF PHILOSOPHY** and submitted in the **DEPARTMENT OF ELECTRICAL ENGINEERING, Indian Institute of Technology Indore**, is an authentic record of my own work carried out during the time period from December, 2017 to December, 2022 under the supervision of Prof. Shaibal Mukherjee, Professor, Department of Electrical Engineering, Indian Institute of Technology Indore and Dr. Pankaj Misra, Scientist G, RRCAT Indore.

The matter presented in this thesis has not been submitted by me for the award of any other degree of this or any other institute.

06/10/2023

Signature of the student with date
(RUCHI SINGH)

This is to certify that the above statement made by the candidate is correct to the best of my/our knowledge.

06/10/2023

Signature of Thesis Supervisor #1 with date
(PROF. SHAIBAL MUKHERJEE)

06/10/2023

Signature of Thesis Supervisor #2 with date
(DR. PANKAJ MISRA)

RUCHI SINGH has successfully given his/her Ph.D. Oral Examination held on **06/10/2023**.

06/10/2023

Signature of Thesis Supervisor #1 with date
(PROF. SHAIBAL MUKHERJEE)

06/10/2023

Signature of Thesis Supervisor #2 with date
(DR. PANKAJ MISRA)

ACKNOWLEDGEMENTS

First of all, I would like to express my sincere appreciation to my thesis supervisor **Prof. Shaibal Mukherjee**, Associate Professor, Department of Electrical Engineering IIT Indore, and **Dr. Pankaj Misra**, Scientific Officer/G, Raja Ramanna Centre for Advanced Technology, Indore for his generous guidance, support, monitoring, constant encouragement, timely suggestions and the detailed discussion without which this work would not have been possible. He consistently allowed this thesis to be my own work, but he steered me in the right direction whenever he thought I needed it.

I am extremely grateful to my doctoral committee members **Prof. Vimal Bhatia** and **Prof. Abhirup Datta** for their encouragement, valuable advice, questions, insightful comments and co-operation throughout the work.

My sincere thanks go to **Prof. Suhas S. Joshi**, Director, IIT Indore for providing the essential experimental facilities. I want to acknowledge the support provided by sophisticated instrumentation center (SIC) at IIT Indore, for performing XRD, SEM, and EDX measurements.

My sincere appreciation to **Dr. Vinod Kumar**, and **Prof. Sharath Sriram** for their valuable experimental support in the optical microscopy, and lithography. This thesis would not have been possible without your helpful support and guidance.

I would also like to express my gratitude to **Ganesh Prasad Singh** (Father), and **Manorama Devi** (mother), for their excellent guidance throughout my life. Thank you for encouraging me with your kind words and always believing in me.

I would like to express my whole-hearted thanks to **Dr. Gaurav Siddharth** (Brother) for her trustworthy help, company, discussions and debates, assistance during fabrication and characterization processes, and most importantly her presence during my challenging times. Thanks to **Dr. Ritesh Bhardwaj** for their help in understanding the basics of the photdetectors, its fabrication and characterization. My thanks also go to other lab members and

colleagues **Dr. Md Arif Khan, Dr. Mangal Das, Dr. Biswajit Mandal, and future doctors Pawan Kumar, Sanjay Kumar, Jyoti Tiwari, Mayank Dubey, Chandrabhan Patel, Sumit Chaudhary, Sourabh Yadav, Brahmadutta Mahapatra, and Vikash Verma,** and would also like to thank my post-graduation juniors **Mohit K. Gautam, Ranjan Kumar, Megha Nawaria, and Shruti Ghodke,** who in one way or the other provided me assistance and motivation whenever required. I would also like to express my gratitude to my friends and teachers from **graduation, post graduations** and **Ph.D.** for continually inspiring me at various times.

I am deeply grateful to my family members: **Aditya Pratap** (Husband), sisters **Rita, Pooja**, **Ratna and Laxmi**, mother in law **Sita Sukumari**, sister in law **Adhishwari and Siddheshwari**, and brother in law **Amritesh, Pravesh and Nikhil** for providing me unfailing support and continuous encouragement throughout my years of study and through the process of research and writing this thesis. I am also thankful to my nephew and niece, **Ritesh**, **Payal**, **Aadhya**, **Anandraj**, **Pratistha**, **and Tushita**. Finally, I specially want to thank **Aditya Pratap**, **Ganesh Prasad Singh**, **Dr. Gaurav Siddharth**, and **Pawan Kumar** for providing emotional support in this Ph.D. journey.

RUCHI SINGH

Dedicated

To my parents and spouse, Ganesh Prasad Singh, Manorama Devi and Aditya Pratap

LIST OF PUBLICATIONS

List of Publications

A: Publications from PhD thesis work

A1. Peer-reviewed Journals

1. **Ruchi Singh,** Chandrabhan Patel, Vikash Kumar Verma, Sharath Sriram, and Shaibal Mukherjee, "ZnO-based flexible UV photodetector for wearable electronic applications", **IEEE Sensor Journal,** early access, doi: 10.1109/JSEN.2023.3314528 **(IF: 4.325).**
2. **Ruchi Singh,** Chandrabhan Patel, Pawan Kumar, Mayank Dubey, Sharath Sriram, and Shaibal Mukherjee, "High Detectivity and fast MoS_2 monolayer MSM photodetector", **ACS Applied Electronic Materials**, 4, 12, 5739–5746, 2022. **(IF: 4.494)**
3. **Ruchi Singh,** Ritesh Bhardwaj, Gaurav Siddharth, Pawan Kumar, and Shaibal Mukherjee, "Analytical study of sputter-grown ZnO-based p-i-n homojunction UV photodetector", **IEEE Sensors Journal,** 21, 6, 7515-7521, 2021. **(IF: 4.325)**

A2. Proceedings of International Conferences

1. **Ruchi Singh,** Gaurav Siddharth, Ritesh Bharadwaj, and Shaibal Mukherjee, Structural and Optical Study of Sputtered Grown Sb Doped ZnO Thin Film, **IEEE 21st International Conference on Nanotechnology (IEEE NANO),** Montreal, Canada, July 28-30, 2021.
2. **Ruchi Singh,** Gaurav Siddharth, Ritesh Bhardwaj, and Shaibal Mukherjee, Structural Study of Sb doped ZnO Thin Film for Optical Applications, **5th International Conference on Emerging Electronics (ICEE),** IIT Delhi, Nov. 26-28, 2020.
3. **Ruchi Singh,** Ritesh Bhardwaj and Shaibal Mukherjee, Analytical Study of Thickness Variation on the Responsivity of Li-PZnO/ZnO/GaZnO Homojunction p-i-n UV Photodetector, **20th International Workshop on The Physics of Semiconductor Devices (IWPSD),** Kolkata, India, Dec. 17-20, 2019.

B: Other publications during PhD

B1. Peer-reviewed Journals

1. Pawan Kumar, Sumit Chaudhary, Md Arif Khan, **Ruchi Singh**, Myo Than Htay, Rahul Prajesh, Ajay Agarwal, and Shaibal Mukherjee, Impact of ZnO Cap Layer on the Performance of MgZnO/CdZnO Heterostructure With YO Spacer Layer, **IEEE Transactions on Electron Devices**, 69, 11, 5991-5995, 2022. **(IF: 3.221)**

2. Chandrabhan Patel, **Ruchi Singh,** Mayank Dubey, Sushil Pandey, Shrish Upadhyay, Vikash Kumar, Sharath Sriram, Myo Than Htay, Srimanta Pakhira, Victor Atuchin, and Shaibal Mukherjee, Large and Uniform Single Crystals of MoS_2 Monolayers for ppb-level NO_2 Sensing, **ACS Applied Nano Materials**, 5, 9415-9426, 2022. **(IF: 5.097)**

3. Mayank Dubey, Gaurav Siddharth, **Ruchi Singh**, Chandrabhan Patel, Sanjay Kumar, Myo Than Htay, Victor V. Atuchin, and Shaibal Mukherjee, Influence of Substrate Temperature and Sulfurization on Sputtered $Cu_2SnGe(S,Se)_3$ Thin Films for Solar Cell Application, **IEEE Transactions on Electron Devices**, 69, 5, 2488–2493, 2022. **(IF: 2.917)**

4. Gaurav Siddharth, **Ruchi Singh,** Vivek Garg, Brajendra S. Sengar, Mangal Das, Biswajit Mandal, Myo Than Htay, Mukul Gupta, and Shaibal Mukherjee, Investigation of DIBS-deposited CdZnO/ZnO-based multiple quantum well for large-area photovoltaic application, **IEEE Transactions on Electron Devices,** 67, 12, 5587-5592, 2020 **(IF: 2.917)**

5. Gaurav Siddharth, Brajendra S. Sengar, Vivek Garg, Md Arif Khan, **Ruchi Singh,** and Shaibal Mukherjee, Analytical performance analysis of CdZnO/ZnO-based multiple quantum well solar cell, **IEEE Transactions on Electron Devices,** 67, 3, 1047-1051, 2020. **(IF: 2.074)**

6. Ritesh Bhardwaj, **Ruchi Singh,** Md. Arif Khan, and Shaibal Mukherjee, Performance analysis of p-LPZO/n-GZO and p-SZO/n-GZO homojunction UV photodetectors, **Superlattices and Microstructures**, 140, 106451, 1-7, 2020. **(IF: 2.67)**

7. Pawan Kumar, Md Arif Khan, Gaurav Siddharth, Sanjay Kumar, **Ruchi Singh,** and Shaibal Mukherjee, Electron scattering analysis in 2DEG in sputtering-grown MgZnO/ZnO heterostructure, **Journal of Physics D: Applied Physics,** 53, 125108, 2019. **(IF: 3.169)**

B2. Proceedings of International Conferences

1. Gaurav Siddharth, **Ruchi Singh,** Mayank Dubey, Myo Than Htay and Shaibal Mukherjee, Optimization of dual ion beam sputtered MQWs for solar cell, **48th IEEE Photovoltaic Specialist Conference (IEEE PVSC)**, Virtual Meeting, June 20-25, 2021.
2. Gaurav Siddharth, **Ruchi Singh** and Shaibal Mukherjee, Modeling and Simulation of CdZnO/ZnO heterostructure based Multiple Quantum Wells for Photovoltaics, **37th European Photovoltaic Solar Energy Conference and Exhibition (EU PVSEC),** virtual meeting, September 7-11, 2020.
3. Gaurav Siddharth, **Ruchi Singh** and Shaibal Mukherjee, Modelling and Performance analysis of InGaN/GaN based Multiple Quantum Well solar cells, **47th IEEE Photovoltaic Specialist Conference (IEEE PVSC),** Virtual Meeting, June 15-August 21, 2020.
4. Gaurav Siddharth, **Ruchi Singh** and Shaibal Mukherjee, Analytical Study of InGaN/GaN-based Double Heterojunction p-i-n Solar Cell, **20th International Workshop on The Physics of Semiconductor Devices (IWPSD)**, Kolkata, December 17-20, 2019.
5. Ritesh Bhardwaj, **Ruchi Singh** and Shaibal Mukherjee, Effect of Mg concentration on MgZnO based UV Photodetectors, **6th Nano Today Conference,** Lisbon, Portugal, June 16-20, 2019.
6. Amitesh Kumar, Mangal Das, Sanjay Kumar, **Ruchi Singh**, Pawan Kumar, Abhinav Kranti and Shaibal Mukherjee, "Role of interface modulation during resistive switching for ZnO based RRAMs**", 1st Indian Materials Conclave and 30th Annual General Meeting of MRSI (MRSI-AGM),** IISc Bangalore, February 2019.
7. Ritesh Bhardwaj, **Ruchi Singh**, Biswajit Mandal, Gaurav Siddharth and Shaibal Mukherjee, "n-layer thickness optimization for ZnO based n-p homojunction UV photodetector", **International Conference on**

Computational Mathematics in Nanoelectronics and Astrophysics, IIT Indore, November 2018.

B3. Book Chapter

1. Ritesh Bhardwaj, **Ruchi Singh,** and Shaibal Mukherjee, Advances in ZnO-material based UV photodetectors, Invited by Saleem Hashmi (editor-in-chief), Reference Module in Materials Science and Materials Engineering, Oxford: Elsevier, September 2020.

TABLE OF CONTENTS

LIST OF FIGURES

LIST OF TABLES

ACRONYMS

PD	*Photodetector*
TMD	*Transition metal dichalcogenides*
ZnO	*Zinc Oxide*
MoS_2	*Molybednum Disulphide*
MSM	*Metal-Semiconductor-Metal*
QE	*QuantumEfficiency*
NEP	*Noise Equivalent Power*
D*	*Detectivity*
DIBS	*Dual Ion Beam Sputtering Deposition*
CVD	*Chemical Vapor Deposition*
IPCE	*Incident Photon Conversion Efficiency*
TCE	*Trichloroethylene*
DI	*Deionized*
HF	*Hydrogen Floride*
DPC	*Deposition Chamber*
LLC	*Load Lock Chamber*
KPRM	*Kilo Rotation Per Minute*
RF	*Radio Frequency*
PID	*Proportional–Integral–Derivative*
Al_2O_3	*Aluminium Oxide*
CPU	*Central Processing Unit*
MFC	*Mass Folw Controller*
DC	*Direct Current*
RT	*Room Temperature*
LED	*Light Emitting Diode*
PL	*Photoluminescence*
TERS	*Tip Enhanced Raman Spectroscopy*
UV	*Ultraviolet*
NIR	*Near Infrared*
ULF	*Ultra Low Frequency*

AFM	*Atomic Force Microscopy*
CCD	*Charge Coupled Device*
SC	*Solar Cell*
STC	*Standard Test Conditions*
PV	*Photovoltaics*
AM	*Air Mass index*
IQE	*Internal Quantum Efficiency*
TSP	*Test Script Processor*
GZO	*Ga-doped Zinc Oxide*
SZO	*Sb-doped Zinc Oxide*
BTB	*Band to Band*
IDE	*Interdigitated Electrode*
SBH	*Schottky Barrier Height*
NaCl	*Sodium Cloride*
NH_4OH	*Ammonia*
MoO_3	*Molybednum Oxide*
Si	*Silicon*
SiO_2	*Silicon Oxide*
DMM	*Digital Multimeter*
MSE	*Mean Square Error*
2D	*Two dimensional*
PET	*Polyethylene terephthalate*
PDMS	*Polydimethylsiloxane*
PI	*Polyimide*
PVC	*Polyvinyl chloride*

NOMENCLATURE

Å	*Angstrom*
μm	*Micrometer*
eV	*Electron Volts*
h	*Plank's Constant*
c	*Speed of light*
λ	*Wavelength*
I_D	*Dark Current*
I_{pc}	*photocurrent*
R	*Responsivity*
P_{in}	*Incident power*
η	*External Quantum Efficiency*
q	*Charge of Electron*
ν	*Frequency*
B	*Bandwidth*
D*	*Detectivity*
A	*Active area*
a, c	*Lattice Constants*
Ar	*Argon*
V	*Voltage*
I	*Current*
Hz	*Hertz*
mm	*Milimeter*
^oC	*Degree Celcius*
min	*Minute*
s	*Seconds*
sccm	*Standard Cubic Centimeters per Minute*
cc	*Cubic Centimeters*
cm	*Centimeter*
nm	*Nanometer*
V_{th}	*Thermal Voltage*

p-	*p-type*
i-	*Intrinsic-type*
n-	*n-type*
$(J_p)_i$ and $(J_i)_p$	*Diffusion current due to electrons and holes*
μ_n and μ_p	*Mobility of electrons and holes*
τ_n and τ_p	*Carrier Lifetime of electrons and holes*
N_i and N_A	*Carrier concentration of undoped and p-type ZnO*
t_p and d	*Thicknesses of SZO and ZnO layers*
γ_p and γ_n	*Surface to bulk recombination velocities*
x_p and x_i	*Widths of the depletion regions*
L_n and L_p	*Diffusion length of electrons and holes*
D_n and D_p	*Diffusion constants for electrons and holes*
S_n and S_p	*Surface recombination velocities*
m_p* and m_n*	*Effective mass of hole and electron*
J_{gr}	*Generation-recombination Current Density*
J_{tun}	*Tunneling Current Density*
A*	*Richardson Constant*
p_n and p_p	*Tunneling factors for electrons and holes*
V_d	*Build-in Voltage*
W	*Depletion region width*
E_g	*Energy bandgap*
α	*Absorption Coefficient*
T	*Temperature*
K	*Boltzman constant*
δ	*Energy Difference*
R_p, R_i and R_n	*Fresnal reflection coefficient*
n_2 and n_1	*Refractive Indices*
D	*Distance*
μL	*Microlitres*
ε	*Strain*
Ω	*ohm*
g	*gram*

ABSTRACT

Investigation of performance of oxide and TMD based photodetecting structures

by

Ruchi Singh

Hybrid Nanodevice Research Group

Department of Electrical Engineering

Indian Institute of Technology Indore

Supervisor: Prof. Shaibal Mukherjee and Dr. Pankaj Misra

With the innovation of photodetectors (PDs), new applications in flexible and wearable electronics, foldable displays, nano generators, and health patches are now being investigated. High bandgap and 2D transition metal dichalcogenides (TMDs) materials are now being investigated in various PD device structures. ZnO and its alloys have been extensively studied for their potential applications as a wide bandgap semiconducting material due to low lattice mismatch, resistance to radiation damage, availability of native substrates, wet chemical processing capability, and the ability to produce high-quality films. One of the most studied TMDs for electrical, optoelectronic, photovoltaic, and photocatalytic applications is S-Mo-S covalently bonded MoS_2 because of its two-dimensional structure, layer dependent conductivity, chemical composition, device miniaturization, and low power requirements. The goal of this entire project is to observe progress in the field of photodetector in terms of analytical modelling prior to actual fabrication of multilayer devices, newer materials for photodetecting applications, and flexible device electronics.

Prior to the actual experimental fabrication of the *p-i-n* homojunction PD, it is critical to conduct an analytical study of the PD's performance parameters under various conditions. In the analysed models, standard values of the constant parameters such as surface recombination velocity,

diffusion constant and diffusion length, minority carrier lifetime are used for ZnO material system along with some mathematically derived parameters like surface to bulk recomibination velocity, built-in potential, etc. The model consider the individual components of current density: diffusion, generation-recombination, tunneling to produce total dark current density as a summation of individual components. Similarly, the total quantum efficiency is calculated as the summation of quantum efficiency of *p*-, *i*- and *n*-regions, respectively. The spectral response and peak responsivity with reverse bias voltage of the PD with varying thickness of individual regions is analysed in the model. The parameters of the DIBS deposited Sb doped ZnO as *p*-type (SZO), intrinsic ZnO as *i*-type (ZnO), and Ga doped ZnO as n-type (GZO), resepectively, is utilized.

The developed model of homojunction *p*-*i*-*n* PD is even further evaluated for validation by comparing with the published experimental results gathered by other reasearchers on the same material system. On the based of this developed model, the dark current and spectral response of the sputtered grown Doped ZnO homojunction *p*-*i*-*n* PD is estimated. The PD shows a wavelength seelctivity in the UV region near the absorbtion edge endorsing the analytical study of UV PD as expected due to wide bandgap value of ZnO. The optimized thicknesses of 50 nm and 80 nm of top *p*-type SZO region and sandwiched *i*-type ZnO region, respectively are obtained in this study. The outcomes show that the responsivity grows by 98.56% while intrinsic *i*-type film thickness rises from 20 to 80 nm and it decreases by 42.13% as topmost acceptor doped *p*-type film thickness increases from 50 to 200 nm.

In order to explore the different regime of 2d TMD in light detection application, MoS_2 monolayer has been deposited utilizing CVD system over SiO_2/Si substrate. Intially a seed layer of MoO_3 is deposited over the substrate via spin coating, this seed layer is then interect with sulfur fumes in the CVD furnace to produce MoS_2 monolayer, confirmed by optical microscopy, Raman spectroscopy and sectroscopic ellipsometry analysis. Surface assisted wet transfer process is exploited for transferring of CVD deposited MoS_2 monolayer over interdigitated Pt electrode over glass

substrate. A solution of polystrene and toluene as used for peeling off MoS_2 monolayer from SiO_2/Si substrate and its placing over the electrode.

A number of device performance metrics, including dark and light current-voltage (I-V), spectral responsivity, external quantum efficiency, detectivity, noise equivalent power, and photo switching characteristics, are procured on the MoS_2 monolayer MSM PD. The photodetector performance is analyzed, at 5 V, wherein the dark current of the device increases to 1.61×10^{-7} A from 5.37×10^{-8} A as operating temperature increases from 25 ^{o}C to75 ^{o}C, while photocurrent increases from 3.02×10^{-6} A to 8.43×10^{-6} A with decrease in 28.17 %, respectively. The peak detectivity and NEP are 1.11×10^{11} cm.$Hz^{0.5}W^{-1}$ and 1.24×10^{-11} W, respectively. The rise and fall time are 0.06 ms and 0.14 ms, respectively, and the photocurrent on/off ratio is 256.

The wearable and flexible electronic applications of sputtered grown ZnO MSM PD over polyimide flexible substrate is investigated. Examination of the complete device is performed at normal (flat) and different bending conditions, respectively. I-V analysis in both dark and incident light wavelength along with different bending conditions is performed for varifying wavelength selectivity and impact of bending (strain) on the device. Classic thermionic field emission transport theory and piezo-phototronic effect is used for analytical scrutinization of the performace of the PD. The device is also explored for spectral response with different biased and bending condition in addition to measurement of the quantum efficiency of the MSM PD.

The piezo-phototronic effect describe the impact of strain and the biased voltage on the change in SBH and charge carrier accumulation at the metal-semiconductor Schottky junction. The higher value in the relative change of SBH under bending results in reduction of photocurrent initially, which is compensated by increased electric field at higher biased voltage in the UV PD. The ZnO based flexible UV PD provides the maximum photocurrent for 325 nm wavelength, with an I_{on}/I_{off} ratio of 215 at 6 V in normal condition. The spectral response of the device suggests that it is suitability for UV PD with a peak responsivity of 0.5 A/W.

Chapter 1

Introduction and Fundamental Concepts

1.1. Introduction of Photodetectors

The range of electromagnetic spectrum varies from very short wavelength of 0.1 Å to thousands of kilometres corresponding to X-ray and radio waves, respectively. A subset of these wavelength ranging from 10 nm to 50 μm constitutes optical region of spectrum combining ultraviolet, visible and infrared. Radiation detectors capable to operate in the mentioned region of spectrum are called photodetectors. In other words, photodetectors are the electronic device capable of sensing of optical region (light) of electromagnetic spectrum [1]. These devices are mainly classified into two sub categories of thermal and photon detectors. A material with a strongly temperature-dependent property is used to make a thermal detector. The material will change as the incident radiation is absorbed, and by measuring the change, the amount of energy absorbed can be determined, such as when an electrical conductivity or gas expansion occurs. A black surface coating typically absorbs the radiation, resulting in a broad and uniform spectral response. However, the sensitivity is typically lower than that of a photon detector, where the material's electrons are excited by the incident radiation and an electrical output signal is observed. The photoemissive device and the solid state sensor are the two distinct categories of photon detectors that can be distinguished by observing this output signal. In the first case, the photosensitive electrode releases excited electrons into the surrounding medium, which can be a vacuum or a gas [1-2]. In contrast, in a solid-state detector, the photons alter the material's electronic energy distribution. An output signal is produced by this change in energy. The conductivity change that results from changing the number of free electrons or holes, for instance, is measured in a photoconductor. These photoconductors are the most common type of photodetectors discussed and explored in solid state electronics i.e. optoelectronics [2-3].

1.2. Motivation

An optoelectronic device known as a photodetector uses a variety of photo-related phenomena to transform a light signal into an electrical signal. With the progression of photodetectors (PDs), arising applications in the field of adaptable and wearable gadgets, foldable showcases, nano generators, wellbeing patches, are currently being investigated. Communication, radiation detection (smoke, flame, and missile plume), water sterilization, atomic force microscopy, laser-based devices, inter-satellite communication, ozone layer monitoring, and automotive anti-collision optical radar are some other common applications for PDs [4]. Systems interfacing photodetector with read-out circuits are now been implemented for exploring photodetector based internet of things (IoT) applications [5-6].

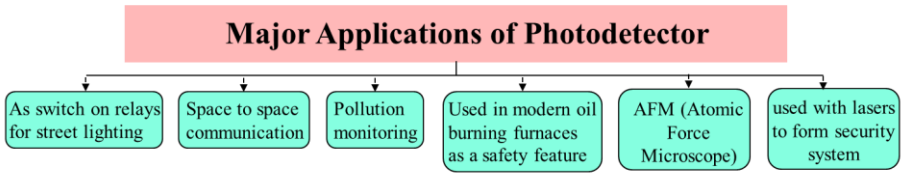

Figure 1.1 *Common applications of photodetectors.*

The primary concerns for these applications are a high signal-to-noise ratio, high precision, self-powered, sensitive, and fast response, as well as a low power consumption and greater miniaturization. In various device structures of PDs, high bandgap and 2D transition metal dichalcogenides (TMDs) materials have recently been investigated [7]. The PD's low sensitivity and efficiency, high order filters, high voltage supply requirement, device degradation, and ultra-high vacuum requirement, however, limit its widespread application [8]. The wavelength spectrum that needs to be detected is the determining factor in selecting the detecting material for PD fabrication. Many researchers have looked into wide bandgap semiconductor materials like SiC, AlGaN/GaN, and ZnSe for UV and deep UV wavelength detection. Zinc Oxide (ZnO) and its alloys have been the subject of extensive research over the past ten years for potential uses as a wide bandgap

semiconducting material. This is for the most part inferable from elements, for example, negligible cross section crisscross, protection from radiation harm, the accessibility of local substrates, amiability to wet synthetic handling, and the chance of creating great movies. [7-8]. The determination of a proper material with explicit highlights is of essential significance for the development of PDs that navigate an assortment of electromagnetic range ranges. Numerous ground-breaking research was carried out, including band engineering with heterostructure. Due to its remarkable two-dimensional structure, layer-dependent conductivity, chemical composition, device miniaturization, and low power requirements, TMDs are one of the upcoming electronic and optoelectronic materials. One of the most extensively studied multilayer TMDs for electrical, optoelectronic, photovoltaic, and photocatalytic applications is S-Mo-S covalently bonded Molybdenum disulphide (MoS_2) [9]. MoS_2 monolayer's outstanding properties include a direct energy bandgap of 1.8 eV at room temperature, high mobility (700 cm^2/V.s), significant optical absorption for the visible spectrum, a high current on/off ratio, and a prominent photoluminescence peak, making it an ideal candidate for PDs devices. MoS_2 monolayer has opened the door to a variety of research platforms, including photodetection properties in the visible region [9]. The wavelength detection range varies depending on doping and the number of MoS_2 layers in the device structure.

1.3. Working Principle

The bundles of energetic particles are called photon, and these particles composes optical spectrum. The Planck-Einstein relation describes each photon's energy, which is proportional to its wavelength in the electromagnetic spectrum (light) [10]. The relation is given by:

$$E = \frac{hc}{\lambda} \tag{1.1}$$

where h - Planck constant, c - speed of light, and λ - light wavelength.

The photoelectric effect, or the direct conversion of optical photon energy into electricity, is the foundation upon which photodetectors operate. There are basically three processes in the photon energy conversion flow [11] as depicted in Figure 1.2:

Figure 1.2 *Process flow of photon energy conversion.*

1.3.1 Generation of Charge Carrier:

The absorption of photons by the materials that make up the *p-n* junction is the first step in the process of creating charge carriers. Photons with an energy that is greater than or equal to the material's energy bandgap generate charge carriers; on the other hand, photons with a lower energy pass through the material without being absorbed and will not contribute to the generation of charge carriers.

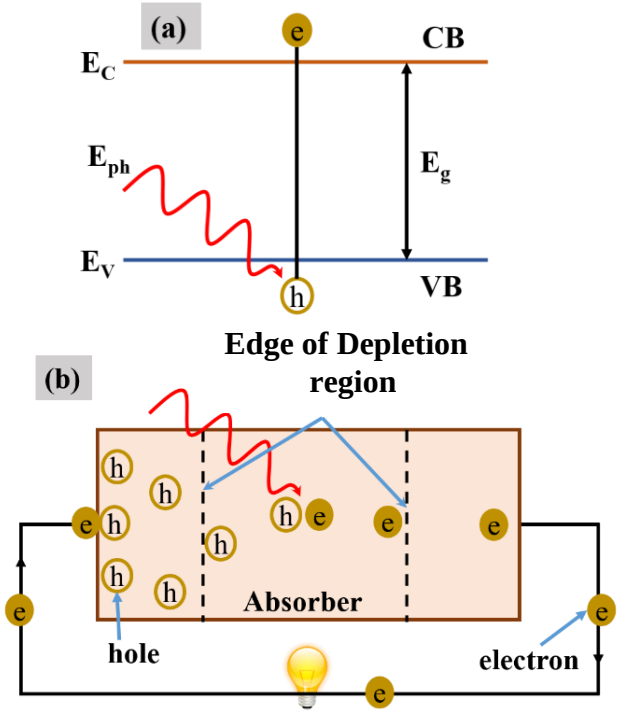

Figure 1.3 *(a) Energy band diagram showing generation of charge carrier by the absorption of photons (b) Simple p-n junction model of photodetector showing separation and collection of charge carrier and then flow of electron through external circuit.*

This process of creating carriers results in the formation of electron hole pairs. The electron leaves the hole in the lower energy state (valence band) in this generated pair and moves to the higher energy state (conduction band) as shown in Figure 1.3 (a).

1.3.2 Separation of Charge Carrier:

Recombination of the charge carrier may occur after its lifetime; consequently, the generated charge carrier must be separated prior to recombination in order to generate electricity. As can be seen in Figure 1.3 (b), the edge of the depletion width present on both sides of the absorber layer (depletion region) allow electrons to pass through one and holes to pass through the other. This depletion regions are essentially framed by the *p*-and *n*-type materials.

1.3.3 Collection of Charge Carrier:

In the final step, the separated charge carriers are collected at the contacts so that electrons can flow through the external circuit to generate electricity and recombine with the holes at the other contact, as shown in Figure 1.3 (b).

1.4. Structures of PD and Figure of Merits

The structures of PD are broadly classified in three configurations as metal-semiconductor-metal (MSM), *p*-*n* and *p*-*i*-*n* PDs [11-12]. MSM PDs have the advantages of planer structure hence easy to fabricate and suitable for integrated circuit technology, low strain capacitance, wide bandwidth, and fast response due close placing of metal contacts [13]. The primary purpose of the *p*-*n* junction PD is to permit light to pass through the metallurgical junction's peripheral region. Due to limited carrier diffusion, the *p*-*n* homojunction and heterojunction are slower but more sensitive to incident light [14]. However, because they operate quickly, have a high value of sensitivity, and exhibit photo-generated gain, *p*-*n* Avalanche PD can enhance their response [15]. These are typically used in a configuration with reverse bias, with the applied bias

close to the breakdown bias voltage. Photo-generated carriers are able to produce an impact ionization process because of the intensely high applied electric field. They travel across the junction at saturation velocity. More carriers can be produced by these drifted electrons and holes [12,16]. The impact ionization process, is the phenomenon which results in carrier multiplication and thus, provide gain in the device. The *p-i-n* homojunction structure is the preferred option out of all of them because of its superior interface quality throughout, making the junction electrically and metallurgically superior. In comparison to conventional *p-n* architecture, the *i*-layer in *p-i-n* architecture makes it possible to absorb incident photons more effectively [17-18]. Additionally, the *p-i-n* PD's response speed can be improved due to the addition of a high-field intrinsic layer between the p and n regions.

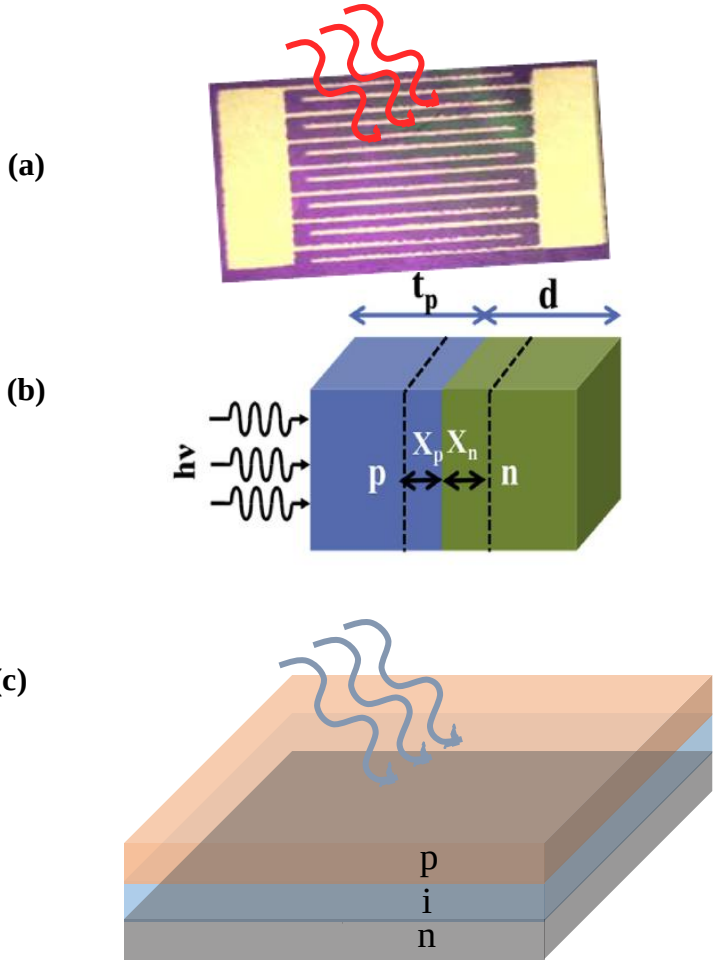

Figure 1.4 *Different structures of PD (a) MSM, (b) p-n junction, and (c) p-i-n junction.*

The vital performance figure of merits of PDs are [19-21]:

1.4.1 Dark Current (I_D) and Photocurrent (I_{pc}):

When no photons (no radiation from the outside enters the detector) enter a photosensitive device, a small electric current known as dark current flows through it. In non-optical devices, it is known as reverse bias leakage current and is present in all diodes. Physically, dark current is caused in the device's depletion region by random generation of electrons and holes [22-23].

The electric current that flows through a photosensitive device, like a photodiode, when it is exposed to incident optical power (P_{in}) is known as photocurrent. The photoelectric, photoemissive, or photovoltaic effects may cause the generation of photocurrent [24].

1.4.2 Responsivity (R):

The ratio of the photocurrent output (in amperes) to the incident optical power (in watts) is known as responsivity. The quantity is expressed in amps per watt (A/W). Thusly, responsivity is the measure of the semiconductor device effectiveness for converting the electromagnetic radiation to the electrical current [25]. Temperature, bias voltage, and wavelength all have an impact on responsivity. Reflection and absorption qualities of the detector material is wavelength depend quantities and consequently responsivity likewise changes with wavelength.

$$R = \frac{I_{pc}}{P_{in}} = \frac{\eta q}{h\nu} \tag{1.2}$$

Where η is external quantum efficiency, q is charge of electron and ν is frequency of incident light.

1.4.3 Quantum Efficiency (η):

The ratio of an electron generation rate to a number of incident photons is known as the quantum efficiency (QE) of a photodetector and it is often measured in % [26].

$$R = \frac{I_{pc}/q}{P_{in}/h\nu} = \frac{I_{pc}}{q}.\frac{h\nu}{P_{in}} \quad (1.3)$$

1.4.4 Noise Equivalent Power (NEP):

NEP is the smallest trespassing optical power that a detector can distinguish from the noise [27] and is given as in equation 1.4:

$$NEP = \frac{(2qBI_D)^{\frac{1}{2}}}{R} \quad (1.4)$$

Where B is bandwidth.

1.4.5 Specific Detectivity (D*):

Specific detectivity is equal to the reciprocal of NEP multiplied with square root of area [28], which can be expressed as in equation (1.5):

$$D^* = \frac{RA^{\frac{1}{2}}}{(2qBI_D)^{\frac{1}{2}}} \quad (1.5)$$

Where A is the active area of the device.

1.4.6 Rise and Fall time:

When the detector is being irradiated with pulsed radiation, in which the rise and fall times are so brief that it appears as a square wave, then the response time is defined as the time taken for the photocurrent to rise from the 10% of the base value to 90% of the peak value is called rise time. Similarly, the time taken to decay from 90% of the peak value to 10% of the base value is termed as fall time [29-30].

1.5. ZnO and MoS_2 Semiconductor Materials

Zinc oxide (ZnO) is a direct wide bandgap (3.37 eV at room temperature) semiconductor which solidifies in two principal structures, hexagonal wurtzite [31] and cubic zinc blende [32]. Figure provides a schematic representation of the arrangement of these structural phases for easier comprehension. 1.5. The Zn atom and the O atom are both denoted by yellow circles in the schematic. The wurtzite structure is more prevalent among these two structures and is thermodynamically

stable at ambient temperatures. At room temperature, the lattice parameters of hexagonal wurtzite ZnO are a = 3.25 and c = 5.20 [33]. Like other II-VI semiconductors, wurtzite ZnO can be transformed into rocksalt (NaCl) at external moderate hydrostatic pressures.

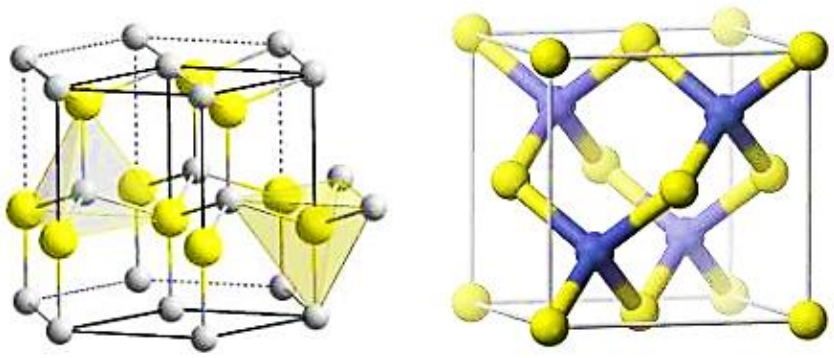

(a) **(b)**

Figure 1.5 *The representation of crystal structures of ZnO: (a) Wurtzite (b) Zinc blende.*

ZnO's large refractive indices from ultraviolet to visible, high breakdown strength, high saturation velocity for electronic device applications, and existence of well-established thin film growth processes are additional unique features. Alloying with other oxide is often implemented to tune the ZnO bandgap [34-35].

MoS_2 is one of the layered TMDs that has received the most research because of its widespread nature as molybdenite. Due to its mechanical flexibility, MoS_2 with an odd number of layers could produce oscillating piezoelectric voltage and current outputs [36]. This suggests that MoS_2 could be used to power nanodevices and stretchable electronics. The thickness of each MoS_2 layer is ~0.65 nm.

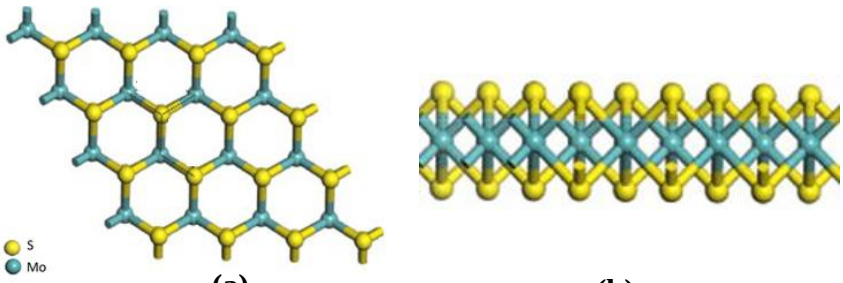

(a) **(b)**

Figure 1.6 *Crystallographic representation of monolayer MoS_2: (a) top view and (b) front view.*

Semiconducting monolayer MoS_2 with a trigonal prismatic polytype is referred to as 2H, while metallic monolayer MoS_2 with an octahedral crystal symmetry configuration is referred to as 1T [37-38]. Due to the planar exciton confinement effect, MoS_2 has strong light-matter interactions and tunable band gaps in the visible and near-infrared wavebands. Monolayer MoS_2 exhibits direct band-gaps and bound excitons in the single-layer limit, which are fundamentally intriguing for achieving applications in nanophotonics and optoelectronics [39].

1.6. Problem Formulation and Execution Plan

The purpose of this entire work is to examine the development of analytical modeling in the photodetector field, before actually fabricating multilayer devices, newer materials for photodetecting applications, and flexible device electronics. It is essential to have a solid understanding of a number of variables, including electrical, optical, and structural aspects, in order to construct high-performance optoelectronic devices. Also that examination of various part of photodetecting gadget requires different testimony strategy for the statement of the semiconducting materials.

Sputtering is replacing traditional plasma-based deposition methods for large-scale fabrication because it allows for independent control of beam energy, direction, and current density. The faltering based strategies are practical and appropriate for huge region testimony. High-quality thin films with greater compositional stoichiometry, homogeneity, and film adhesion on larger substrate surface areas are characteristic of the dual ion beam sputtering (DIBS) method [40]. However, non-conductive dielectric target materials can be deposited using the reactive magnetron sputtering technique at a significantly lower pressure, with a high sputtering yield, and uniform layer deposition.

Many MoS_2 monolayer deposition methods are currently being studied and regulated, but they do not allow for homogeneous film growth. Chemical vapor deposition (CVD) is one of the most straightforward

and efficient methods for fabricating MoS_2 monolayers [41-42]. This is due to the fact that it has a high degree of adaptability in terms of substrates and growth conditions. As a result, the CVD system is used to grow the MoS_2 monolayer for MSM PD fabrication.

The following are the necessary steps to accomplish the above goal:

• The formulation of an analytical model for the photoresponsivity and dark current analyses of a UV photodetector (PD) based on a DIBS-grown ZnO thin film

• CVD deposition of a MoS_2 monolayer and evaluation of a MoS_2 monolayer MSM device for various photodetecting application performance parameters

• An examination of the performance of sputtered ZnO-based MSM UV flexible PD under both standard and irregular device bending conditions.

1.7. Thesis Organization

The research in this thesis describe the analytical modelling, fabrication and measurement of performance of wide bandgap and 2d MoS_2 based photodetector for various electronics application including foldable electronics. Based on this, the thesis is organised as follows:

Chapter 1 presents the motivation and introduction for the research work presented in behind doing this thesis. The chapter summarize the basic properties of the ZnO and MoS_2 materials and their advantages for the realization of PDs application, along with discussion of the prior state-of-art research work in this field.

Chapter 2 covers the deposition and characterization technologies used in the fabrication and testing of ZnO and MoS_2 PDs. DIBS, CVD, and reactive magnetron sputtering are utilized to deposit the materials. Variable-angle-variable-wavelength Spectroscopic Ellipsometry (SE), Source meter, Solar Simulator (Photo Emission Tech Inc.), Current-Voltage (I-V), and Bentham PVE300 incident photon conversion efficiency (IPCE) measurement system, Keithley

DMM6500, Horiba LabRam Raman spectroscopy, and Carl Zeiss Axio Vert.A1 inverted microscope are used to perform the various device characteristics.

Chapter 3 labels the developed analytical model for ZnO-based *p*-i-n homojunction UV PD and analyzing the performance, in terms of dark current and responsivity, of homojunction *p-i-n* UV PDs by proper optimization of the thickness of different layers.

Chapter 4 describes the chemical vapor deposition (CVD)-deposited MoS_2 monolayer, its verification followed by surface energy assisted wet transfer. Performance analysis of MoS_2 monolayer MSM PD for dark and light current, responsivity, quantum efficiency and switching response.

Chapter 5 consists a discussion of ZnO based MSM PD structure over flexible polyimide substrate. The PD is then evaluated for relevant performance parameters, both in normal and different bending conditions. The classic thermionic emission model under bending condition is also conversed.

Chapter 6 illustrates the summary of the research work from the thesis and proposes the scope for future works for the continuation of the research on this topic.

1.8. References

[1] P. N. J. Dennis, "Photodetectors an Introduction to Current Technology," Plenum, New York 1986.

[2] L. R. Canfield, "6. Photodiode Detectors," In Experimental Methods in the Physical Sciences, 32, 117-138. Academic Press, 1998.

[3] W. Yang, J. Chen, Y. Zhang, Y. Zhang, J. H. He, and X. Fang, "Silicon-compatible photodetectors: trends to monolithically integrate photosensors with chip technology," Advanced Functional Materials 29, 18, 1808182, 2019.

[4] Y. A. Goldberg, "Semiconductor near-ultraviolet photoelectronics," Semiconductor science and technology, 14, 7, R41, 1999.

[5] X. Liang, X. Wan, X. Lu, and Y. Zhang, “IoT Security Techniques Based on Machine Learning,” Signal Processing and Internet of Things. IEEE Signal Processing Magazine, 35, 2018.

[6] B. Sarwar, I. S. Bajwa, N. Jamil, S. Ramzan, and N.Sarwar, “An intelligent fire warning application using IoT and an adaptive neuro-fuzzy inference system,” Sensors, 19, 14, 3150, 2019.

[7] K. Liu, M. Sakurai, and M. Aono, “ZnO-based ultraviolet photodetectors,” Sensors, 10, 9, 8604-8634, 2010.

[8] D. Som, S. Trivedi, A. Chatterjee, and S. Kanungo, “Van der Waals (vdW) Heterostructures Based on Transition Metal Dichalcogenides (TMD): Current Status and Prospects in Broadband Photodetector Applications,” Microelectronics and Signal Processing, 1-16, 2021.

[9] A. Taffelli, S. Dirè, A. Quaranta, and L. Pancheri, “MoS_2 based photodetectors: a review,” Sensors, 21, 8, 2758, 2021.

[10] A. H. Smets, K. Jager, O. Isabella, R. A. Swaaij, and M. Zeman, “Solar energy: The physics and engineering of photovoltaic conversion, technologies and systems,” Cambridge: Cambridge University Press, 2015.

[11] M. A. Green, and S. P. Bremner, “Energy conversion approaches and materials for high-efficiency photovoltaics,” Nature materials 16, 1, 23-34, 2017.

[12] Y. Zou, Y. Zhang, Y. Hu, and H. Gu, “Ultraviolet detectors based on wide bandgap semiconductor nanowire: A review,” Sensors, 18, 7, 2072, 2018.

[13] L. Jia, W. Zheng, and F. Huang, “Vacuum-ultraviolet photodetectors,” PhotoniX, 1, 1, 1-25, 2020.

[14] W. Tian, Y. Wang, L. Chen, and L. Li, “Self-powered nanoscale photodetectors,” Small, 13, 45, 1701848, 2017.

[15] J. Michel, J. Liu, and L. C. Kimerling, “High-performance Ge-on-Si photodetectors,” Nature photonics, 4, 8, 527-534, 2010.

[16] R. A. Yotter, and D. M. Wilson, “A review of photodetectors for

sensing light-emitting reporters in biological systems," IEEE Sensors Journal, 3, 3, 288-303, 2003.

[17] J. Wang, and Sungjoo Lee, "Ge-photodetectors for Si-based optoelectronic integration," Sensors, 11, 1, 696-718, 2011.

[18] J. E. Bowers, A. Ramaswamy, D. Dai, W. S. Zaoui, Y. Kang, T. Yin, and M. Morse, "Recent advances in Ge/Si PIN and APD photodetectors," Physica Status Solidi c, 7, 10, 2526-2531, 2010.

[19] M. Long, P. Wang, H. Fang, and W. Hu, "Progress, challenges, and opportunities for 2D material based photodetectors," Advanced Functional Materials 29, no. 19 (2019): 1803807.

[20] D. Yang, and D. Ma, "Development of organic semiconductor photodetectors: from mechanism to applications," Advanced Optical Materials, 7, 1, 1800522, 2019.

[21] R. Saran, and R. J. Curry, "Lead sulphide nanocrystal photodetector technologies," Nature Photonics, 10, 2, 81-92, 2016.

[22] G. Simone, M. J. Dyson, S.CJ Meskers, R. AJ Janssen, and G. H. Gelinck, "Organic photodetectors and their application in large area and flexible image sensors: the role of dark current," Advanced Functional Materials, 30, 20, 1904205, 2020.

[23] A. D. Stiff-Roberts, "Quantum-dot infrared photodetectors: a review," Journal of Nanophotonics, 3, 1, 031607, 2009.

[24] C. Main, S. Reynolds, and R. Brüggemann, "Decay from steady-state photocurrent in amorphous semiconductors," Physica Status Solidi c, 1, 5, 1194-1207, 2004.

[25] X. Wang, and X. Gan, "Graphene integrated photodetectors and opto-electronic devices—a review," Chinese Physics B 26, 3, 034203, 2017.

[26] R. C. Jone, "Quantum efficiency of detectors for visible and infrared radiation," Advances in electronics and electron physics, 11 87-183, 1959.

[27] B. S. Karasik, A. V. Sergeev, and D. E. Prober,

"Nanobolometers for THz photon detection," IEEE Transactions on Terahertz Science and Technology, 1, 1 97-111, 2011.

[28] J. Xu, W. Zheng, and F. Huang, "Gallium oxide solar-blind ultraviolet photodetectors: a review," Journal of Materials Chemistry C, 7, 29, 8753-8770, 2019.

[29] L. Peng, L. Hu, and X. Fang, "Low-dimensional nanostructure ultraviolet photodetectors," Advanced Materials, 25, 37, 5321-5328, 2013.

[30] R. Tang, S. Han, F. Teng, K. Hu, Z. Zhang, M. Hu, and X. Fang. "Size-controlled graphene nanodot arrays/ZnO hybrids for high-performance UV photodetectors," Advanced Science, 5, 1, 1700334, 2018.

[31] R. Bhardwaj and S. Mukherjee, "Nanoscale UV photodetectors based on ZnO and alloyed ZnO," Elsevier: Reference Module in Materials Science and Materials Engineering, 2018.

[32] Y. Hou, Z. Mei, and X. Du, "Semiconductor ultraviolet photodetectors based on ZnO and $Mg_xZn_{1-x}O$," Journal of Physics D: Applied Physics, 47, 28, 283001, 2014.

[33] J. L. Yang, K. W. Liu, and D. Z. Shen, "Recent progress of ZnMgO ultraviolet photodetector," Chinese Physics B, 26, 4, 047308, 2017.

[34] S. K. Pandey, S. Kumar Pandey, V. Awasthi, M. Gupta, U. P. Deshpande, and S. Mukherjee, "Influence of in-situ annealing ambient on *p*-type conduction in dual ion beam sputtered Sb-doped ZnO thin films," Applied Physics Letters, 103, 7, 072109, 2013.

[35] G. H. Lee, T. Kawazoe, and M. Ohtsu, "Room temperature nearfield photoluminescence of zinc-blend and wurtzite ZnO structures," Applied Surface Science, 239, 3-4, 394, 2005.

[36] H. S. Nalwa, "A review of molybdenum disulfide (MoS2) based photodetectors: from ultra-broadband, self-powered to flexible devices," RSC advances, 10, 51, 30529-30602, 2020.

[37] Y. Wakayama, and R. Hayakawa, "Antiambipolar transistor: A

newcomer for future flexible electronics," Advanced Functional Materials 30, 20, 1903724, 2020.

[38] L. R. Zou, D. D. Sang, Y. Yao, X. T. Wang, Y. Y. Zheng, N. Z. Wang, C. Wang, and Q. L. Wang. "Research progress of optoelectronic devices based on two-dimensional MoS_2 materials," Rare Metals, 1-22, 2022.

[39] A. Rai, H. CP Movva, A. Roy, D. Taneja, S. Chowdhury, and S. K. Banerjee, "Progress in contact, doping and mobility engineering of MoS_2: an atomically thin 2D semiconductor," Crystals, 8, 8 316, 2018.

[40] R. Bhardwaj, P. Sharma, R. Singh, M. Gupta, and S. Mukherjee, "High Responsivity $Mg_xZn_{1-x}O$ Based Ultraviolet Photodetector Fabricated by Dual Ion Beam Sputtering," IEEE Sensors Journal, 18,7, 2744-2750, 2018.

[41] Y. Zhang, Y. Yao, M. G. Sendeku, L. Yin, X. Zhan, F. Wang, Z. Wang, and J. He, "Recent progress in CVD growth of 2D transition metal dichalcogenides and related heterostructures," Advanced materials, 31, 41, 1901694, 2019.

[42] F. Yan, Z. Wei, X. Wei, Q. Lv, W. Zhu, and K. Wang, "Toward High-Performance Photodetectors Based on 2D Materials: Strategy on Methods." Small Methods, 2, 5, 1700349, 2018.

Chapter 2

Fabrication and characterization techniques for PDs

2.1. Introduction

The exploration of novel materials with diverse characteristics and applications has made a decisive role in the advancing science and technology. This chapter briefly describes all the equipment used in the deposition of ZnO thin film and MoS_2 monolayer along with different characterization tools for the analysis of the deposited thin film and fabricated PDs. Dual ion beam sputtering (DIBS) and reactive magnetron sputtering system has been deployed for the deposition of ZnO thin films. Furthermore, chemical vapor deposition (CVD) system is deployed for growth of MoS_2 monolayer. MATLAB R15a tool is exploited for the analytical modelling of the *p-i-n* PD. Distinct characterization techniques are utilized to study the structural, electrical, and optical properties of the thin films. The Spectroscopic ellipsometry measurement system and optical microscopy system are used to measure the optical properties of the thin film. The spectral photoresponse of fabricated PDs is measured using incident photon conversion efficiency (IPCE) measurement system. Raman spectroscopy, solar simulator and various instruments of Keithley is used for different performance analysis of the photodetector under observation.

2.2. Substrate Selection and Cleaning Process

The type and state of the substrate's surface play a crucial role in high-quality thin film growth, despite the fact that the quality of the deposited thin film depends on the deposition technique. Low chemical reactivity, low surface roughness, and high mechanical strength are all desirable characteristics of the substrate. The device's application type, cost,

manufacturing process, and packaging all play a role in determining the substrate of choice. The substrates for the deposition of thin films in this thesis are silicon and corning glass. The purity of the films and their ability to adhere to the substrates are affected by contamination at the surface of the substrate; consequently, the substrate must be properly cleaned prior to the deposition of the sensing film [1]. A suitable cleaning method was used to clean the substrates based on the kind of substrate and any potential contaminants that might be on it.

2.2.1 Procedure for Cleaning Silicon Substrates

In this thesis, the Si substrates were cleaned using the following steps:

- Before cleaning the substrates, use a pipette-like blower to get rid of the dust.
- Ultrasonic cleaning with a diluted TCE solution to get rid of any heavy residue or fingerprints on the wafer.
- Use DI water to rinse off any remaining TCE.
- Wafers are cleaned using ultrasonics in acetone to get rid of any organic debris or contaminants.
- To get rid of any remaining acetone, rinse with DI water.
- Ultrasonic cleaning with diluted isopropanol to dissolve non-polar contaminants remaining on the wafers.
- To get rid of any remaining isopropanol, rinse with DI water.
- To remove native silicon dioxide from wafers, dip in HF solution.
- Wash with DI water.
- Use high-purity nitrogen gas to purge the substrate of any remaining water.

2.1.2 Procedure for Cleaning the Glass Substrates

In this thesis, the following steps were used to clean the glass substrates:

- Methanol-based ultrasonic cleaning to get rid of any oil or fingerprints.

- Use DI water to rinse off any remaining soap.
- Using acetone and ultrasonic cleaning to agitate the surface to get rid of small dust particles.
- To get rid of any remaining acetone, rinse with DI water.
- Ultrasonic cleaning with diluted isopropanol to dissolve non-polar contaminants remaining on the wafers.
- Use DI water to rinse and blow out the water droplets.
- Use high-purity nitrogen gas to purge the substrate of any remaining water.

2.3. Thin Film Deposition tools

In this research work, the growth of the polycrystalline ZnO to fabricate PD on different substrate, Elettrorava-DIBS and PVD75 pro reactive magnetron sputtering system is used. Quazar tech CVD system is used for MoS_2 deposition. The following sub-sections are described these system in detailed manner.

2.3.1 DIBS System

Multiple thin films are deposited using the DIBS system to create the thin film PD structure. The DIBS System is based on the physical vapour deposition method, which is used to deposit thin films in ultrahigh vacuum conditions for various electronics and optoelectronic devices like photodetector, photovoltaic, and light-emitting diode devices [2-4]. When it comes to producing high-quality thin films with precise element composition, superior film adhesion to the substrate, reduced surface roughness, and the ability to pre-clean substrates in situ prior to film deposition, the DIBS system excels [5]. The DIBS system also has the advantage of uniform deposition over a large area, making it useful for making a photovoltaic cell with a large area.

The benefits of the DIBS framework comes from the two particle sources: (1) depositing source, also known as a primary ion source, and (2) supporting source, also known as a secondary ion source [4]. The

schematic of the deposition chamber (DPC) and visual picture of DIBS framework are displayed in Figure 2.1 and 2.2, individually.

Sputtering materials from a target onto the substrate with the primary ion source is the method of choice. The DIBS system allows for the selection of an appropriate target for the deposition of thin film by mounting four distinct targets simultaneously on a rotating and water-cooled target assembly.

Both the pre-cleaning (etching) of the substrate surface prior to the start of the thin film deposition process and the removal of any island formation during the deposition process are carried out using the secondary ion source that is aimed at the substrate holder assembly. Between the target assembly and the primary ion source, a 45-degree angle is maintained, and between the substrate holder assembly and the assist ion source, a 60-degree angle is maintained. The inside view of DPC is shown below:

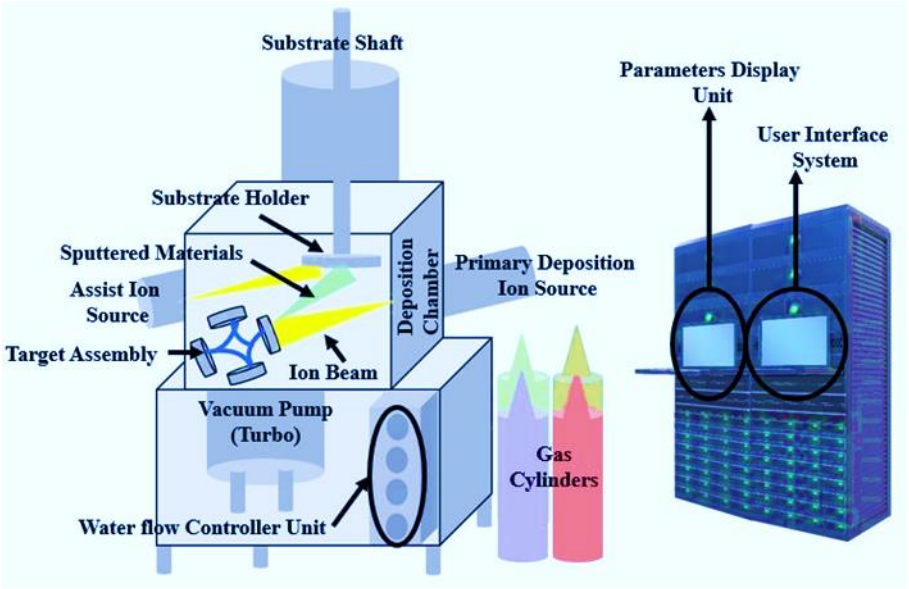

Figure 2.1 *Pictorial schematic of DIBS system.*

The DIBS contains two chambers: 1) the DPC deposition chamber and 2) the LLC load lock chamber The LLC is only used for loading and unloading the sample from the DPC, so there is no need to vent the DPC each time a sample needs to be loaded or unloaded. The deposition process is carried out in the DPC. The gate valve separates the two

chambers. The vacuum in both DPC and LLC is maintained by two separate turbo pumps that rotate at 27 and 51 KRPM, respectively, with support from separate rotary pumps. The DPC and LLC are connected to the vacuum gauges for background and working conditions measurement and monitoring. Within the DPC and LLC, the background pressure is maintained between 10 and 8 mbar. Pyrex glass or stainless steel are used to make the DPC because they are nonmagnetic, easy to repair with welding, non-corrosive, and highly malleable [3]. During the annealing and deposition processes, the substrate holder is placed just below the heater assembly to maintain the desired temperature, which ranges from room temperature to 1000 ^{o}C. The system for cooling the deposition chamber, vacuum pumps, and targets assembly includes the water chiller. The auto controller and various power supply units associated with the DIBS system control deposition parameters in the DIBS system, such as gas pressure, gas composition, deposition temperature, and RF power.

Figure 2.2 *Camera Image of DIBS system.*

Using ion sources developed by Kauffman Robinson [2], the DIBS system generates plasma containing an electron and an Ar+ ion. The

essential particle source which is utilized to create plasma, comprise of three key parts: discharge chamber, grids, and neutralizer with a hollow cathode An RF-powered coil is encircled alumina or quartz chamber before the Ar gas, which will be ionized through inductive coupling, is introduced. The RF field stimulates the free electrons until they attain sufficient energy to generate Ar+ and an electron pair from Ar gas. In order to eject and focus the Ar+ ions, voltages are applied on three grids within the primary source. The neutralizer of the essential particle source gathering is utilized to kill the Ar+ shaft [2]. Figure 2.3 (a) depicts the primary ion source's schematic diagram.

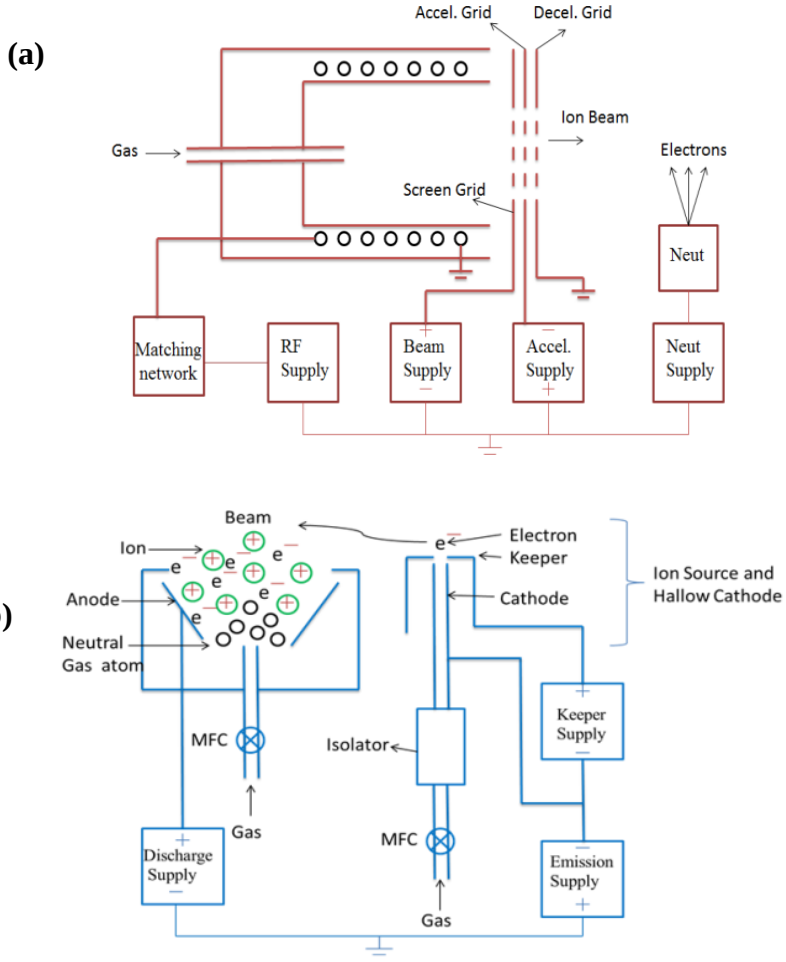

Figure 2.3 *Flow diagram of (a) Primary ion beam and (b) assist ion source.*

As depicted in Figure 2.3 (b), the assist ion source consists of an auto controller, three power supplies (keeper, emission, and discharge), and

a hollow cathode neutralizer assembly. The hollow cathode is ignited by the keeper power supply, which also keeps the cathode hot enough for thermionic electron emission. The electron current generated by the hollow cathode is controlled by the emission voltage, which provides a negative voltage. In order to produce the Ar+ ion beam, the discharge power supply supplies voltage and current to the assist ion source's anode [3].

2.3.2 CVD System

Chemical vapor deposition is one of the prominent technique of deposition of TMD material. In this thesis Quazar tech crystal CVD 1100-4 system is used for growth of MoS_2 monolayer via chemical root [5-6].

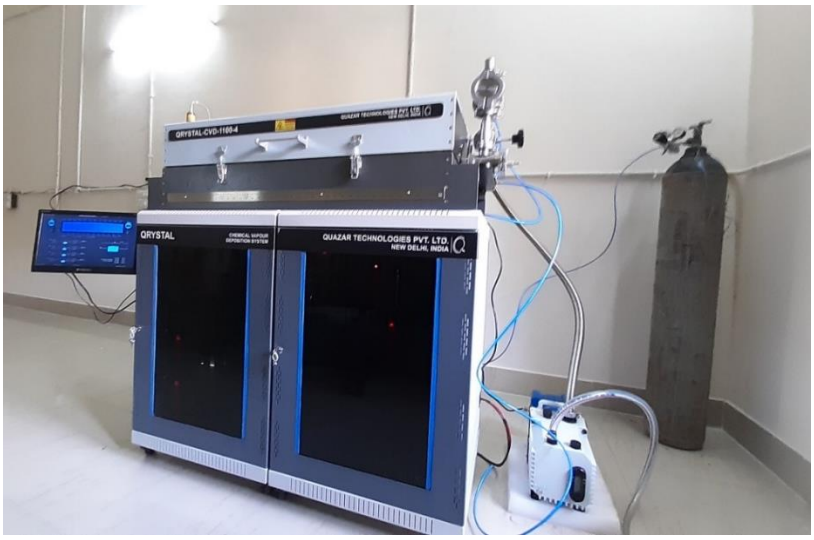

Figure 2.4 *Camera image of Crystal CVD 1100-4 system.*

The system require 200-230 V, 50 Hz single phase electric power supply. The furnace of the system has a shell like construction made up of aluminium to provide sufficient rigidity to the system. The heating tube is made of fused quartz alumina and has 12 different heating zones with PID controllers. The dimension of tube is 45 mm x 1400 mm, while the heating zones are separated by high purity Al_2O_3 for proper insulation between them. Kenthal A1 heating wires are used. Type–N

thermocouples are used for heating the individual zones which provide heating upto 1200 ^{o}C and hence independent heating or manual heating of the zones is possible. Cooling fans are assembled at the back of the furnace for proper cooling. Furnace stand and panel box is attached in the system which also provide space for various controller assemblies and CPU. The maximum working temperature of the tube is 1100 ^{o}C with a ramp rate of 5 ^{o}C/min at highest temperature. Four line gas manifolds using precision mass flow controller (MFC) with digital display is provided for gas supply system. This system is compatible with argon, nitrogen, oxygen, hydrogen and methane with a controlled flow rate of 0-1000 sccm. Pneumatic valves having flow controlled through computer operated MFC are installed for better precision and safety. Vapour gas outlet tube for exhausting the residue gases is assembled along with the vacuum pump assembly for maintaining proper operating pressure inside the tube. The system is compatible with alumina boat sample holder and capable of handling different substrates such as silicon wafer, quartz wafer, and fibre fabrics. The entire system is thoroughly checked for leak (leak rate should be less than 10^{-3} cc/s). On/Off valves are mounted for flashing the gases at 5000 sccm during the cleaning of the tube. High grade corrosion resistant and high pressure stainless steel pipeline connections are provide in the system along with a gas mixing chamber at the gas inlet side of the tube. Computer controlled solenoid valves with dependable pneumatic piston actuators. Different safety features like auto purge, manual valves, python coded step by step recipe, alarmed pop-ups and auto shutdown are incorporated by proper handling of the system by end users.

2.3.3 PVD75 Reactive Magnetron Sputtering System

Figure 2.4 depicts a diagram of the reactive DC magnetic sputtering process. A load lock is included in the system to keep the high vacuum from being disturbed while the sample is being loaded into the chamber. The chamber is outfitted with halogen heat lights to warm the substrates

from RT to 800 °C. Within the DC magnetron sputtering gun that is shuttered, a Lesker 99.99% Zinc target with a diameter of two inches is utilized. Oxygen gas is carried close to the substrate while argon gas is carried to the source. The flow rates are controlled by mass flow controllers. Ion gauges are used to monitor the base pressure, and capacitive nanometers are used to monitor pressure during deposition. A cleaned substrate is initially inserted into the robotic arm or an Inconel substrate holder. The substrate holder is then inserted face down into the robotic arm's load lock. The substrate holder is moved to the column that is connected to the heater assembly after the load lock is pumped down. The gate valve is closed and the robotic arm is released. After that chamber is loaded up with Ar-O_2 gas up to an ideal strain (30 mtorr). A high bad potential is applied across the anodes to speed up the electrons. Plasma will be produced as a result of the ionization of the Ar-O_2 gas atoms by the energetic electrons [7]. The target atoms will be ejected as a result of the Ar+ ions being accelerated toward the cathode and bombarding it. By chemically reacting with oxygen ions, the target material by bombarding their surfaces with energetic Ar+ ions, the sputtered atom forms an oxide film are deposited over the substrate.

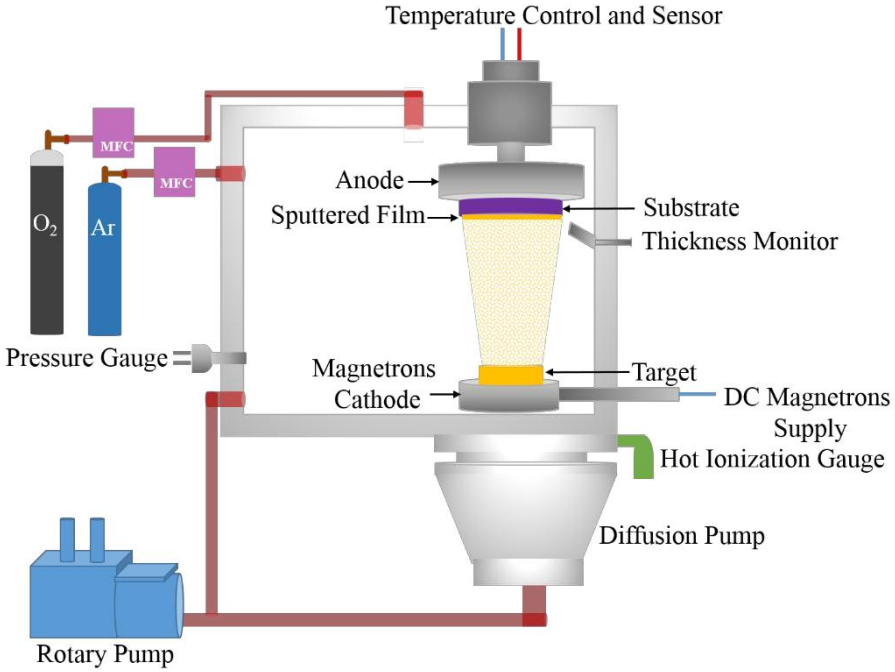

Figure 2.5 *Schematic of reactive magnetron sputtering system.*

Based on the proven PVD 75 platform, the Kurt J. Lesker Company PRO Line PVD 75 is the next-generation thin film deposition system. With improved system base pressures and pump down times, PRO Line PVD 75 builds on the design's successes. Among the key benefits of this innovative, world-class design are an industry-leading software control system with advanced programming capabilities, automatic substrate loading, and numerous features for optimized thin film performance. In addition to a dependable, uninterruptible processing module that enables process completion regardless of the state of the computer user interface, KJLC's software makes recipe creation simple. One of Kurt J. Lesker's most adaptable thin film deposition systems, the PRO Line PVD 75 offers thermal evaporation, magnetron sputtering, and electron beam deposition as single or multiple techniques [8].

Figure 2.6 *Camera image of Proline PVD75 reactive magnetron sputtering system.*

https://www.lesker.com/newweb/vacuum_systems/jpg/Photo/PhotoSY-K-ProLinePVD75-OpenFrameStandard-001.jpg

Only KJLC offers Mag-Keeper sputter sources with a magnetically coupled target and zero o-rings in the cathode body, making it simple to change targets. It can run at power densities up to 200 watts per square inch (depending on the material) thanks to its cooling well design. Sputter targets up to 0.375" thick with this cathode. This cathode can operate at a temperature of less than 1 mTorr in the absence of a hold-down clamp or dark space shield. Standard flip or swing shutters necessitate additional cross-contamination shielding, which is not necessary with the novel dome shutter design. KJLC E-bar sources are likewise intended to kill pointless o-rings, seals, and feedthroughs to bring down pump down times and give phenomenal base tensions. The KJLC E-beam source only requires three feedthroughs, and the absence of a dynamic water-to-vacuum o-ring seal significantly reduces the likelihood of a water leak in the vacuum chamber.

In order to achieve better uniformity, the thermal evaporation sources that are normally located on the substrate fixture have been moved to the fixture's outer edges. The fixtures permit source adjustment of up to an inch for application-specific optimization [9].

Substrates

- Suitable for substrates with a diameter of up to 6 inches (150 mm)
- 20 RPM, 850°C heat or water cooled
- Up to 100W RF bias
- Automated transfer

Ion source

eH400 End-Hall permanent magnet or KDC40 gridded ion source:

- KDC40 Gridded ion source enables precise beam shaping with interchangeable ion optics and independent operation of important ion beam properties
- eH400 End-hall source is a versatile ion source that is capable of high current, low energy ion cleaning or etching while minimizing damage to substrate surfaces.

2.3.4 E-beam Evaporation System

E-beam evaporation is another method of vapor deposition used to produce thin films. The metal pellets that are the source material are evaporated with an electron beam, and the condensed material forms a thin film on the cooled substrate. A more advanced version of thermal evaporation is the e-beam evaporation method. In E-beam evaporation, the source material is heated by an electron beam, whereas in thermal evaporation, the material is heated resistively [10-11]. E-beam involves bombarding a target anode with an electron beam produced by a charged tungsten filament in a high vacuum. The anode material covers everything in the vacuum chamber (within sight) in a thin layer as these atoms precipitate into a solid. Thermionic emission, field electron emission, and the anodic arc method are all methods that can produce electron beams. The evaporation material is targeted by accelerating the generated electron beam to a high kinetic energy. The electrons will rapidly lose energy upon striking the evaporation material. Interactions with the evaporation material convert the electrons' kinetic energy into other forms of energy. The evaporation material is heated by the generated thermal energy, causing it to melt or sublimate. The subsequent fume can then be utilized to cover surfaces [12].

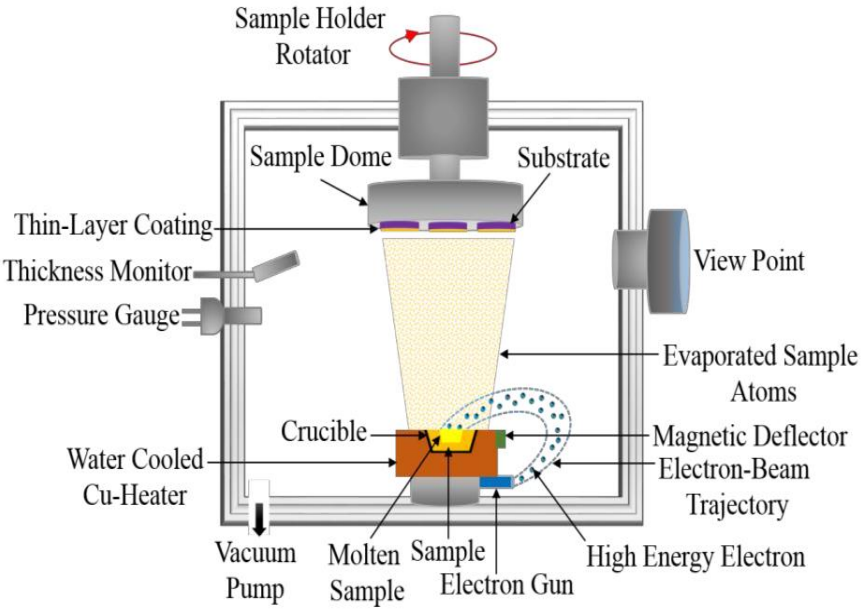

Figure 2.7 *Schematic of E-beam evaporation system.*

The following are the primary components of an E-beam evaporation system:

- Substrate holder
- Electron Beam Evaporation Unit
- Substrate and E-Beam Unit Cooler System
- Pressure Gauge
- Thickness Monitor Unit
- Vacuum Pump
- Chiller and Other Parameter Controlling Units

The following are important steps in the E-Beam Evaporation process. Initially, the crucible is filled with the source material, typically graphite. The substrate is then loaded with its face down above the sample, and the entire chamber is kept at an extremely high vacuum of 10^{-6} Torr. The source material is heated to it's evaporate point by heating the filament beneath the crucible with a high current once the desire chamber condition has been reached. A high electric field accelerates the hot electrons that are emitted from the filament, which results in an emission current. In order to bombard the source material and cause its evaporation, an electromagnetic coil is used to control the size and shape of the emitted electron beam. Atoms that have been vaporized condense on the chamber wall and the cooled substrate.

2.4. Brief introduction of MATLAB

MATLAB is a programming platform made for scientists and engineers to analyze and design products and systems that change our world. The MATLAB language, a matrix-based language that enables the most natural expression of computational mathematics, is the core of MATLAB. It is equipped for dissecting information, creating calculations, and Make models and applications from examination to creation by sending installed gadgets, as well as coordinating with

Simulink and Model-Based Plan. Using a variety of modeling approaches and levels of abstraction, engineers can collaborate to describe, analyze, simulate, and verify their multidomain systems with the help of MATLAB and Simulink, which make it easier to explore design space and design semiconductor devices from the top down. Software, analog, digital, RF, and thermal are examples of domains; and the level of abstraction can vary from transistor to algorithm [12]. In this work MATLAB-Simulink version R15a is used for the analytical modelling.

2.5. Thin Film and Device Characterization tools

In this research work, the characterization of thin film and performance analysis of the fabricate PD require different measurement tools. The following sub-sections are described these system in detailed manner.

2.5.1 Spectroscopic Ellipsometry Measurement System

The thickness and energy bandgap of thin films produced in any deposition systems was measured using the M-2000D J. A. Woollam Variable Angle Variable Wavelength Spectroscopic Ellipsometer, which allows for measurements at a variety of angles to the sample plane. The Variable Angle Variable Wavelength Spectroscopic Ellipsometer is depicted in Figure 2.8. Ellipsometry is used to measure the polarization shift that occurs when light reflects or transmits from a material structure [13]. The symbols for the polarization change's amplitude ratio and phase difference are, respectively. The measured reaction is influenced by the optical properties and thickness of each particular material. Consequently, ellipsometry is mostly used to calculate film thickness and optical constants. This method can also be used to estimate the composition, crystallinity, roughness, doping concentration, and other material parameters associated with a change in optical response.

Each sample's optical properties were determined by measuring light incident at various points on the sample multiple times. The optical bandgap of the examples is determined utilizing the ingestion coefficient

that outcomes from fitting the Ψ and Δ as opposed to differing occurrence frequencies. Because the sample and film are largely transparent, the Ellipsometer calculates the transmission coefficient. The energy bandgap of the developed film is immediately derived from the transmission coefficient of the bare substrate, which was measured prior to the film being deposited [14]. The primary components of the ellipsometry system are a light source, polarization generator, sample, polarization analyzer, and detector. The polarization generator and analyzer are constructed with polarizers, compensators, and phase modulators to alter polarization. A different sample stage called transmission stage is used for measuring the transmission spectra of the thin film.

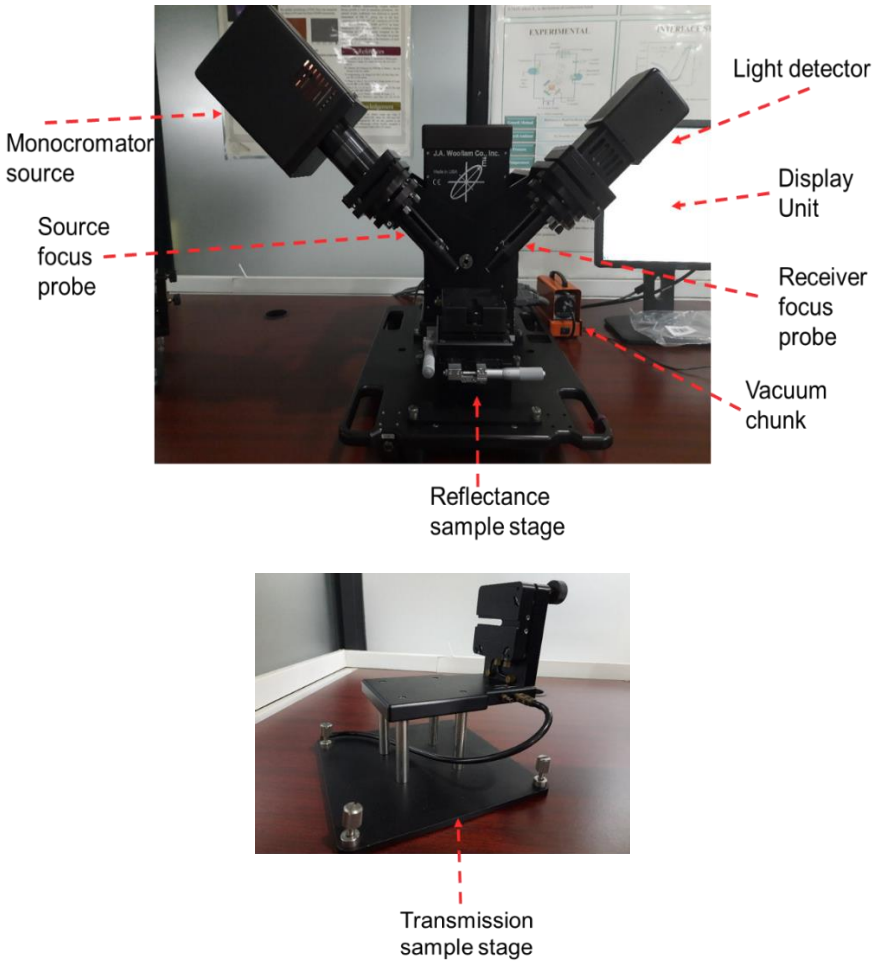

Figure 2.8 *Camera image of Variable angle spectroscopic ellipsometry measurement system.*

2.5.2 Optical Microscopy Measurement System

In this thesis, Carl Zeiss Axio Vert A1 inverted microscope for material is used for optical imaging and surface morphological analysis of the MoS_2 monolayer and device dimension measurement. The system is a powerful, inverted, and small microscope. Numerous traditional and cutting-edge contrast techniques make it possible to examine substantial, heavy samples. In reflected light, you can easily switch between brightfield, darkfield, DIC, C-DIC, fluorescence, and polarization contrast. IT utilize phase contrast, polarization, and brightfield for transmitted light. Alternately, you might decide to combine a number of contrast methods to get the most information. A change in objectives is automatically recognized by the 5x encoded nosepiece turret [15-16].

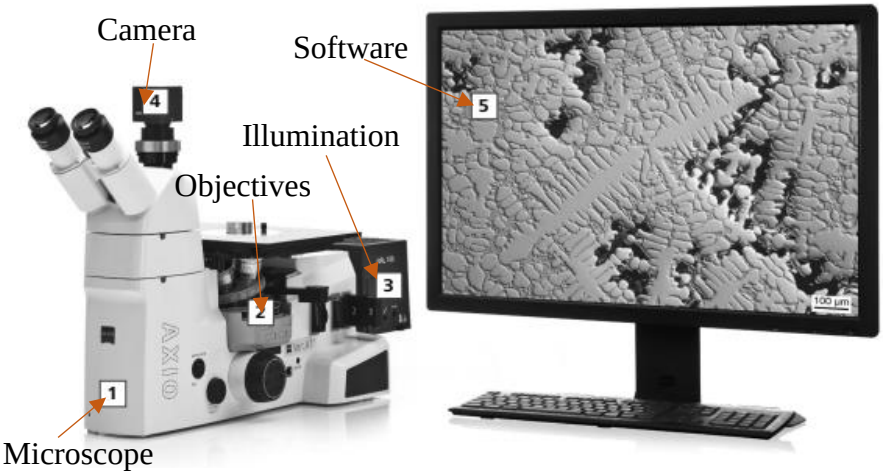

Figure 2.9 *Image of Zeiss Axio Vert A1 Inverted Microscope.*

Additionally, it makes it possible to save and retrieve light intensity values using a light manager. You can accurately quantify your structure and evaluate the materials' properties and quality. Improve preparation or production procedures and gain valuable new insight and then take the necessary steps. The system has a magnigying setup with sample stand, vibration free table stand and an assembled computer system with microscope compatible software. The system is provided with upright frame with built in transformer and power supply. 5X zoom capability having a magnifying level of 5X, 10X, 25X, 50X and 100X. Frame

mounted LED illumination intensity control, with multi step manual focus drive. Built-in and adjustable color coded aperture and field diaphgram. It has a rotatable 4 position turrets and 5 position rotatable universal nosepiece. 360^{o} rotatable polarizer and analyser with 3 click stop of 0^{o}, 45^{o}, and 90^{o}.

2.5.3 Raman Spectroscopy System

A Horiba LabRam HR Evolution spectrometer close-fitting by liquid nitrogen chilled Charge Coupled Device (CCD) detector is utilized for Raman spectroscopy measurement of the dropped MoS_2 monolayer. The true confocal Raman microscope enables the most precise images and analyses to be obtained with speed and confidence. The LabRAM HR Evolution Raman microscopes are ideal for both micro and macro measurements and offer advanced confocal imaging capabilities in 2D and 3D. The LabRAM HR Evolution is the best Raman spectroscopy instrument because it guarantees high performance and is easy to use. Standard Raman analysis, Photoluminescence (PL), Tip Enhanced Raman Spectroscopy (TERS), and other hybrid techniques all make extensive use of them. Similarity with a large number of laser frequencies and the chance of mounting up to three identifiers empowers the estimation frequency reach to be stretched out from 200nm to 2200nm. The best option for UV Raman analysis at wavelengths below 400 nm is the optimized UV configuration [17]. Because of this performance, additional spectroscopic methods like UV Raman, resonance Raman, and photoluminescence are now available, making it possible to thoroughly characterize samples made of a wide variety of materials. The exclusive SWIFTTM and DuoScanTM fast Raman imaging technologies are included in the LabRAM HR Evolution.

DuoScan is a confocal imaging mode, with high accuracy, super quick rastering mirrors making variable measured laser large scale spots, and furthermore permitting nano-step planning from profound UV to NIR.

Confocal Raman mapping is available with SWIFTTM, and CCD integration times are as low as 1 millisecond per point. The LabRAM

HR Development joins basic admittance to exceptionally low frequencies down to $5cm^{-1}$ with a high throughput single stage spectrometer, utilizing the ULF Module. Additional sample characterization in a spectral region that is rarely accessible with other basic spectrometers is now possible thanks to the most recent generation of notch and bandpass filters. For analytical measurements, system offer comprehensive Raman spectroscopy solutions. These include transmission Raman analyzers, specialized in situ process Raman spectrometers, miniaturized Raman instruments for high volume OEM manufacturers, hybrid Raman systems like AFM-Raman, and modular Raman systems [18].

Figure 2.10 *Image of LabRam Raman Spectroscopy System.*

https://www.horiba.com/int/scientific/products/detail/action/show/Product/labram-hr-evolution-1083/#gallery-002

2.5.4 Solar Cell Tester System

The solar cell tester is essentially an integrated system that includes an I-V measurement system and a solar simulator. Figure 2.11 depicts the photographic image of the solar tester. Here is a brief explanation of the various units of the solar cell tester:

(a) The Connection and Sample Placement Stage: The sample is positioned on the chuck. The connection to the solar cell that is currently being measured is then made using adjustable pins. By pressing the vacuum button, the sample that has been placed on the chuck is held in place with great force.

b) Unit for the Temperature and Vacuum Controller: The analysis of the operation temperature is crucial because it has a significant impact on the performance of the solar cell. Additionally, this system makes it possible to alter the device under measurement's temperature. By pressing the vacuum button, the sample that has been placed on the chuck is held in place with great force.

Figure 2.11 *Image of Solar Cell Tester System.*

c) Unit for the Intensity Controller: The SCs are operated in non-STC, just like in real-world applications. This means that the level of solar irradiance varies depending on where you are, the weather, and the time of day. The solar simulator can be used to analyze solar cells under different levels of solar irradiance.

d) System of Measurement: Keithley is utilized for estimating I-V

Attributes of the Cell in dim and light condition.

A portion of the striking elements of the Sunlight based cell analyzers are [19]:

- Computer-controlled, fully automated and integrated system.
- Stability-enhancing feedback control and measurement of light intensity.

- A variety of adaptable cell test fixture configurations, including the option of controlling the cell temperature (from -10°C to 70°C ±0.5°C).
- The genuine four-probe cell contacting method.
- Temperature controlled throw with vacuum hold.
- The capability to normalize the data points to Standard Test Conditions (STC) or other user-specified conditions for intensity and temperature measurements.
- Cutting-edge I-V curve software with three distinct curve fitting models and 17 distinct weight function models, as well as potent curve fitting algorithms.
- The capacity to identify various cell parameter Thermal Coefficients.

Table 2.1 contains a list of some of the solar cell tester's technical specifications [20].

Table 2.1: *Technical specifications of solar cell tester*

Feature description	**Specification**
Type of lamp	Xenon Short Arc
Lamp Power	150 W
Max. Illuminated area	2” (50 mm) x 2” (50 mm)
Air Mass	AM1.5G Standard: AM1.5D or AM1 optional
Adjustment Range of light intensity	100 mW/cm^2 +/- 15%
Spectral Range	350 nm - >2,700 nm
Spatial Non-uniformity of irradiance*	≤ 2% or better
Degree of Collimation	≤ 2 degrees
Phase/Voltage/Frequency	Single Phase/110-220 AC Volts /50-60 Hz
Max. Power Consumption (W)	0.5 KVA

The instrument that is used to measure the solar cell's I-V and PV characteristics in both dark and light conditions is called a solar cell tester. The performance parameters, such as short-circuit current, open-circuit voltage, fill factor, maximum peak power, voltage and current corresponding to maximum power, shunt and series resistance, and conversion efficiency, are directly derived from these characteristics. For various purposes, various AM filters can be utilized in this system to measure the performance of solar cells.

2.5.5 Incident Photon Conversion Efficiency (IPCE) System

The PVE300 is a complete system for figuring out the IQE and spectral response of solar cells. The PVE300 is a crucial component in research and production-line quality processes due to its ability to characterize photovoltaic devices and materials. The PVE300 makes it possible to quickly and precisely determine the characteristics of solar cells by utilizing a monochromatic probe and NMI traceable, calibrated reference diodes. Measurement of total reflectance and transmittance Convert EQE to internal quantum efficiency. Measurement of spectral response/external quantum efficiency (IPCE). Monochromatic Probe of the PVE300 System, a TMc300, 300mm focal length monochromator and a dual Xenon/quartz halogen source provide optimal illumination from the UV to the NIR. To enable the measurement of total reflectance and total transmittance, the DTR6 integrating sphere is mounted on an optical rail to the upper portion of the PVE300 chamber. Constant Current Power is required for each light source (xenon, quartz halogen, and solar simulator) [21].

In this work, the Bentham PVE300 Incident Photon Conversion efficiency (IPCE) system was used to characterize the spectral photoresponse of fabricated UV PDs. This is important for determining the Device characterization is typically carried out with the PVE300 system in both the research industry and academia. Photovoltaic devices can be quickly and precisely measured with this tool [22]. The Bentham PVE300's primary features are as follows:

(i) Direct device spectral photoresponse calculation

(ii) The up-front calculation of reflectance and transmittance.

(iii) The extensive operating range (300-2500 nm).

(iv) USB based fully automated control software for Windows.

(v) Lock-in-based detection employing a transformer or amplifier.

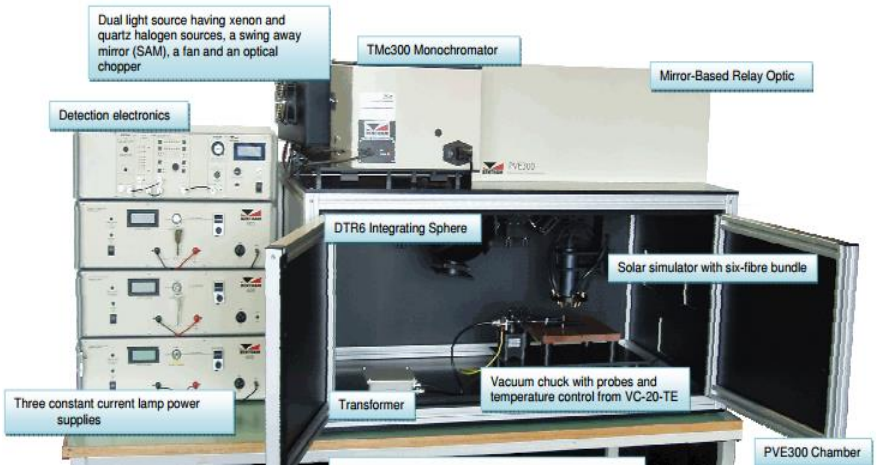

Figure 2.12 *Image of Incident Photon Conversion Efficiency (IPCE) System.*

2.5.6 I-V and Temporal Response Measurement System

In the present thesis, the I-V analysis of the PD in photon incidence condition for different monochromatic wavelength is measured by utilizing Keithley 2612A system [23]. The 2612A System SourceMeter instruments can be used to build multi-channel I-V test systems or as benchtop I-V characterization tools. The embedded TSP Express Software Tool in Series 2600A instruments for benchtop use makes it simple and quick to perform common I-V tests without having to install or program software. The highest throughput in the industry and the lowest cost of test are provided by the Series 2600A's Test Script Processor (TSP) architecture for system-level applications and other new features like parallel test execution and precision timing [24].

- The following products belong to the family: 1 fA to 50 Ampere, and 1 volt to 200 volt
- Faster test times and the ability to record transient device

- behavior are provided by 20,000 rdg/s.
- USB port for saving data and test scripts for precise timing and channel synchronization (500 ns).
- High-speed data transfer is supported by LXI Class C compliance.

Apart from 2612A, the system also use Keithley DMM 6500 ½ system for measuring the time stamp during the variation of PD current between dark and photocurrent. Transient capture, data visualization, and analysis are just some of the additional measurement capabilities offered by this touchscreen bench 6.5-digit multimeter. There are fifteen built-in measurement functions, including temperature, capacitance, and digitizing. With great precision and high resolution, measure low current and resistance on low-power devices. Utilize the integrated 16-bit digitizer to capture transient signals. To get the most out of the test data, look at two measurements at once. There is no need for additional instruments with the DMM6500 6.5-digit multimeter [25].

Figure 2.13 *Image of Keithley 2612A and DMM 6500 ½ System.*

2.6. Conclusion

In this chapter, details of different deposition and measurement system are discussed which are used for during the analysis of fabricated PD.

2.7. References

[1] V. Garg, B. S. Sengar, V. Awasthi, and P. Sharma, "Localized surface plasmon resonance on Au nanoparticles : tuning and exploitation for performance enhancement in ultrathin

photovoltaics," RSC Advances, 6, 26216-26226, 2016.

[2] H. R. Kaufman, R. S. Robinson, and R. I. Seddon, "End-Hall ion source," Journal of Vacuum Science & Technology A: Vacuum, Surfaces, and Films, 5, 4, 2081-2084, 1987.

[3] F. Quaranta, A. Valentini, F. R. Rizzi, and G. Casamassima, "Dual-ion-beam sputter deposition of ZnO films," Journal of Applied Physics, 74, 1, 244-248, 1993.

[4] V. Awasthi, S. K. Pandey, S. Kumar, C. Mukherjee, M. Gupta, and S. Mukherjee, "Evaluation of the band alignment and valence plasmonic features of a DIBS grown Ga-doped $Mg_{0.05}Zn_{0.95}O$/CIGSe heterojunction by photoelectron spectroscopy," Journal of Physics D: Applied Physics, 48, 48, 485305, 2015.

[5] C. Patel, R. Singh, M. Dubey, S. Pandey, S. Upadhyay, V. Kumar, S. Sriram, M. T. Htay, S. Pakhira, V. Atuchin, and S. Mukherjee, "Large and Uniform Single Crystals of MoS_2 Monolayers for ppb-level NO_2 Sensing," ACS Applied Nano Materials, 5, 9415-9426, 2022.

[6] T. Mondal, A. K. Bhowmick, and R. Krishnamoorti, "Controlled synthesis of nitrogen-doped graphene from a heteroatom polymer and its mechanism of formation," Chemistry of Materials, 27, 3 716-725, 2015.

[7] B. Mandal, A. Biswas, Aaryashree, D. S. Sharma, R. Bhardwaj, M. Das, M. A. Rahman, S. Kuriakose, M. Bhaskaran, S. Sriram, M. T. Htay, A. K. Das, and S. Mukherjee, "π-conjugated amine-ZnO nanohybrids for the selective detection of CO_2 gas at room temperature," ACS Applied Nano Materials, 1, 6912−6921, 2018.

[8] L. Y. Beliaev, E. Shkondin, A. V. Lavrinenko, and O. Takayama, "Optical, structural and composition properties of silicon nitride films deposited by reactive radio-frequency sputtering, low pressure and plasma-enhanced chemical vapor deposition," Thin Solid Films, 763, 139568, 2022.

[9] https://www.lesker.com/process-equipment-division/thin-film-

systems/pro-line-pvd-75-deposition-platform.cfm

[10] M. A. Khan, P. Kumar, M. Das, M. T. Htay, A. Agarwal, and S. Mukherjee, “Drain current optimization in DIBS-grown MgZnO/CdZnO HFET,” IEEE Transactions on Electron Devices 67, 6, 2276-2281, 2020.

[11] S. Nirantar, T. Ahmed, G. Ren, P. Gutruf, C. Xu, M. Bhaskaran, S. Walia, and S. Sriram, “Metal–air transistors: Semiconductor-free field-emission air-channel nanoelectronics,” Nano letters, 18, 12, 7478-7484, 2018.

[12] R. Singh, R. Bhardwaj, G. Siddharth, P. Kumar, and S. Mukherjee, “Analytical study of sputter-grown ZnO-based pin homojunction UV photodetector,” IEEE Sensors Journal, 21, 6, 7515-7521, 2020.

[13] M. Dubey, G. Siddharth, R. Singh, C. Patel, S. Kumar, M. T. Htay, V. V. Atuchin, and S. Mukherjee, “Influence of Substrate Temperature and Sulfurization on Sputtered $Cu_2SnGe(S,Se)_3$ Thin Films for Solar Cell Application,” IEEE Transactions on Electron Devices, 69, 5, 2488–2493, 2022.

[14] R. Singh, G. Siddharth, R. Bhardwaj, and S. Mukherjee, “Structural and optical study of sputtered grown Sb doped ZnO thin film,” IEEE 21st International Conference on Nanotechnology (NANO), 474-477, IEEE, 2021.

[15] S. Singh, N. Resnina, S. Belyaev, A. N. Jinoop, A. Shukla, I. A. Palani, C. P. Paul, and K. S. Bindra, “Investigations on NiTi shape memory alloy thin wall structures through laser marking assisted wire arc based additive manufacturing,” Journal of Manufacturing Processes, 66, 70-80, 2021.

[16] A. K. Litoria, C. A. Figueroa, L. T. Bim, C. I. Pruncu, A. A. Joshi, and S. S. Hosmani, “Pack-boriding of low alloy steel: microstructure evolution and migration behaviour of alloying elements,” Philosophical Magazine, 100, 3, 353-378, 2020.

[17] C. Rani, M. Tanwar, T. Ghosh, S. Kandpal, D. K. Pathak, A. Chaudhary, P. Yogi, S. K. Saxena, and R. Kumar, “Raman

Spectroscopy as a Simple yet Effective Analytical Tool for Determining Fermi Energy and Temperature Dependent Fermi Shift in Silicon," Analytical Chemistry, 94, 3, 1510-1514, 2022.

[18] V. Gupta, D. K. Pathak, S. Chaudhary, and R. Kumar, "Raman imaging for measuring homogeneity of dry binary blend: Combining microscopy with spectroscopy for technologists," Analytical Science Advances, 1, 2, 89-96, 2020.

[19] "Solar Cell Testers: Photo Emission Technology," [Online]. Available: http://www.photoemission.com/celltesters.html.

[20] G. Siddharth, R. Singh, V. Garg, B. S. Sengar, M. Das, B. Mandal, M. T. Htay, M. Gupta, and S. Mukherjee, "Investigation of DIBS-deposited CdZnO/ZnO-based multiple quantum well for large-area photovoltaic application," IEEE Transactions on Electron Devices, 67, 12, 5587-5592, 2020.

[21] R. Bhardwaj, P. Sharma, R. Singh, and S. Mukherjee, "Sb-Doped *p*-MgZnO/*n*-Si Heterojunction UV Photodetector Fabricated by Dual Ion Beam Sputtering," IEEE Photonics Technology Letters, 29, 14, 1215-1218, 2017.

[22] R. Bhardwaj, P. Sharma, R. Singh, M. Gupta, and S. Mukherjee, "High Responsivity $Mg_xZn_{1-x}O$ Based Ultraviolet Photodetector Fabricated by Dual Ion Beam Sputtering," IEEE Sensors Journal, 18, 7, 2744-2750, 2018.

[23] J. Agrawal, T. Dixit, I. A. Palani, and V. Singh, "Electron depleted ZnO nanowalls-based broadband photodetector," IEEE Photonics Technology Letters, 31, 20, 1639-1642, 2019.

[24] R. Singh, C. Patel, P. Kumar, M. Dubey, S. Sriram, and Shaibal Mukherjee, "High Detectivity and Fast MoS_2 Monolayer MSM Photodetector," ACS Applied Electronic Materials, 2022.

[25] "Keithley DMM6500 6.5 Digit Multimeter with Graphical Touchscreen," [Online].
Available: https://www.tek.com/en/products/keithley/digital-multimeter/dmm6500.

Chapter 3

Analytical study of sputter-grown ZnO-based *p-i-n* homojunction UV photodetector

3.1. Introduction

In the recent past years, ultraviolet (UV) photodetectors (PDs) have emerged as a widely developed and extensively studied topic in the field of semiconductor devices [1-3]. Among all the materials available for fabricating the UV PDs, the ZnO-based material systems have become increasingly popular due to their inherent benefits. ZnO has a wide energy bandgap (3.37 eV), which can be further enhanced by the incorporation of Mg and Be [4-6], large exciton binding energy (60 meV), high radiation hardness, high chemical stability and abundancy on earth [5, 7]. Several architectures for ZnO-based photodetectors are developed such as metal-semiconductor-metal (MSM), photoconductors, Schottky, *p-n*, and *p-i-n* [8-15]. Amid of these all, the *p-i-n* homojunction structure is a more desirable choice owing to the superior interface quality possessed integrally by the structure making the junction electrically and metallurgically superior. Due to the presence of *i*-layer in *p-i-n* architecture, it provides more efficient absorption of incident photons, as compared to that in conventional *p-n* architecture [16-18].

From the beginning of exploring ZnO as a semiconductor material, obtaining good and reproducible *p*-type conduction in ZnO materials which had remained a bottleneck due to low solubility of dopants and various compensation effects [2, 7, 19, 20]. However, a reproducible and reliable dual ion beam sputtered (DIBS) grown *p*-type Sb-doped ZnO has been achieved and reported in our earlier work [21]. DIBS offer several advantages over other conventional deposition techniques such as superior film growth quality with better compositional stoichiometry [7, 14, 21].

Due to the unavailability of rigorous experimental as well as simulation reports in the literature on ZnO-based *p*-*i*-*n* homojunction UV PD, a comprehensive analytical model is essential to assess the performance metrics of such UV PD with varied material thickness layers. Experimental reports are available in the literature for ZnO based *p*-*i*-*n* homojunction photodetector [16, 22], however, these reports have not detailed the performance variation with material thickness. To the best of the authors' knowledge, the detailed analytical modeling to estimate the performance of ZnO homojunction based *p*-*i*-*n* UV PD is not available in the literature.

Here, report an analytical model for ZnO-based *p*-*i*-*n* homojunction UV PD and validation with the experimental results of UV PDs available in the literature. The model is helpful in analyzing the performance, in terms of dark current and responsivity, of homojunction *p*-*i*-*n* UV PDs and obtaining the optimal thickness of Sb doped *p*-type ZnO (SZO) and undoped ZnO (*i*-ZnO) on top of Ga doped *n*-type ZnO (GZO) before the actual fabrication of the device grown by DIBS.

3.2. Device Structure and Model Formulation

The structure under consideration is a homojunction *p*-SZO/*i*-ZnO/*n*-GZO photodiode grown on sapphire substrate. A schematic diagram of the UV PDs is shown in Figure 3.1 with corresponding energy band diagram at thermodynamic equilibrium. In the *p*-*i*-*n* structure, each region has different carrier concentration and carrier mobility, as mentioned in Table 3.1. The top SZO layer acts as a transparent window for transmission of incident photons, which are intended to be absorbed in the active ZnO region [16]. The homojunction energy band diagram is drawn by applying Anderson's classical theory [23].

3.2.1 Modeling of current density

The functionality of PD is strongly affected by the total current density generated by the thermally created carriers. In the following section,

various current density components of homojunction *p-i-n* UV PDs are modeled which in summation gives the dark current density of the device. The major current density components are as follows:

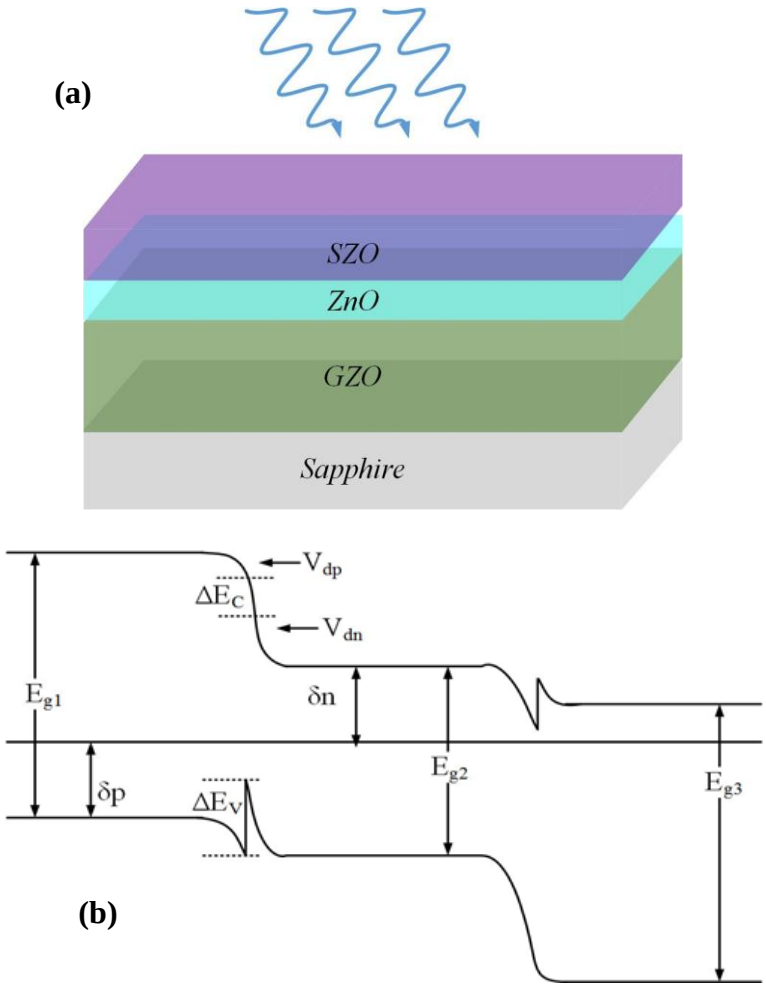

Figure 3.1 *(a) Device Structure and (b) Energy Band Diagram of Homojunction p-i-n UV PD.*

3.2.1.1 Diffusion current density (J_{diff})

The thermally diffused minority carrier current density is generated as a result of the diffusion of charge carriers due to the concentration gradient [24, 25]. The equation governing this current density component in a *p-i-n* PD is given in equations (1-3) [24]:

$$J_{diff} = (J_i)_p + (J_p)_i \tag{3.1}$$

$$(J_i)_p = \frac{qn_i{}^2}{N_A}\sqrt{\frac{\mu_n KT}{q\tau_n}} \left(\frac{\gamma_n \cosh\left(\frac{t_p - x_p}{L_n}\right) + \sinh\left(\frac{t_p - x_p}{L_n}\right)}{\cosh\left(\frac{t_p - x_p}{L_n}\right) + \gamma_n \sinh\left(\frac{t_p - x_p}{L_n}\right)}\right)\left[exp\left(\frac{qV}{KT}\right) - 1\right] \quad (3.2)$$

$$(J_p)_i = \frac{qn_i{}^2}{N_i}\sqrt{\frac{\mu_p KT}{q\tau_p}} \left(\frac{\gamma_p\, cosh\left(\frac{d-x_i}{L_p}\right) + sinh\left(\frac{d-x_i}{L_p}\right)}{cosh\left(\frac{d-x_i}{L_p}\right) + \gamma_p\, sinh\left(\frac{d-x_i}{L_p}\right)}\right)\left[exp\left(\frac{qV}{KT}\right) - 1\right] \quad (3.3)$$

$(J_p)_i$ and $(J_i)_p$ are the diffusion components of current due to the injection of electrons and holes in the *p*- and *i*- regions diffused from *i*- and *p*-regions, respectively, summing up the total diffusion current. μ_n, μ_p, τ_n, and τ_p are the mobility and carrier lifetime values of electron and hole, respectively. N_i and N_A are the concentration of undoped ZnO region and acceptors in SZO region, respectively, n_i is the intrinsic carrier concentration of the ZnO material system at thermodynamic equilibrium; *T* is the temperature in Kelvin; *q* is charge of electron; *K* is the Boltzmann constant; *V* is the bias voltage; t_p and *d* are the thicknesses of SZO and ZnO layers, respectively; γ_p and γ_n are the surface to bulk recombination velocities for *p*- and *i*-regions; L_p and L_n are the diffusion lengths for electrons and holes, respectively; and x_p and x_i are the widths of the depletion region on the *p*- and *i*-regions, respectively. The surface to bulk recombination velocities are given by equations (4-5) [18]:

$$\gamma_n = \frac{S_n L_n}{D_n} \quad (3.4)$$

$$\gamma_p = \frac{S_p L_p}{D_p} \quad (3.5)$$

where S_n and S_p are the surface recombination velocity of electrons and holes, respectively at interface of *p*- and *i*- regions, and D_n and D_p are the diffusion coefficients of electrons and holes, respectively.

3.2.1.2 Generation-recombination current density (J_{gr})

The defects lying within the depletion region act as intermediate states for thermal generation and recombination of charge carriers [19]. These transition states are called Shockley-Read centers. The existing electric field in the depletion region separates out the carriers photo-generated in the region. The transport of these photo generated carriers across the homojunction under concern is strongly affected by the trap levels at the interface inside the depletion region [18]. The transport of these carriers is termed as generation-recombination current. This generation-recombination current density is governed by Shockley-Read-Hall equation [26].

J_{gr} arising in the depletion region can be formulated as given in equations (6-8):

$$J_{gr} = (J_n)_{gr} + (J_p)_{gr} \tag{1.6}$$

$$(J_n)_{gr} = \frac{2KTn_i x_n}{\tau_n V_{th} V} \sqrt{\frac{3KT}{m_n{}^*}} \tag{3.7}$$

$$(J_p)_{gr} = \frac{2KTn_i x_p}{\tau_p V_{th} V} \sqrt{\frac{3KT}{m_p{}^*}} \tag{3.8}$$

where $m_p{}^*$ and $m_n{}^*$ are the effective mass values of hole and electron in the *p*- and *i*-regions, respectively; V_{th} is the thermal carrier velocity, and τ_p and τ_n are Shockley-Read-Hall recombination lifetimes of holes and electrons, respectively.

3.2.1.3 Tunneling current density (J_{tun})

The two components of tunneling current density depend on two tunneling mechanisms such as trap-assisted tunneling and quantum mechanical tunneling. The overall tunneling current is actually the sum of the current provided by the individual tunneling mechanisms. When minority carriers tunnel from the occupied trap states on the quasi-neutral side to vacant band states on the other side of the junction

through trap states present in the depletion region, then the mechanism is called trap-assisted tunneling [24]. These intermediate energy states, commonly known as the trap centers, are created by the impurities present in the material. The trap-assisted tunneling component of current density is governed by trap states, as proposed by Gopal *et al* [27]. When the width of the depletion region is sufficiently thin, then electrons and holes having energy below the barrier potential can cross the interface by quantum mechanical tunneling. The components of the current stand up from quantum mechanical tunneling can be obtained by numerical model based on the WKB approximation [25]. For the *p-i-n* PD, quantum mechanical tunneling is the dominating phenomenon. The resultant tunneling current density is given by equations (9-11) [28]

$$J_{tun} = (J_{sn})_{Tun} + (J_{sp})_{Tun} \tag{2.9}$$

$$(J_n)_{Tun} = A^* T^2 p_n \, exp\left(-\frac{V_{dn}+\delta_n}{kT}\right) \tag{3.10}$$

$$(J_p)_{Tun} = A^* T^2 p_p \, exp\left(-\frac{V_{dp}+\delta_p}{kT}\right) \tag{3.11}$$

where A^* is the effective Richardson's constant [29], δ_n is the energy difference between the conduction band minima and Fermi level of *i*-region; δ_p is the energy difference between Fermi level and valence band maxima of *p*-region; p_n and p_p are the tunneling factors for electrons and holes, respectively. The total built-in potential (V_d) is given by equation (12) in terms of V_{dn} and V_{dp} which are represented in the energy band diagram shown in Figure 3.1(b).

$$V_d = V_{dn} + V_{dp} \tag{3.12}$$

Since the entire discussion is about UV PDs, the band to band (BTB) direct tunneling is insignificant due to its major role at high reverse bias in narrow bandgap semiconductors [27].

3.2.2 Modeling of quantum efficiency

The three components contributing towards the analytical modeling of the net quantum efficiency (η) of the *p-i-n* photodetector arises from the three different regions of the structure i.e. neutral *n*-region (η_n), neutral *p*-region (η_p), and *i*-region (depletion region) (η_{dep}). The equations (13-18) describing these components of efficiency are [24]

$$\eta = \eta_{dep} + \eta_n + \eta_p \tag{4.13}$$

$$\eta_{dep} = (1 - R_p)(1 - R_i)(1 - R_n) \times \left(exp\left(-\alpha_p(t_p - x_p)\right) - exp\left(-(\alpha_p t_p + \alpha_n x_i)\right)\right) \tag{3.14}$$

$$\eta_p = \left[\frac{(1 - R_p)(1 - R_i)\alpha_p L_n}{(\alpha_p L_n)^2 - 1}\right] \times \left[(A - \alpha_p L_n)\left(exp\left(-\alpha_p(t_p - x_p)\right)\right) - (A - 1)\left(\frac{\alpha_p L_n - \gamma_n}{1 - \gamma_n}\right)\left(exp\left(\frac{d + x_p}{L_n}\right)\right)\right] \tag{3.15}$$

Where

$$A = \frac{\gamma_n \, cosh\left(\frac{t_p - x_p}{L_n}\right) + sinh\left(\frac{t_p - x_p}{L_n}\right)}{cosh\left(\frac{t_p - x_p}{L_n}\right) + \gamma_n \, sinh\left(\frac{t_p - x_p}{L_n}\right)} \tag{3.16}$$

$$\eta_n = \left[\frac{(1 - R_p)(1 - R_i)(1 - R_n)\alpha_n L_p}{(\alpha_n L_p)^2 - 1}\right] \times \left(\left(B + \alpha_n L_p\right)\left(exp\left(-(\alpha_p t_p + \alpha_n x_i)\right)\right) - (B + 1)\left(\frac{\alpha_n L_p + \gamma_p}{1 + \gamma_p}\right) \times \left(exp\left(-\alpha_n(d + t_p)\right)\right) \times \left(exp\left(\frac{d - x_i}{L_p}\right)\right)\right) \tag{3.17}$$

Where

$$B = \frac{\gamma_p \, cosh\left(\frac{d - x_i}{L_p}\right) + sinh\left(\frac{d - x_i}{L_p}\right)}{cosh\left(\frac{d - x_i}{L_p}\right) + \gamma_p \, sinh\left(\frac{d - x_i}{L_p}\right)} \tag{3.18}$$

where R_p, R_i and R_n are the Fresnel reflection coefficients at the various interfaces; α_p and α_n are the absorption coefficients of the *p*- and *n*-regions, respectively; t_p and d are the thicknesses of *p*- and *i*-regions, respectively; x_p and x_i are the depletion widths in *p*- and *i*-regions, respectively; L_n and L_p are the electron and hole diffusion lengths, respectively. The equations governing the diffusion length and Fresnel reflection coefficient are

$$L_n = \left(\frac{KT\mu_n\tau_n}{q}\right)^{\frac{1}{2}}, L_p = \left(\frac{KT\mu_p\tau_p}{q}\right)^{\frac{1}{2}} \quad (5.19)$$

$$R_{(x)} = \frac{(n_2 - n_1)^2}{(n_2 + n_1)^2} \quad (3.20)$$

where *x* can be *p, i,* or *n*; n_2 and n_1 are the refractive indices of the two media at the interface [30].

The ratio of photocurrent to incident optical power is called responsivity (R) of a UV PD, which is directly proportional to η, as given by [21, 24]

$$R = \frac{q\eta\lambda}{hc} \quad (6.21)$$

where c is the speed of light, h is Planck constant and λ is the incident light wavelength.

3.3. Experimental Data

Table 3.1: *Provides the Experimental Parameter Values of Layers Used for Modeling*

Parameter	SZO [31]	ZnO [32]	GZO [31]
Mobility (cm^2/V-s)	6.75	6.5	14.16
Carrier concentration (cm^{-3})	1.3×10^{17}	7.2×10^{18}	2.8×10^{19}

DIBS system is used for the deposition of SZO, ZnO and GZO layers. Details of the DIBS growth process are mentioned elsewhere [31-32].

Some of the electrical and optical parameters used in the simulation are obtained from our previous experimental work.

Table 3.1 provide the values of the experimental parameters for *p*-, *i*-, and *n*-regions grown by DIBS and used in the analytical modeling. Table 3.2 provides the values of the some other parameters used during the analysis [33]. Here in the Table 3.2, m_e is the mass of electron [34].

Table 3.2: *Provides Value of Some Other Parameters Used During Modeling*

Parameter	For holes	For electrons
Diffusion constant (cm^2/s)	0.1688	0.354
Surface recombination velocity (cm/s)	6×10^5	4×10^5
Diffusion length (cm)	1.299×10^{-5}	3.25×10^{-5}
Minority carrier lifetime (s)	1×10^{-9}	3×10^{-9}
Effective mass (Kg)	$0.318\, m_e$	$0.25\, m_e$

3.4. Results and Discussion

In order to validate the analytical model formulation, the computed results are matched with the experimental results obtained by Feng Sun et al [22], where they studied Li-N ZnO/*i*-ZnO/*n*-ZnO UV PD. In Figure 3.2, a comparison of computed and experimental results is shown for the variation of responsivity with wavelength at zero bias voltage and the dark current in the reverse bias. A close agreement is observed between the computed and experimental results and this validates the presented analytical model.

After validation, the analytical model is used to predict the performance of homojunction *p*-*i*-*n* UV PDs based on ZnO-material system. The responsivity variation with respect to the wavelength at zero bias voltage for the *p*-SZO/*i*-ZnO/*n*-GZO UV PD structure with varying thickness (t_p) of the topmost illuminated *p*-region while the thickness of the *i*- and

n-layer remain constant at 50 and 300 nm, respectively, is shown in Figure 3.3.

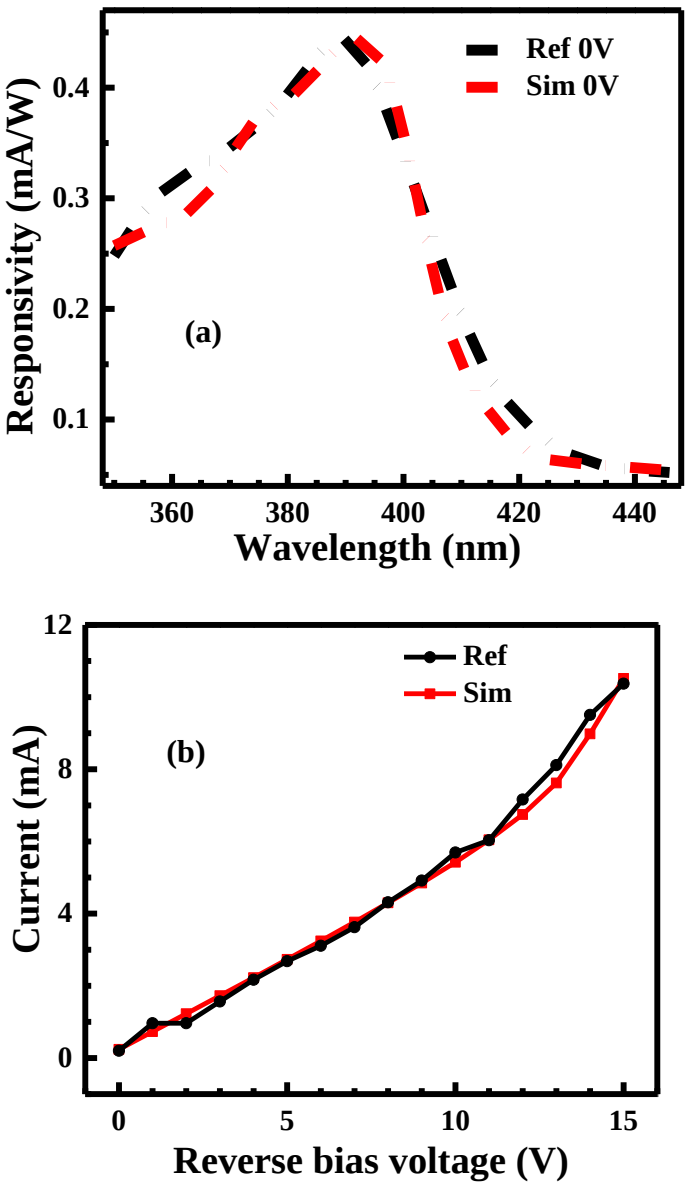

Figure 3.2 *Graphical Comparison of the Simulated and Experimental results for (a) Spectral Responsivity and (b) Dark Current Variation with Reverse Bias Voltage.*

The inset in Figure 3.3 indicates that the peak responsivity of the *p*-SZO/*i*-ZnO/*n*-GZO UV PD structure at zero bias is at 362 nm which is due to the high bandgap about 3.37 eV in ZnO and doped ZnO family. The peak responsivity value, with the *p*-layer thickness of 50 nm, in SZO/ZnO/GZO UV PD, is found to be ~5.3 mA/W at 362 nm.

In the UV PDs, it is observed that the peak responsivity appears around the band edge. An increase in the responsivity peaks in the device is also observed with a reduction in the thickness (t_p) of *p*-layer from 200 to 50 nm.

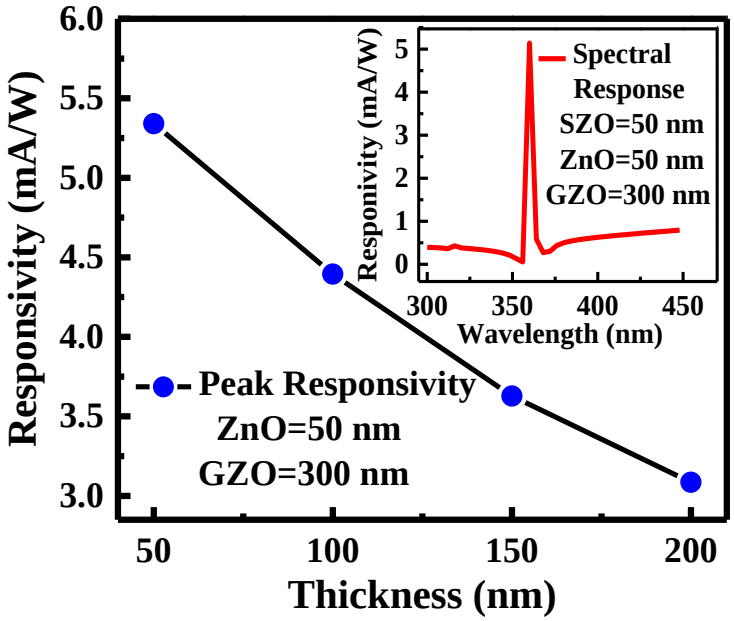

Figure 3.3 *Peak Responsivity Variation for SZO/ZnO/GZO UV PD with Different SZO (p-layer) Thickness (t_p). Inset shows the Spectral Response Curve for p-i-n UV PD at Zero Bias.*

Thus, a thinner acceptor-doped ZnO layer allows a greater number of the photons to reach the depletion region, due to which large number of charge carriers is photogenerated in the region [35-36]. The equation governing the charge carrier photogeneration with distance from the surface is given by $N(D) = Ne^{-\alpha D}$, where N(D) is the number of photons at a distance of D from material surface and α is the absorption coefficient of material as function of wavelength [37]. Therefore, a thinner *p*-layer results in higher responsivity in all wavelengths shorter than the wavelength corresponding to the bandgap of the illuminated material (for higher wavelength, the material become transparent as shown in the inset of Figure 3.3) for the homojunction UV PDs [36]. The peak responsivity reduces to ~3.08 mA/W at zero bias for 200 nm of *p*-layer thickness.

The variation in the responsivity with respect to wavelength at 0 V bias is shown in Figure 3.4. The thickness (d) of the sandwiched *i*-region is varied from 20 to 80 nm for the *p*-SZO/*i*-ZnO/*n*-GZO UV PD structure when the thicknesses of the SZO and GZO layers are kept constant at 50 and 300 nm, respectively.

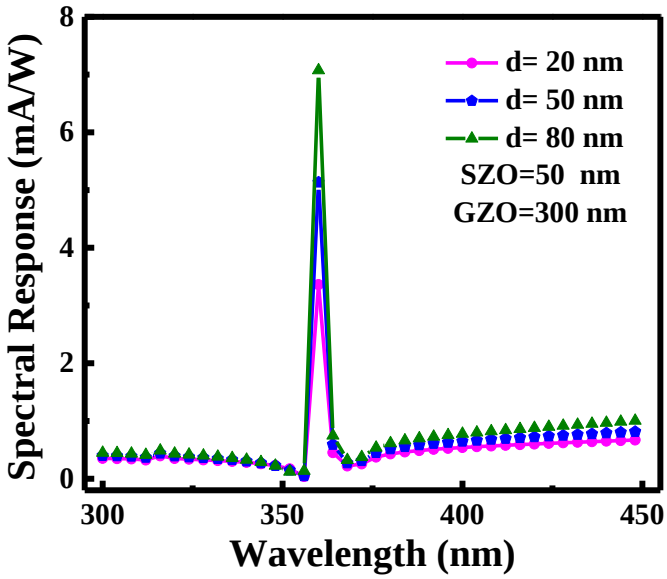

Figure 3.4 *Spectral Responsivity Curve for p-i-n UV PD with Different i-ZnO Thickness.*

As seen in Figure 3.4, the peak responsivity changes from 3.5 to 7.3 mA/W as the thickness (d) of ZnO layer changes from 20 to 80 nm.

The device responsivity increases as the absorber layer thickness increases. This observation can be drawn from the fact that when UV illumination falls on top of *p*-*i*-*n* homojunction detector, the corresponding photons are absorbed in the depletion region in the vicinity of the SZO/ ZnO interface, and the hole-electron pairs are photogenerated [38]. Due to the internal electric field in ZnO layer, there is the formation of spatial separation between the photogenerated carriers, and the number of hole-electron pair recombinations may decrease. As a result, the photogenerated electrons drift into the *n*-GZO, whereas the photogenerated holes are accelerated into *p*-SZO by the depletion electric field in ZnO layer. A larger depletion region results in higher photogeneration of the minority carriers, which, in turn, increases

the gain, photocurrent, efficiency as well as the responsivity of the device [35]. Therefore, a thick absorber region is required to achieve large value of quantum efficiency. The depletion region thickness at the SZO/ZnO interface can be estimated by equations 22 and 23 [39-40]:

$$x_p + x_i = \sqrt{\frac{2\varepsilon_s(N_a + N_i)\varphi_{bi}}{qN_aN_i}} \tag{3.22}$$

$$x_pN_a = x_iN_i \tag{7.23}$$

where x_p is the width of the depletion region in SZO and x_i is that in *i*-ZnO layer, q is the charge of electron, N_a is the concentration of SZO layer, N_i is the carrier concentration of *i*-ZnO, φ_{bi} is the interface barrier potential and ε_s is the dielectric constant of ZnO.

The peak responsivity change with corresponding change in applied reverse bias across the *p-i-n* homojunction device is presented in Figure 3.5. With the increment in the reverse bias voltage, the responsivity of the device increases correspondingly.

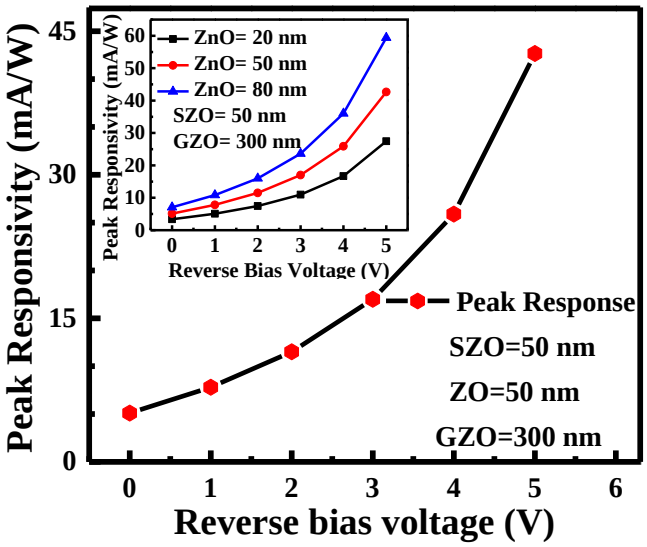

Figure 3.5 *Variation of Peak Responsivity for SZO/ZnO/GZO UV PDs with Reverse Bias. Inset shows variation of peak responsivity for different thickness of ZnO.*

The observation validates the fact that a wider depletion region is obtained with a larger reverse bias, which in turn results in the generation of larger number of photogenerated charge carriers in the

depletion region before being swept away by the built-in electric potential [40-41]. A similar trend of increment in the responsivity with applied reverse bias was observed by Lin *et al* [16].

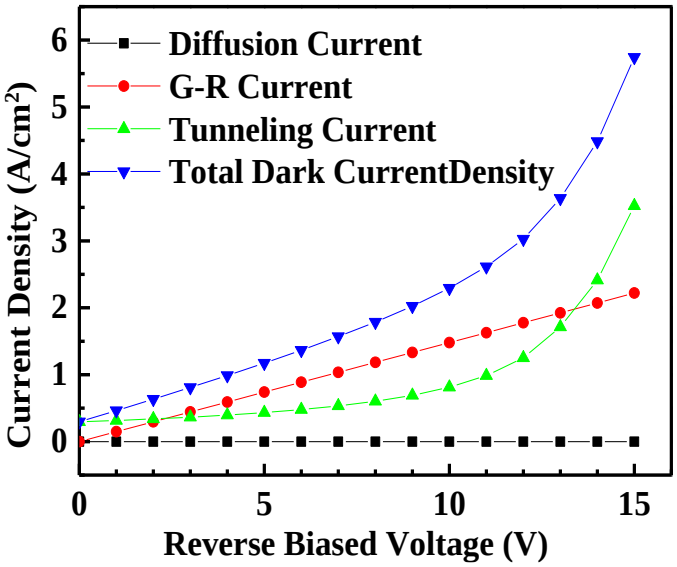

Figure 3.6 *Dark Current Variation for SZO/ZnO/GZO UV PDs with Reverse Bias.*

The dark current variation in SZO/ZnO/GZO *p-i-n* UV PD with applied reverse bias voltage is shown in Figure 3.6. In the figure it is clearly shown that the dark current of the *p-i-n* UV homojunction photodetector increases with the increase in the reverse bias voltage. This trend suggests that the major current component contributing to this kind of behavior is tunneling current [42-43]. The dark current increment with the applied reverse bias voltage increment is also consistent with that in other UV photodetector structures reported in the literature earlier [5, 44-45].

Table 3.3 shows the comparison of responsivity and the dark current of experimentally reported [22] with the simulated results presented in this work for a similar *p-i-n* UV photodetector structure. From the data presented in Table 3.3, it is evident that the DIBS-grown *p*-SZO influences the performance parameter of the UV photodetector with an improvement in peak responsivity and dark current making the structure superior over the *p-i-n* UV photodetectors earlier reported for the same material system.

Table 3.3: *Comparision of Performance Parameter of the Present Work with the Literature*

Parameter	Thickness of layers (nm)	Peak responsivity (mA/W) at 0 V bias	Dark current (mA) at -15 V
SZO/ZnO/GZO (This work)	150/50/300	3.63	-5.8
Li-N ZnO/*i*-ZnO/*n*-ZnO [22]	150/50/300	0.45	-12

3.5. Conclusion

In comparision to the reported results of Li-N ZnO/*i*-ZnO/*n*-ZnO UV PD, the analytically predicted DIBS-grown SZO/ZnO/GZO *p*-*i*-*n* UV PD provides with better performance parameters in terms of peak responsivity and dark current. With the increase in *p*-SZO layer thickness from 50 to 200 nm, responsivity of the UV PD decreases from 5.34 to 3.09 mA/W. Also, with the rise in *i*-ZnO layer thickness from 20 to 80 nm, the responsivity shows an increase of 108.6%. In comparison to already existing ZnO-based UV *p*-*i*-*n* PD, the DIBS-grown *p*-*i*-*n* PD with SZO as acceptor-doped ZnO has shown an improvement of ~7.6-fold and reduction of ~2.1-fold in the peak responsivity at 0 V and dark current at -15 V, respectively, at room temperature. The obtained results are crucial in predicting the improvement and optimization of the existing ZnO-based *p*-*i*-*n* UV PD performance parameters, which lead to the development of efficient and cost-effective UV PDs.

3.6. References

[1] H. Wang, G. Yi, X. Zu, X. Jiang, Z. Zhang, and H. Luo, "A highly sensitive and self-powered ultraviolet photodetector composed of titanium dioxide nanorods and polyaniline nanowires," Material Letter, 138, 204-207, 2015.

[2] M. Kumar, Y. Noh, K. Polat, A.K. Okyay, and D. Lee, "Metal–semiconductor–metal UV photodetector based on Ga doped ZnO/graphene interface," Solid State Communications, 224, 37-40,

2015.

[3] W. Dai, X. Pan, S. Chen, C. Chen, W. Chen, H. Zhang, and Z. Ye, “ZnO homojunction UV photodetector based on solution-grown Sb-doped *p*-type ZnO nanorods and pure *n*-type ZnO nanorods,” RSC Advances, 5, 6311, 2015.

[4] J.H. Yu, D.S. Park, J.H. Kim, T.S. Jeong, C.J. Youn , and K.J. Hong, “Post-growth annealing and wide bandgap modulation of BeZnO layers grown by RF co-sputtering of ZnO and Be targets,” Journal of Material Science, 45, 130–135, 2010.

[5] R. Bhardwaj, P. Sharma, R. Singh, M. Gupta, and S. Mukherjee, “High responsivity $Mg_xZn_{1-x}O$ based ultraviolet photodetector fabricated by dual ion beam sputtering,” IEEE Sensors Journal, 18, 7, 2018.

[6] W. Ouyang, J. Chen, J.H. He, and X. Fang, “Improved Photoelectric Performance of UV Photodetector Based on ZnO Nanoparticle Decorated BiOCl Nanosheet Arrays onto PDMS Substrate: The heterojunction and Ti_3C_2Tx MXene Conduction Layer,” Advanced Electronic Materials, 6, 2000168, 2020.

[7] B.J. Kwon, H.S. Kwack, S.K. Lee, Y.H. Cho, D.K. Hwang, and S.J. Park, “Optical investigation of *p*-type ZnO epilayers doped with different phosphorus concentrations by radio-frequency magnetron sputtering,” Applied Physics Letters, 91, 061903, 2007.

[8] B. Zhao, F. Wang, H. Chen, L. Zheng, L. Su, D. Zhao, and X. Fang, “An ultrahigh responsivity (9.7 mA W^{-1}) self-powered solar-blind photodetector based on individual ZnO–Ga_2O_3 heterostructures,” Advanced Functional Materials, 27, 1700264, 2017.

[9] K. Hu, F. Teng, L. Zheng, P. Yu, Z. Zhang, H. Chen, and X. Fang, “Binary response Se/ZnO *p*-*n* heterojunction UV photodetector with high on/off ratio and fast speed,” Laser & Photonics Review, 11, 1600257, 2017.

[10] L. Hu, J. Yan, M. Liao, H. Xiang, X. Gong, L. Zhang, and X. Fang, “An optimized ultraviolet-A light photodetector with wide range photoresponse based on ZnS/ZnO biaxial nanobelt,” Advanced

Materials, 24, 2305-2309, 2012.

[11] H. Ferhati, F. Djeffal, A.E. Benhaya, and A. Bendjerad, “Giant detectivity of ZnO-based self-powered UV photodetector by inserting an engineered back gold layer using RF sputtering,” IEEE Sensors Journal, 20, 3512-3519, 2020.

[12] Y. Ning, Z. Zhang, F.Teng, and X. Fang, “Novel transparent and self-Powered UV Photodetector based on crossed ZnO nanofiber array homojunction,” Small, 14, 1703754, 2018.

[13] H. Ferhatia, and F. Djeffal, “New high-performance ultraviolet (MSM) TiO_2/glass photodetector based on diffraction grating for optoelectronic applications,” Optik, 127, 7202–7209, 2016.

[14] R. Bhardwaj, P. Sharma, R. Singh, and S. Mukherjee, “Sb-doped *p*-MgZnO/*n*-Si heterojunction UV photodetector fabricated by dual ion beam sputtering,” IEEE Photonics Technology Letters, 29, 14, 2017.

[15] L.J. Mandalapu, Z. Yang, F.X. Xiu, D.T. Zhao, and J.L. Liua, “Homojunction photodiodes based on Sb-doped *p*-type ZnO for ultraviolet detection,” Applied Physics Letters, 88, 092103, 2006.

[16] T.S. Lin, and C.T. Lee, “Performance investigation of *p*-*i*-*n* ZnO-based thin film homojunction ultraviolet photodetectors,” Applied Physics Letters, 101, 221118, 2012.

[17] W.C. Qiu, W.D. Hu, L. Chen, C. Lin, X.A. Cheng, X.S. Chen, and W. Lu, “Dark current transport and avalanche mechanism in HgCdTe electron-avalanche photodiodes,” IEEE Transactions on Electron Devices, 62, 6, 2015.

[18] D.J.H. Lambert, M.M. Wong, U. Chowdhury, C. Collins, T. Li, H.K. Kwon, B.S. Shelton, T.G. Zhu, J.C. Campbell, and R.D. Dupuis, “Back illuminated AlGaN solar-blind photodetectors,” Applied Physics Letters, 77, 1900, 2000.

[19] J.R. Duclèrea, M. Novotny, A. Meaney, R. O’Haire, E. McGlynn, M.O. Henry, and J.P. Mosnier, “Properties of Li-, P- and N-doped ZnO thin films prepared by pulsed laser deposition,” Superlattices and Microstructures, 38, 397–405, 2005.

[20] D.C. Look, and B. Claflin, "*p*-type doping and devices based on ZnO," Physica Status Solidi (b), 241, 624–630, 2004.

[21] S.K. Pandey, S.K. Pandey, V. Awasthi, A. Kumar, U.P. Deshpande, M. Gupta, and S. Mukherjee, "*p*-type conduction from Sb-doped ZnO thin films grown by dual ion beam sputtering in the absence of oxygen ambient," Journal of Applied Physics, 114, 163107, 2013.

[22] F. Sun, C.X. Shana, S.P. Wang, B.H. Li, Z.Z. Zhang, C.L. Yang, and D.Z. Shen, "Ultraviolet photodetectors fabricated from ZnO *p*–*i*–*n* homojunction structures," Materials Chemistry and Physics, vol. 129, pp. 27– 29, 2011.

[23] B.L. Sharma, and R.K. Purohit, "Semiconductor Heterojunction," New York: Pergamon, 1974.

[24] A.D.D. Dwivedi, A. Mittal, A. Agrawal, and P. Chakrabarti, "Analytical modeling and ATLAS simulation of N^{+}-InP/n_0-$In_{0.53}Ga_{0.47}As$/p^{+}-$In_{0.53}Ga_{0.47}As$ *p*-*i*-*n* photodetector for optical fiber communication," Infrared Physics & Technology, 53, 236–245, 2010.

[25] P. Chakrabarti, A. Krier, and A.F. Morgan, "Analysis and simulation of a mid-infrared P^{+}-$InAs_{0.55}Sb_{0.15}P_{0.30}$/$n_0$-$InAs_{0.55}Sb_{0.11}$/$N^{+}$-$InAs_{0.55}Sb_{0.15}P_{0.30}$ double heterojunction photodetector grown by LPE," IEEE Transactions on Electron Devices, 50, 2049–2058, 2003.

[26] G.J. Nott, P.C. Findlay, J.G. Crowder, C.R. Pidgeon, C.T. Elliot, T. Ashley, A.D. Johnson, J.P.R. Wells, I.V. Bradley, B.N. Murdin, and A.M. White, "Direct determination of Shockley-Read-Hall trap density in InSb/InAlSb detectors," Journal of Physics: Condense Matter, 12, L731–L734, 2000.

[27] V. Gopal, S.K. Singh, and R.M. Mehra, "Analysis of dark current contributions in mercury cadmium telluride junction diodes," Infrared Physics and Technology, 43, 317–326, 2002.

[28] R.Q. Yang, M. Sweeny, D. Day, and X.M. Xu, "Interband tunneling in heterojunction tunnel diodes," IEEE Transaction of Electron. Devices, 38, 442–446, 1991.

[29] W. Mtangi, F.D. Auret, C. Nyamhere, P.J.J.v. Rensburg, M. Diale, and A. Chawanda, "Analysis of temperature-dependent I-V measurements on Pd/ZnO Schottky barrier diodes and the determination of the Richardson constant," Physica B, 404, 1092–1096, 2009.

[30] P. Bhattacharya, "Semiconductor Optoelectronic Devices," Prentice, Hall of India Private Limited, New Delhi, 1995.

[31] S.K. Pandey, V. Awasthi, S. Verma, and S. Mukherjee, "Blue electroluminescence from Sb-ZnO/Cd-ZnO/Ga-ZnO heterojunction diode fabricated by dual ion beam sputtering," Optics Express, 22, 25, 30983-30991, 2014.

[32] S.K. Pandey, S.K. Pandey, V. Awasthi, A. Kumar, U.P. Deshpande, M. Gupta, and S. Mukherjee, "Influence of annealing temperature on ZnO thin films grown by dual ion beam sputtering," Bulletin of Materials Science, 37, 1-7, 2014.

[33] R. Bhardwaj, R. Singh, M.A. Khan, and S. Mukherjee, "Performance analysis of *p*-LPZO/*n*-GZO and *p*-SZO/*n*-GZO homojunction UV photodetectors," Superlattices and Microstructures, 140, 1-7, 2020.

[34] N.N. Syrbu, I.M. Tiginyanu, V.V. Zalamai, V.V. Ursaki, and E.V. Rusu, "Exciton polariton spectra and carrier effective masses in ZnO single crystals," Physica B, 353, 111–115, 2004.

[35] C.K.Wang, T.K. Ko, C.S. Chang, S.J. Chang, Y.K. Su, T.C. Wen, C.H. Chiou, and Y.Z. Chiou, "The Thickness Effect of *p*-AlGaN Blocking Layer in UV-A Bandpass Photodetectors," IEEE Photonics Technology Letters, 17, 2161, 2005.

[36] Y.Z. Chiou, "Nitride-Based *p*-*i*-*n* Bandpass Photodetector," IEEE Electron Devices Letters, 26, 172, 2005.

[37] S.Y. Bae, J.P. Shim, D.S. Lee, S.R. Jeon, and G. Namkoong, "Improved photovoltaic effects of a vertical-type InGaN/GaN multiple quantum well solar cell," Japanese Journal of Applied Physics, 50, 092301, 2011.

[38] G.Y. Xu, A. Salvador, W. Kim, Z. Fan, C. Lu, and H. Tang, "High

speed, low noise ultraviolet photodetectors based on GaN *p*-*i*-*n* and AlGaN(*p*)-GaN(*i*)-GaN(*n*)structures," Applied Physics Letters, 71, 2154-2156, 1997.

[39] H. Shen, C.X. Shan, B.H. Li, B. Xuan, and D.Z. Shen, "Reliable self-powered highly spectrum-selective ZnO ultraviolet photodetectors," Applied Physics Letters, 103, 232112, 2013.

[40] S.N. Das, and A.K. Pal, "Properties of a nanocrystalline GaN *p*–*n* homojunction prepared by a high-pressure sputtering technique," Semiconductor Science and Technology, 21, 1557-1562, 2006.

[41] K. Vanheusden, C.H. Seager, W.L. Warren, D.R. Tallant, and J.A. Voigt, "Correlation between photoluminescence and oxygen vacancies in ZnO phosphors," Applied Physics Letters, 68, 403-405, 1996.

[42] P. Martyniuk, and A. Rogalski, "Theoretical modeling of InAsSb/AlAsSb barrier detectors for higher-operation-temperature conditions," Optical Engineering, 53, 017106, 2014.

[43] P. Chakrabarti, P. K. Saxena, and R.K. Lal, "Analytical Simulation of an InAsSb Photovoltaic Detector for Mid-Infrared Applications," International Journal of Infrared and Millimeter Waves, 27, 1119-1132, 2006.

[44] F. Klem, J.K. Kim , M.J. Cich , S.D. Hawkins , T.R. Fortune , and J.L. Rienstra, "Comparison of nBn and nBp mid-wave barrier infrared photodetectors," Quantum sensing and Nanophotonic Devices VII, 7608, 1-12, 2010.

[45] Y. Vygranenko, K. Wang, and A. Nathan, "Low leakage *p*-NiO⁄*i*-ZnO⁄*n*-ITO heterostructure ultraviolet sensor," Applied Phyics Letters, 89, 172105, 2006.

[46] S. W. Feng, C. M. Lai, C. H. Chen, W. C. Sun, and L. W. Tu, "Theoretical simulations of the effects of the indium content, thickness, and defect density of the *i*-layer on the performance of *p*-*i*-*n* InGaN single homojunction solar cells," Journal of Applied Physics, 108, 9, 093118, 2010.

Chapter 4

High Detectivity and Fast MoS_2 Monolayer MSM Photodetector

4.1. Introduction

In the last decade, two-dimensional (2D) materials, specifically transition metal dichalcogenides (TMDs), have gained remarkable interest due to many interesting electrical and optoelectrical properties, such as chemical composition and structural configuration dependent conductivity, low-power requirement, ultra-small size, and many more; which opens the door for multiple research platform including photodetection and optoelectronics [1-3]. These extraordinary properties encourage the development of many 2D material such as molybdenum disulfide (MoS_2), tungsten disulphide (WS_2), molybdenum diselenide ($MoSe_2$), tungsten diselenide (WSe_2), borophene (2D boron), hexagonal boron nitride (h-BN), silicene (2D silicon), MXenes (2D carbides/nitrides), and germanene (2D germanium) that are capable of formation of atomic sheets [2-5]. One of the highly studied layered TMDs for electronics, optoelectronics, photovoltaics, and photocatalytic applications is S-Mo-S covalently bonded MoS_2. The exceptional properties of MoS_2 monolayer include direct energy bandgap (1.8 eV) at room temperature, substantial mobility (~700 $cm^2/V.s$), significant optical absorption for visible spectrum of light, a high current on/off ratio, and a massive photoluminescence peak [1,6-8].

Various methods of MoS_2 monolayer deposition, are investigated, however, are restricted in obtaining controlled and homogeneous film growth. One of the most simple and efficient techniques of synthesizing MoS2 monolayer is chemical vapor deposition (CVD) due to its feature of wide tunability in growth parameters and substrates [9-10]. Photodetection is one of the promising optoelectronic applications of

MoS_2 layered TMD because of its low dark current due variation of TMD layer property with field effect modulation [11-12]. The dominant structures for MoS_2 detectors are transistor and metal-semiconductor-metal (MSM) based architectures. In MSM detector, TMD layer used as semiconducting material paired with a vast variety of metals. MSM structure provides the freedom of physical positioning and fabrication layout of contact, making the device more robust. Moreover, autonomy of contact metal and device structure provides wide disparity in different figures of merit of photodetector [13]. MoS_2 monolayer MSM photodetector are widely studied for dark- and photocurrent, responsivity and external quantum efficiency measurements in the literature [14-15]. However, various photodetecting performance parameters, like detectivity, noise equivalent power (NEP), and variation of these parameters with external bias voltage are not adequately investigated. This leads to the unexplored capability of MoS_2 monolayer MSM photodetector, due to lack of studies covering the detailed investigation of CVD-grown MoS_2 monolayer based devices.

In this work, I have fabricated MoS_2 monolayer MSM photodetector in which the fabrication process starts with lithographical designing of interdigitated metallic contacts over glass substrate followed by wet transfer of CVD-grown MoS_2 monolayer on top. Platinum (Pt) based interdigital electrode structure is used to investigate the performance of the CVD-grown MoS_2 monolayer. In addition, surface energy assisted wet transfer process is employed for transferring the MoS_2 monolayer from Si/SiO_2 onto the glass substrate containing interdigital electrodes (IDEs). Subsequently, the relevant performance parameters in the form of dark- and photo-current, responsivity, quantum efficiency, detectivity and NEP are evaluated for MoS_2 MSM detector. Furthermore, the variation of responsivity, quantum efficiency, detectivity and NEP with bias voltage is examined. This study exhibits a detailed investigation of CVD-grown MoS_2 monolayer MSM photodetecting application.

4.2. Experimental Details

4.2.1 Deposition of MoS_2

The SiO_2/Si substrate with a SiO_2 thickness of 300 nm on Si(001) substrate (resistivity ~5-100 Ω-cm) is initially sonicated for 10 min in acetone and isopropyl alcohol each, then rinsed with deionized water and finally purged with dry nitrogen gas of 5N-purity before deposition. To prepare MoO_3 solution, 10 mL NH_4OH is mixed with 200 mg of MoO_3 powder and 50 mg of NaCl; and this mixture is magnetically stirred till the solution becomes completely transparent. From 0.5 µL (20 mg/ml) of this solution, a seed layer of MoO_3 is deposited via spin coating at 3500 rpm over the substrate and followed by preheating of the substrate. Subsequently, in the CVD furnace, 600 mg of sulphur powder is placed in an alumina boat in the direction of carrier gas, while, in another alumina boat, the preheated MoO_3 deposited substrate is placed, as shown in Figure 4.1. During the deposition, a deposition temperature 800 ^oC, a constant flow rate of Ar at 150 sccm and O_2 at 2 sccm for 10 min of deposition time are maintained. The flowchart of the complete process of MoS_2 deposition using the CVD furnace is shown in figure 4.1.

4.2.2 Wet Transfer Process

The flowchart of Figure 4.1(b) includes all the major steps of the MoS_2 transfer process. Initially, a 9 g polystyrene is dissolved in 100 ml of toluene solution and continuously magnetically stirred, till the solution becomes completely transparent without any precipitate. 1.2 mL of this solution is then spin-coated over the MoS_2/SiO_2/Si sample at 3500 rpm. The sample is then heated for 30 min at 85 ^oC in hot air oven for increasing the adhesion of spin coated film with the deposited MoS_2 monolayer. The sample is then slightly etched from the sides to remove the spin-coated film of polystyrene solution from the sample and to provide a way for penetration of deionized water between the MoS_2 monolayer and SiO_2/Si substrate. The sample is then carefully dipped

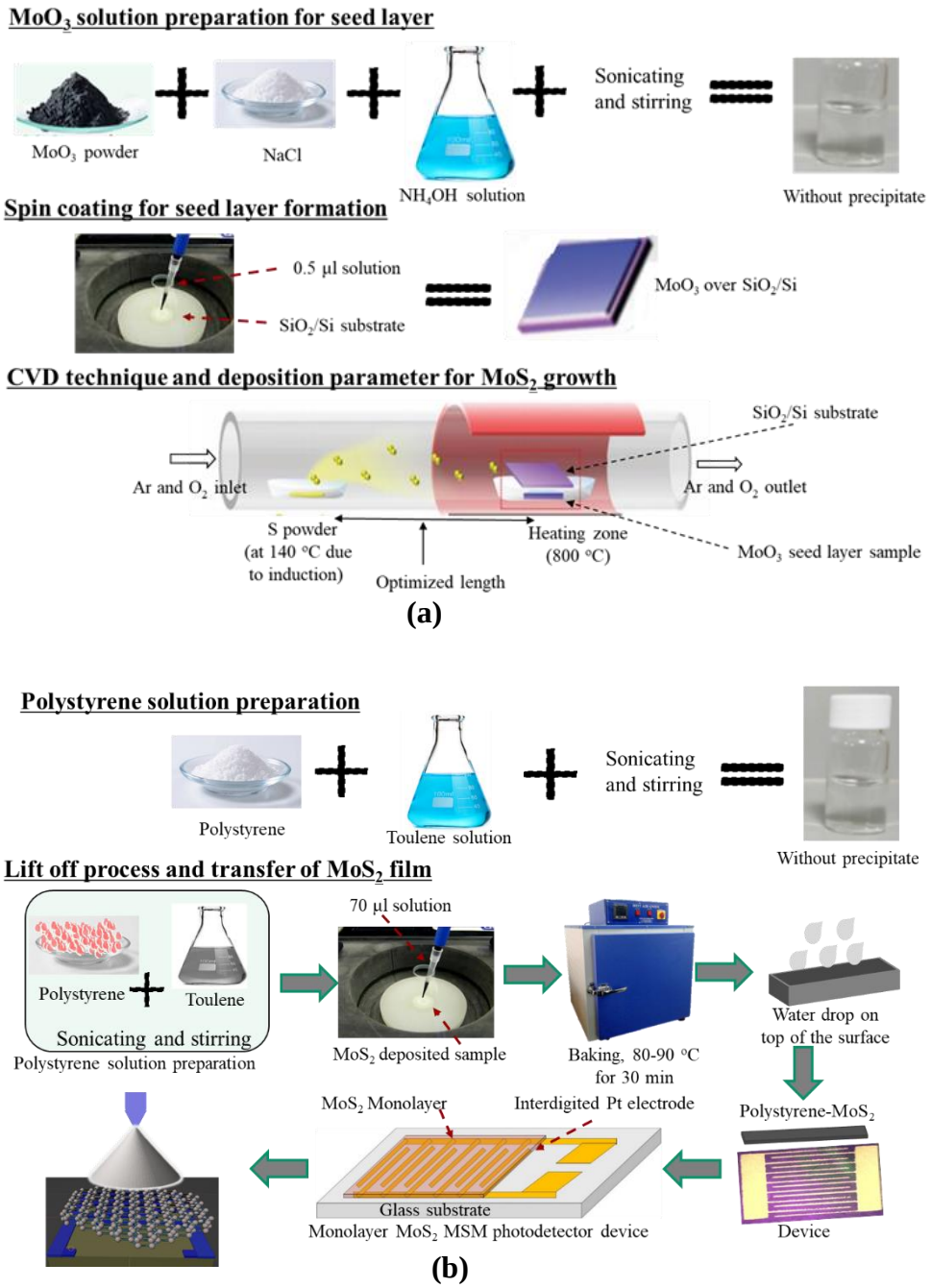

Figure 4.1 *(a) Schematic of the Complete Deposition Process of MoS_2 Monolayer and (b) Wet Transfer Process on Interdigitated Pt Electrode.*

into the deionized water from the etched corner. Due to the hydrophilic nature of MoS_2, after deionized water penetration, the MoS_2 monolayer can be easily peeled off from the SiO_2/Si substrate with the spin-coated film of polystyrene-toluene. After this, the lifted-off MoS_2 monolayer is

placed on the glass substrate with IDEs. The fabricated device is then mildly heated for 1-2 min at 50 ^{o}C on hot plate for enhancing the adhesion between the placed MoS_2 monolayer with the electrodes. The residues of the polystyrene-toluene film on the device is removed by rinsing and dipping of the device in toluene solution [16]. The outcome of this process is MSM photodetector, as systematically illustrated in Figure 4.1 (b). Figure 4.2 (a) and (b) depict the normal camera image and microscopically measured electrode dimension of the MSM

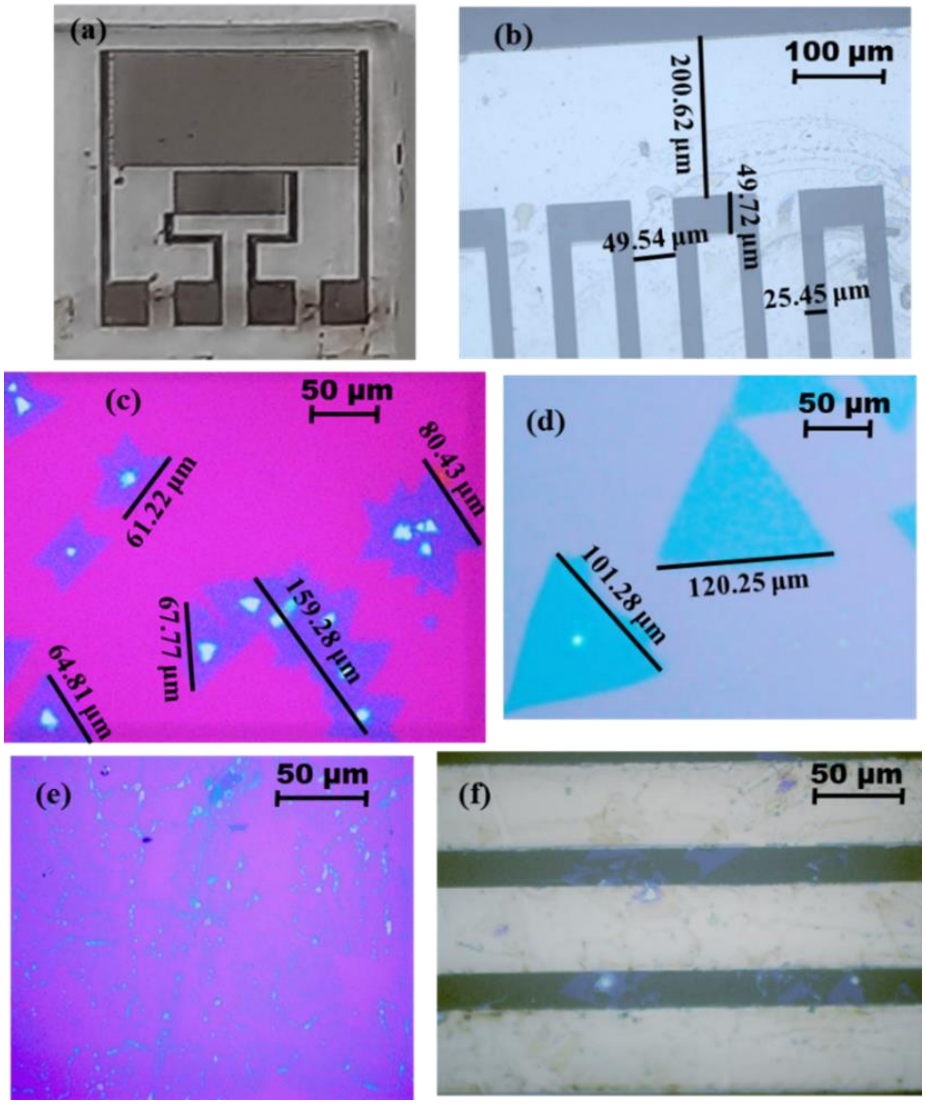

Figure 4.2 *(a) Camera Image of PD, and (b) Electrode Dimensions. Optical image of (c) Deposited MoS_2, (d) Maximum Dimensions, (e) SiO_2/Si Substrate after Wet Transfer Process, and (f) Transferred MoS_2 Monolayer on IDEs.*

device, respectively. The interelectrode spacing of 25 μm, electrode thickness of 50 μm, electrode (connected to contact pad) thickness of 200 μm, and the active device area of 12.625 mm^2 are measured.

4.2.3 Details of Measuring Instruments

For verifying the proper deposition and wet transfer of the MoS_2 monolayer, a Carl Zeiss Axio Vert.A1 inverted microscope is used for imaging. A spectroscopic ellipsometry (SE, M-2000D from J. A. Woollam Co., Inc) instrument is used for obtaining the optical parameters of the MoS_2 monolayer. A solar simulator (Photo Emission Tech Inc.) under standard conditions (AM 1.5 and 10000 mW cm^{-2}) is used under dark mode for measuring temperature dependent current-voltage (I-V) and under light mode for obtaining photovoltaic characteristics of the device. A Bentham PV-300 photovoltaic characterization system is used for measuring spectral photoresponse, quantum efficiency and photo switching characteristics (when interfaced with DMM6500 digital multimeter from Keithley and sourcemeter) [17]. I-V measurements at different wavelength is carried out by interfacing a PV-300 system with Keithley 2612A sourcemeter at room temperature. A Horiba LabRam HR Evolution spectrometer fitted with liquid nitrogen cooled Charge Coupled Device (CCD) detector is used for Raman spectroscopy measurement of the deposited MoS_2 monolayer.

Figure 4.2 (c) shows the constant contrast of the deposited MoS_2 in optical image, suggesting that a distributed single crystal of MoS_2 monolayer of perfect triangular shape having an average side length of ~45 μm is obtained while the maximum side length obtained is 120 μm, as shown in Figure 4.2 (d). Figure 4.2 (e) is the optical image of the sample after wet transfer process, revealing the residue of the deionized water and polystyrene toluene film, confirming the complete lifting-off of MoS_2. Figure 4.2 (f) shows the successfully transferred MoS_2 monolayer over the interdigitated Pt electrode confirming the fabrication

of the MSM photodetector device [7-10]. The positive difference in the work function at the junction of Pt and MoS_2 due to *n*-type nature of MoS_2, emphasize on the Schottky nature of the contact between them.

4.3. Results and Discussion

Before the wet transfer process, Raman spectroscopy and spectroscopic ellipsometry analysis of the MoS_2 monolayer are performed. Figure 4.3 presents two Raman peaks at 383.92 and 404.40 cm^{-1}, attributed to the in-plane (E^1_{2g}) and out-of-plane (A^1_g) vibrations, respectively. The energy difference (Δk) between these two peaks is 20.48 cm^{-1}, which strongly validates the formation of MoS_2 monolayer [7,10]. In spectroscopic ellipsometry analysis, the MoS_2 monolayer is analysed by a four-layer optical model, as earlier used by Yim *et al*, and the obtained thickness values of MoS_2 and SiO_2 layers are 0.70 and 309.68 nm, respectively, with an mean square error (MSE) of 7.738 [18]. The calculated bandgap of the MoS_2 monolayer via Tauc plot is 1.82 eV, which corresponds to the bandgap of MoS_2 monolayer. The results of Raman spectroscopy and ellipsometry confirm the growth of MoS_2 monolayer [18].

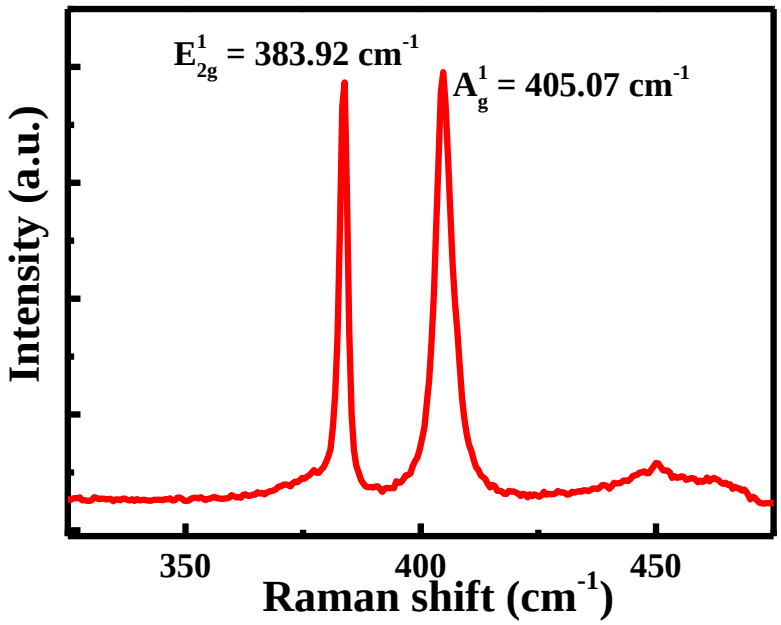

Figure 4.3 *Raman Spectrum of MoS_2 Monolayer.*

Figure 4.4 depicts the temperature-dependent I-V curves of the device performed using solar simulator in dark condition. The plot suggests that, as the temperature across the MSM device increases, the dark current increases [15,19]. The reverse saturation current, as well as current of any semiconducting device, is a temperature-dependent quantity and it increases with temperature due to the energy bandgap variation[20]. Researchers have discussed the potential of MoS_2 for photovoltaic application [1,6-7]. In the inset of Figure 4.4, inset (a) shows the temperature dependent I-V in linear scale and (b) depicts dark current variation with temperature at fixed bias, the plots confirms the increase in the value of dark current due to thermal excitation with rise in temperature.

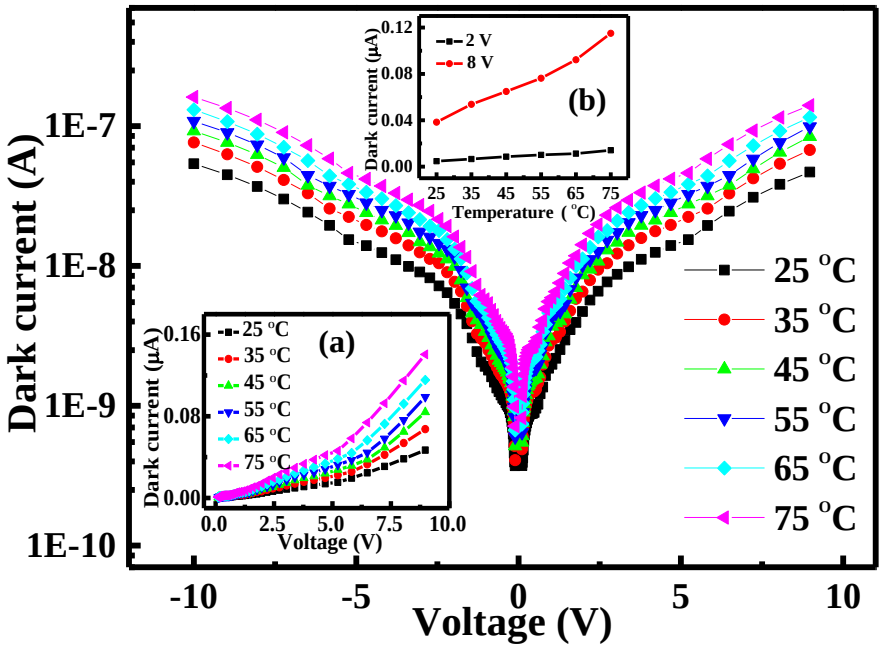

Figure 4.4 *Dark Current vs Voltage with Varying Temperature, the inset shows the (a) Plot in Linear Scale and (b) Dark Current with Temperature at Fixed Bias.*

In Figure 4.5, the I-V characteristics of the device are measured in light and dark modes for inspecting its properties for photovoltaic application under one sun illumination condition, and the obtained values of short circuit current and open circuit voltage are 6.72 μA and 0.87 V,

respectively [21-22]. The graph confirms the high potential of MoS_2 for photovoltaic applications.

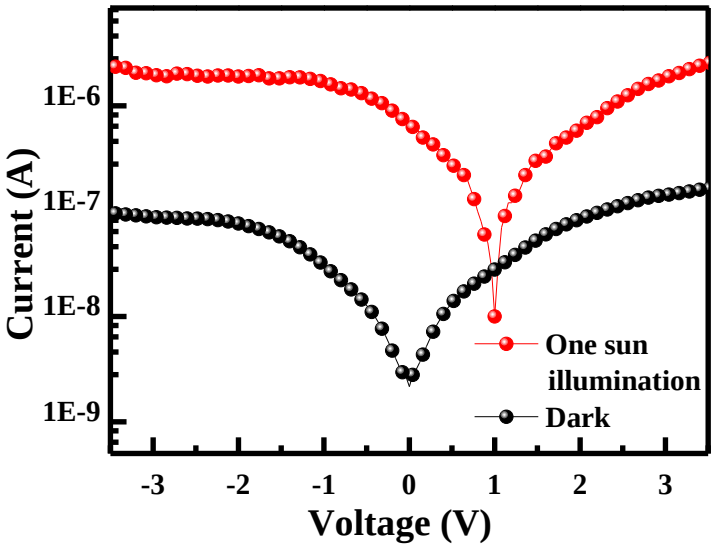

Figure 4.5 *I-V Plot of MoS_2 Monolayer for Photovoltaic Application under One Sun Illumination Condition.*

For different wavelength illumination, the variation of generated photocurrent with voltage at room temperature is analysed using a Bentham PV 300 system interfaced with Keithley 2612A system, as shown in Figure 4.6. The observed variation of photocurrent with wavelength can be understood by the fact that the intensity of the incident light is inversely proportional to the wavelength, if the illuminated area of the device is kept constant, resulting in a reduction in the photocurrent with the wavelength increase. An alternative explanation for this increase in photocurrent with decrease in wavelength is given by Han *et al.* which states that the increase in the energy of incident photons and interface chemistry between the 2D semiconductor and 3D metal activate more number of trap states in MoS_2 (formed due to existing defects) [23]. These trap states act as trap centres for photogenerated carriers, causing a delay in the carrier transportation to electrodes. Thus, the gain in the photocurrent with reduction in the wavelength is attributed to the trap states and defects [23-24]. Also, for MoS_2 monolayer, the energy owned by the incident

photon to excite an electron from valence to conduction band must be greater than the energy bandgap i.e. 1.8 eV, and the corresponding wavelength is ~681 nm [14,25]. This confirms the low value of photocurrent for the 750 nm incident wavelength, as observed in Figure 4.6. The inset of the Figure 4.6 shows the variation of photocurrent with wavelength, the image depicts that the MSM device has a high value of photocurrent for visible wavelengths compare to 750 nm.

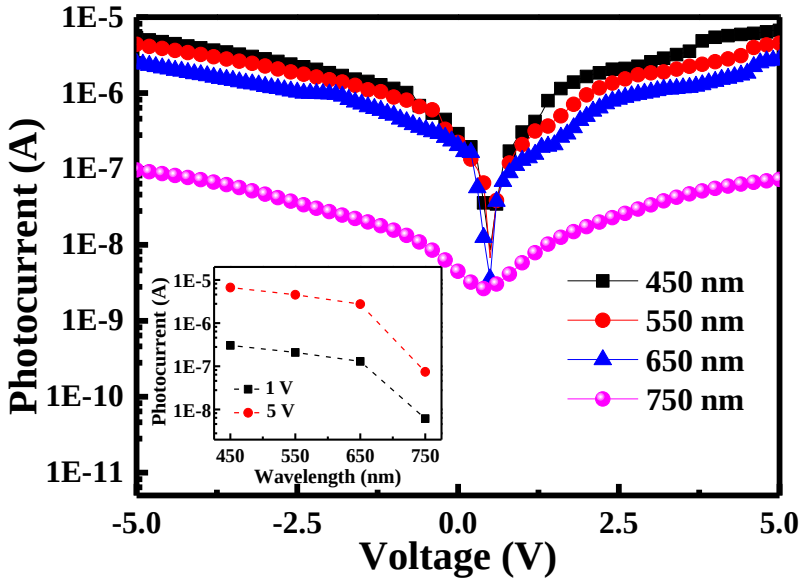

Figure 4.6 *Photocurrent vs Voltage with Varying Wavelength for MSM PD, the Inset Shows the Plot of Photocurrent as Function of Wavelength at Fixed Bias.*

The appropriateness of any photo-detecting device is verified by its performance parameter, namely, responsivity (R), external quantum efficiency (EQE), internal quantum efficiency (IQE), detectivity (D*) and noise equivalent power (NEP). Figure 4.7 represents the energy band diagrams of the MSM photodetector for unbiased, biased and biased with photo-incident condition, and Figure 4.8 shows the variation of the peak responsivity with bias voltage, confirming the increment in the peak response with increase in bias voltage. From the energy band diagram of the MSM photodetector, the depletion width and barrier potential at the reverse biased metal semiconductor junction of the

device increases with a rise in the bias voltage due to band bending as compared to that for unbiased condition. This results in an accumulation and transport of charge carriers at the junction under the influence of bias voltage and electric field governed by the thermionic field emission theory. The increased depletion width at reverse bias junction provides larger area to the incident photons under light illumination condition for electron-hole pair generation and charge separation before recombination due to increment of the electric field at junction, respectively [17,19]. Due to the *n*-type nature of MoS_2, no significant change in the electron concentration is expected via optical illumination, however, the concentration of minority carriers increases significantly. The combined effect of larger depletion width at larger bias voltage and photo carrier generation due to optoexcitation along with effect of photogain due to trap states, result in enhancement in current, responsivity and quantum efficiency [26].

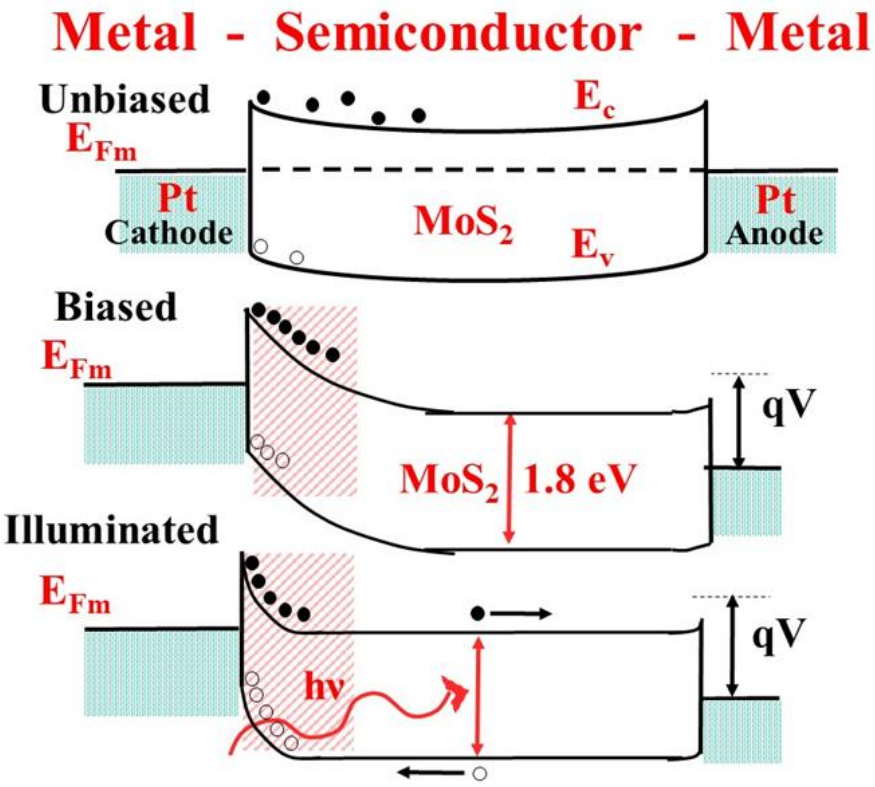

Figure 4.7 *Schematic Energy Band Diagram of MSM PD for Unbiased, Biased and Optical Incident Conditions.*

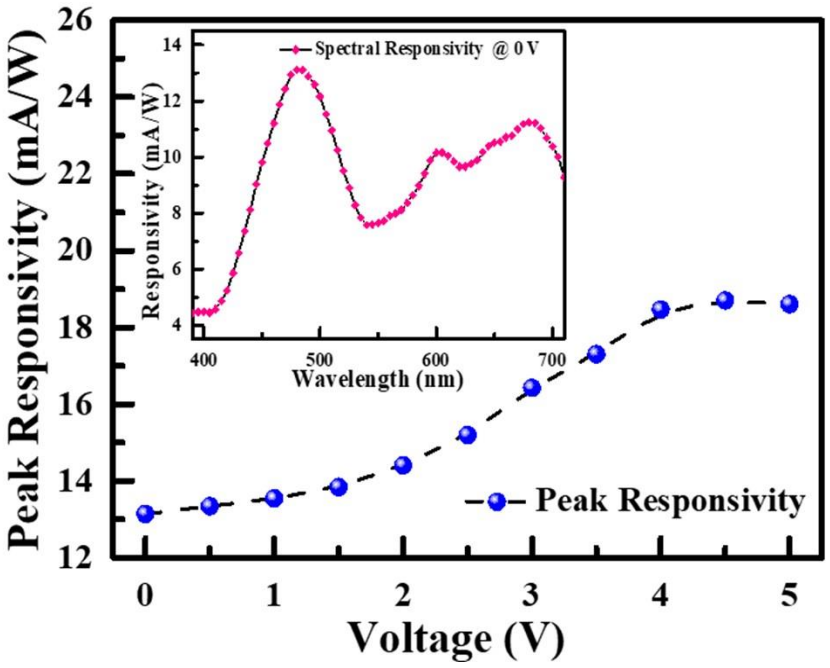

Figure 4.8 *Variation of Peak Responsivity with Voltage at Peak Response Wavelength, the Inset Shows the Spectral Response at 0 V.*

The peak responsivity rises from 13.15 to 18.59 mA/W, as bias voltage increases from 0 to 5 V. The high responsivity of the device even at 0 bias voltage suggests the potential of the device as self-powered photodetector. The inset of Figure 4.8 gives the spectral responsivity of the device for the wavelengths corresponding to visible spectrum of light, suggesting that that the device is sensitive towards the entire visible spectrum. Moreover, the peak response of 13.15 mA/W is observed at 480 nm, signifying the band selective response of the device. A similar kind of responsivity behavior is observed by other researchers and it is attributed to various defects presents in MoS_2 and is also consistent with the results presented in Figure 4.6 [24,27].

To further investigate the MSM device for photodetection application, EQE measurement is performed, and the results are presented in Figure 4.9. The measurements provide a peak EQE of 14.22% at around 480 nm at 0 V. The EQE corresponding to the energy bandgap (1.82 eV for λ= 681 nm) of MoS_2 monolayer is 8.72%. This spectral variation plot of EQE for wavelength range of 400 to 700 nm, suggests the potential of

MoS_2 MSM device to efficiently detect complete visible light spectrum [28]. In the inset of Figure 4.9, the variation of EQE and IQE with external bias voltage is presented at 480 nm. The IQE of the MSM device is calculated by IQE=EQE/(1-Ʀ), where Ʀ is the reflectance of the material. The curves indicate that the maximum variations in the EQE and IQE are 7.64% and 9.09%, respectively, as voltage varies from 0 to 5 V.

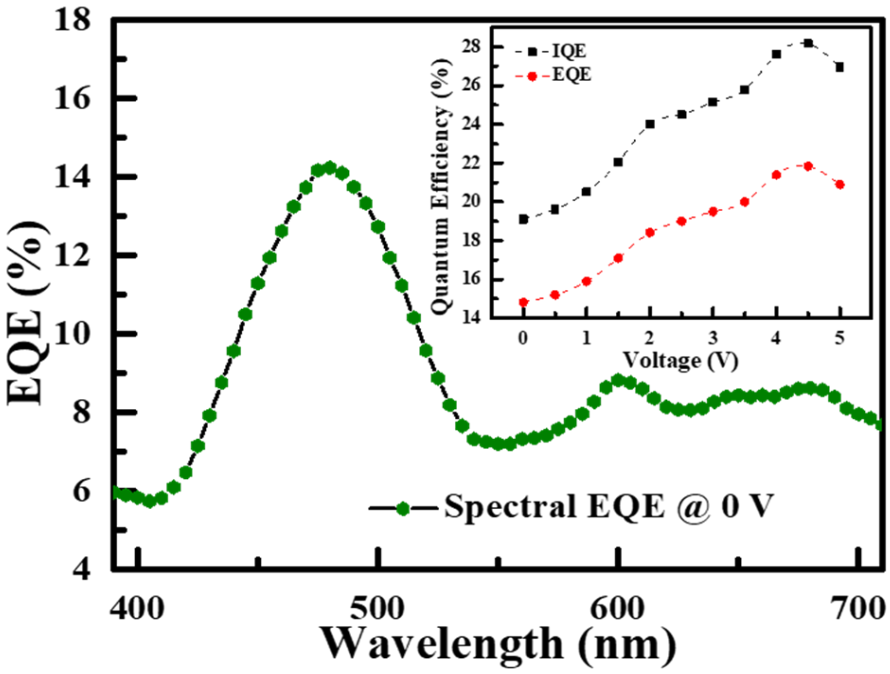

Figure 4.9 *Spectral External Quantum Efficiency, the Inset Shows the EQE and IQE with Biased Voltage at Peak Response Wavelength.*

Detectivity and NEP are the two other crucial performance parameters of any photodetector and they are quantified as suitability of the device to detect weak signals and sensitivity of the photodetector. In Figure 4.10, detectivity and NEP of the MoS_2 device are depicted with varying bias voltage. The detectivity and NEP are calculated via following equations:

$$D^* = \frac{R.A^{1/2}}{(2qI_D)^{1/2}} \tag{4.1}$$

$$NEP = \frac{(A.B)^{1/2}}{D^*} \tag{4.2}$$

$$\text{PDCR} = \frac{I_{pc} - I_D}{I_D} \qquad (4.3)$$

where A is the effective area, I_D is the dark current and B is the bandwidth [17]. Detectivity is directly proportional to responsivity, and, hence, it varies rapidly as voltage is increased initially and then is saturated. The decrease in the detectivity with the increase in bias voltage is attributed to the dominant effect of dark current at higher voltage i.e. increased by an order of 2 as the bias voltage increases from 0 to 5 V and this variation of I_D is also observed in Figure 4.4. The amount of incident optical power, which is equal to the noise power from all sources in the detector, is termed as NEP; inversely proportional to the detectivity of the photodetector. The NEP level of the MSM device is calculated on the assumption that the major contributing factor is shot noise due to the dark current [17,29]. The peak detectivity and NEP are 1.11×10^{11} cm.Hz$^{0.5}$W^{-1} at 0 V and 1.24×10^{-11} W at 5 V, respectively, for the wavelength corresponding to peak responsivity. The variations in detectivity and NEP are reduction of 77.58% and increment of 222.62%, respectively, for the voltage variation from 0 to 5 V.

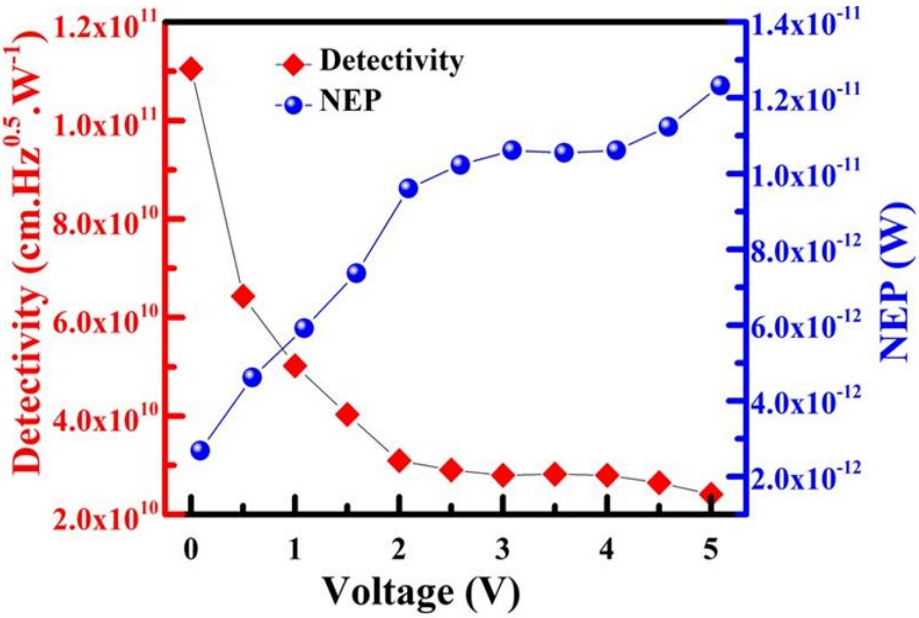

Figure 4.10 *Detectivity and NEP of the MSM PD.*

In order to investigate the time response or photoswitching characteristics, temporal response of the device at 5 V is studied and it is displayed in Figure 4.11. The plot suggests that a very sharp rise and fall in the photocurrent is observed with the toggling of ON/OFF state of the incident light. The I_{on}/I_{off} ratio obtained is 256 for 5 V DC supply, where I_{on} is the measured photocurrent in the light incident condition and I_{off} is the measured current in the absence of illumination, respectively. The rise and fall times of a photodetecting device depend on many parameters, including nature of the material, junction interface, recombination time, geometry of metal contacts, surface defects, and trap distribution. As discussed above, incident photon energy activates the defect based trap states, which are acting as recombination centres and thus help in the providing very small values of rise and fall times.

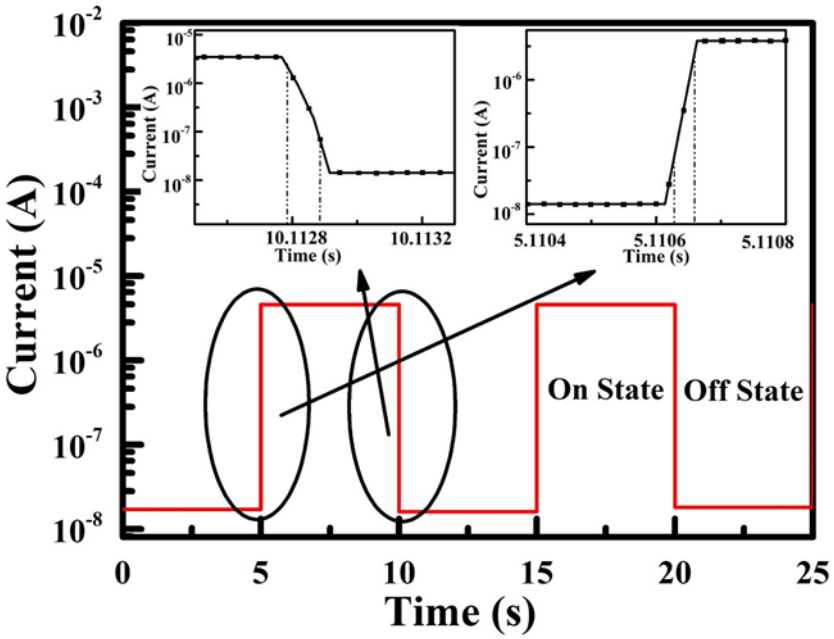

Figure 4.11 *Plot of Photoswitching Characteristic of the MSM PD.*

In the insets of Figure 4.11, the exact values of the rise and fall times are calculated as 0.06 and 0.14 ms, respectively. The observed value of the rise time is the best as reported for MoS_2 monolayer MSM detector [14,30]. The small values of the response times of the device suggest its appropriateness for the applications like smoke detection, relay

switches, replacement of avalanche photodiode, etc, where the ultrafast detection is a crucial parameter of the device.

The photo to dark current ratio (PDCR) of the device for different incident wavelengths at 0 and 5 V are calculated using Equation 4.3, where I_{pc} is the photocurrent. The PDCR at 0 V suggests the insignificant change in the photocurrent with wavelength, whereas for 5 V, PDCR value decreases from 529 to 190 as wavelength increases from 450 to 650 nm. The calculated PDCR results are in the agreement with Figure 4.6. The significant value of the PDCR for 5 V also validates the observed peak response and EQE at higher bias voltage.

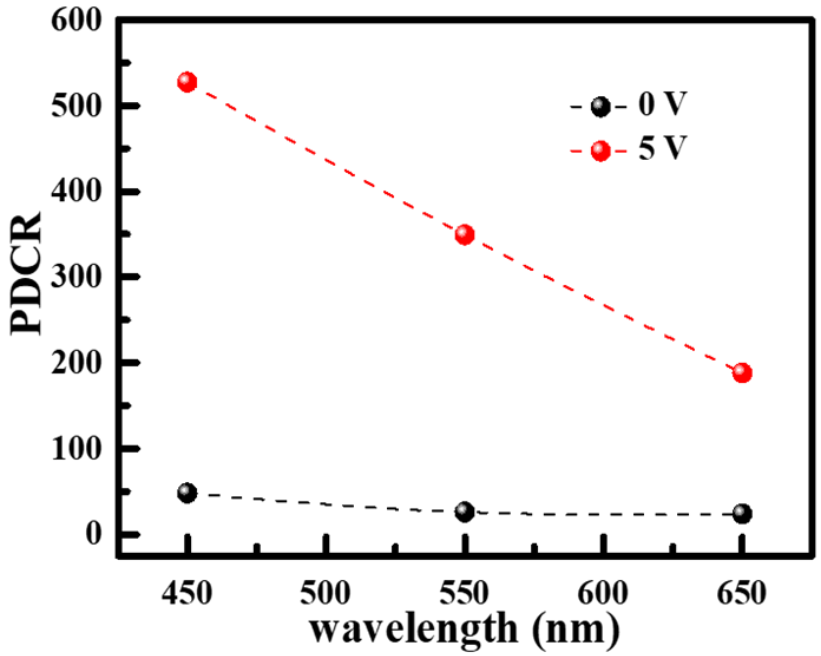

Figure 4.12 *Photocurrent to Dark Current Ratio (PDCR) at Different Wavelength.*

Table 4.1 shows a comparison of various performance parameters with those reported in the literature for MoS_2 monolayer MSM photodetectors. The ultrafast nature of the fabricated MSM device in terms of lowest rise time and fall time is emphasized in the Table. Also, the importance of this work is highlighted in terms of evaluating all the crucial performance parameters of the MoS_2 monolayer MSM photodetector under one head.

Table 4.1: *Comparative Analysis of Performance Parameters of MoS_2 Monolayer PD*

S.No.	Metal Contact	Dark Current @ 0 V	Peak Responsivity	Rise Time	Fall time
11	Ti/Au	~10^{-9} A	37 A/W @ 0V	-	-
12	Ti/Au	~10^{-9} A	~10^{4} A/W@ 0 V	120 ms	**~10^{3} ms**
14	Au	~10^{-9} A	8 mA/W @ 10 V and ~475 nm	1 s	**0.7 s**
15	Pd/Au	~ 10^{-12} A	0.7 A/W @ 1 V and 450-680 nm	0.17 s	-
25	Ag/Au	-	~0.25-0.9 mA/W @ 1 V and 450 nm	0.5 ms	**0.8 ms**
27	Ag	~10^{-6} A	0.11 A/W @ 1 V and ~525 nm	2.7 s	**2.6 s**
28	Ag	~10^{-5} A	0.13 A/W @ 1 V and ~532 nm	89 ms	**92 ms**
Present work	**Pt**	**3.76×10^{-10} A**	**18.59 mA/W @ 5 V and 480 nm**	**0.06 ms**	**0.14 ms**

4.4. Conclusion

In summary, MoS_2 monolayer was successfully grown in CVD furnace with maximum side length of 120 μm, as verified by optical microscopy, spectroscopic ellipsometry and Raman spectroscopy. This MoS_2 monolayer was then wet transferred over Pt interdigitated electrode on glass substrate to obtain a MoS_2 monolayer MSM photodetector. The photodetector performance was analyzed by dark and light I-V measurements, spectral responsivity, external quantum efficiency, detectivity, noise equivalent power and photo switching characteristic (temporal response). At 5 V, the dark current of the device increases to 1.61×10^{-7} A from 5.37×10^{-8} A as operating temperature increases from 25 ^{o}C to75 ^{o}C, while photocurrent increases from 3.02×10^{-6} A to 8.43×10^{-6} A with decrease in 28.17 %, respectively. The peak detectivity and NEP are 1.11×10^{11} cm.$Hz^{0.5}W^{-1}$ and 1.24×10^{-11} W, respectively. The rise and fall time are 0.06 ms and 0.14 ms, respectively, and the photocurrent on/off ratio is 256. The study suggests that MoS_2

monolayer based photodetector has a great potential for self-powered and high switching device.

4.5. References

[1] Choi, W., Choudhary, N., Han, G.H., Park, J., Akinwande, D. and Lee, Y.H., "Recent development of two-dimensional transition metal dichalcogenides and their applications," Materials Today, 20, 3, 116-130, 2017.

[2] Kolobov, A.V., and Junji, T., "Two-dimensional transition-metal dichalcogenides," Springer, 239, 2016.

[3] Mahatha, S.K., Patel, K.D. and Menon, K.S., "Electronic structure investigation of MoS_2 and $MoSe_2$ using angle-resolved photoemission spectroscopy and ab initio band structure studies," Journal of Physics: Condensed Matter, 24, 475504, 2012.

[4] Zhao, W., Ghorannevis, Z., Chu, L., Toh, M., Kloc, C., Tan, P.H. and Eda, G., "Evolution of electronic structure in atomically thin sheets of WS_2 and WSe_2," ACS Nano, 7, 1, 791-797, 2013.

[5] Cassabois, G., Valvin, P. and Gil, B., "Hexagonal boron nitride is an indirect bandgap semiconductor," Nature Photon, 10, 262-266, 2016.

[6] Eda, G., Yamaguchi, H., Voiry, D., Fujita, T., Chen, M. and Chhowalla, M., "Photoluminescence from chemically exfoliated MoS_2," Nano Letters, 11, 5111-5116, 2011.

[7] Li, H., Zhang, Q., Yap, C.C.R., Tay, B.K., Edwin, T.H.T., Olivier, A. and Baillargeat, D., "From bulk to monolayer MoS_2: evolution of Raman scattering," Advanced Functional Materials, 22, 1385-1390, 2012.

[8] Splendiani, A., Sun, L., Zhang, Y., Li, T., Kim, J., Chim, C.Y., Galli, G. and Wang, F., "Emerging photoluminescence in monolayer MoS_2," Nano Letters, 10, 1271-1275, 2010.

[9] Wang, X., Feng, H., Wu, Y. and Jiao, L., "Controlled synthesis of highly crystalline MoS_2 flakes by chemical vapor deposition," Journal of the American Chemical Society, 135, 5304-5307 2013.

[10] Lee, Y.H., Zhang, X.Q., Zhang, W., Chang, M.T., Lin, C.T., Chang, K.D., Yu, Y.C., Wang, J.T.W., Chang, C.S., Li, L.J. and Lin, T.W., "Synthesis of large-area MoS_2 atomic layers with chemical vapor deposition," Advance Materials, 24, 2320-2325, 2012.

[11] Wang, W., Zeng, X., Warner, J.H., Guo, Z., Hu, Y., Zeng, Y., Lu, J., Jin, W., Wang, S., Lu, J. and Zeng, Y., "Photoresponse-bias modulation of a high-performance MoS_2 photodetector with a unique vertically stacked 2H-MoS_2/1T@ 2H-MoS_2 structure," ACS Applied Materials & Interfaces, 12, 29, 33325-33335, 2020.

[12] Kufer, D. and Konstantatos, G., "Highly sensitive, encapsulated MoS_2 photodetector with gate controllable gain and speed," Nano Letters, 15, 7307-7313, 2015.

[13] Taffelli, A., Dirè, S., Quaranta, A. and Pancheri, L., "MoS_2 based photodetectors: a review," Sensors, 21, 2758, 2021.

[14] Le, C.T., Senthilkumar, V. and Kim, Y.S., Photosensitivity "Study of Metal-Semiconductor-Metal Photodetector Based on Chemical Vapor Deposited Monolayer MoS_2," Journal of Nanoscience and Nanotechnology, 15, 8133-8138, 2015.

[15] Moun, M., Singh, A., Tak, B.R. and Singh, R., "Study of the photoresponse behavior of a high barrier Pd/MoS_2/Pd photodetector," Journal of Physics D: Applied Physics, 52, 325102, 2019.

[16] Patel, C., Singh, R., Dubey, M., Pandey, S.K., Upadhyay, S.N., Kumar, V., Sriram, S., Than Htay, M., Pakhira, S., Atuchin, V.V. and Mukherjee, S., "Large and Uniform Single Crystals of MoS_2 Monolayers for ppb-Level NO_2 Sensing," ACS Applied Nano Materials, 5, 7, 9415–9426, 2022.

[17] Bhardwaj, R., Sharma, P., Singh, R., Gupta, M., and Mukherjee, S., "High responsivity $Mg_xZn_{1-x}O$ based ultraviolet photodetector

fabricated by dual ion beam sputtering," IEEE Sensors Journal, 18, 7, 2744-2750, 2018.

[18] Yim, C., O'Brien, M., McEvoy, N., Winters, S., Mirza, I., Lunney, J.G. and Duesberg, G.S., "Investigation of the optical properties of MoS_2 thin films using spectroscopic ellipsometry," Applied Physics Letters, 104, 103114, 2014.

[19] Saenz, G.A., Karapetrov, G., Curtis, J. and Kaul, A.B., "Ultra-high photoresponsivity in suspended metal-semiconductor-metal mesoscopic multilayer MoS_2 broadband detector from UV-to-IR with low Schottky barrier contacts," Scientific Reports, 8, 1276, 2018.

[20] Siddharth, G., Sengar, B.S., Garg, V., Khan, M.A., Singh, R. and Mukherjee, S., "Analytical performance analysis of CdZnO/ZnO-based multiple quantum well solar cell," IEEE Transactions on Electron Devices, 67, 3, 1047-1051, 2020.

[21] Bhattacharjee, S., Biswas, P., Solanke, S., Muralidharan, R., Nath, D. and Bhat, N., "Optoelectronics based on Vertical Transport in Multi-layer MoS_2," 76th Device Research Conference (DRC), 1-2, 2018.

[22] Fortin, E. and Sears, W.M., "Photovoltaic effect and optical absorption in MoS_2," Journal of Physics and Chemistry of Solids, 43, 9, 881-884, 1982.

[23] Han, J., Li, J., Liu, W., Li, H., Fan, X. and Huang, K., "A novel flexible broadband photodetector based on flower-like MoS_2 microspheres," Optics Communication, 473, 125931, 2020.

[24] Xie, Y., Zhang, B., Wang, S., Wang, D., Wang, A., Wang, Z., Yu, H., Zhang, H., Chen, Y., Zhao, M. and Huang, B., "Ultrabroadband MoS_2 photodetector with spectral response from 445 to 2717 nm," Advanced Materials, 29, 17, 1605972, 2017.

[25] Yin, Z., Li, H., Li, H., Jiang, L., Shi, Y., Sun, Y., Lu, G., Zhang, Q., Chen, X. and Zhang, H., "Single-layer MoS_2 phototransistors," ACS Nano, 6, 1, 74-80, 2012.

[26] Perea-López, N., Lin, Z., Pradhan, N.R., Iñiguez-Rábago, A., Elías, A.L., McCreary, A., Lou, J., Ajayan, P.M., Terrones, H., Balicas, L. and Terrones, M., "CVD-grown monolayered MoS_2 as an effective photosensor operating at low-voltage," 2D Materials, 1, 011004, 2014.

[27] Yore, A.E., Smithe, K.K., Jha, S., Ray, K., Pop, E. and Newaz, A.K.M., "Large array fabrication of high performance monolayer MoS_2 photodetectors," Applied Physics Letters, 111, 043110, 2017.

[28] Kaushik, V., Varandani, D., Das, P. and Mehta, B.R., Layer dependent photoresponse behavior of chemical vapor deposition synthesized MoS_2 films for broadband optical sensing. Journal of Physics D: Applied Physics, 52, 475302, 2019.

[29] Dhar, S., Majumder, T. and Mondal, S.P., "Graphene quantum dot-sensitized ZnO nanorod/polymer Schottky junction UV detector with superior external quantum efficiency, detectivity, and responsivity," ACS Applied Material Interfaces, 8, 46, 31822-31831, 2016.

[30] Tsai, D.S., Liu, K.K., Lien, D.H., Tsai, M.L., Kang, C.F., Lin, C.A., Li, L.J. and He, J.H., "Few-layer MoS_2 with high broadband photogain and fast optical switching for use in harsh environments," ACS Nano, 7, 5, 3905-3911, 2013.

Chapter 5

ZnO film based UV photodetector on flexible polyimide substrate

5.1. Introduction

In recent years, device miniaturization has paved the way for a new paradigm of future electronics and optoelectronics. One of the new dimensions in this aspect is flexible electronics, having high compatibility with arbitrarily shaped surfaces, wearable, complex geometries, lightweight, and portable applications [1-2]. Ultrathin sensors and detectors, foldable display, and health monitoring patches are combining the best of both optoelectronics and flexible electronics in a single unit [3].

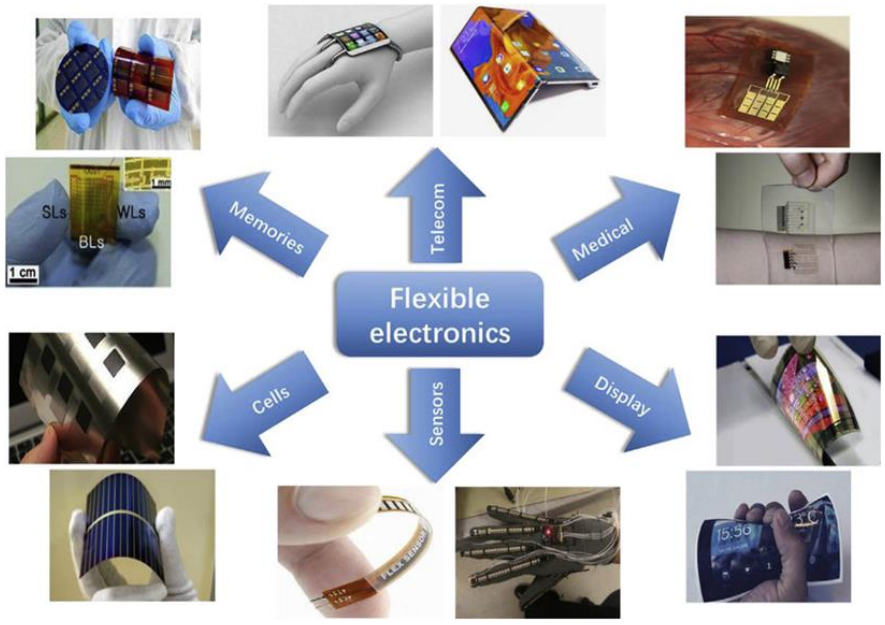

Figure 5.1 *Different Research Aspects of flexible Electronics.*

Advancing in the optoelectronics, the self-powered Ultraviolet (UV) photodetectors (PD) are now being used for nanofabrication technologies, environmental monitoring, health, and infrastructure applications apart from their conventional usage in

communication, ozone sensing, leak and flame detection [4]. A low temperature deposition technique with high precision and great miniaturization is often applicable for fabrication of flexible devices. Over the last two decades, ZnO emerged as a potential wide band gap piezoelectric semiconductor and a replacement of GaN due to its enormous applications in nano generator, nanowire, etc. [5]. Along with no toxicity and abundance, ZnO alloying with different elements expands the material's application range in the blue and near ultraviolet spectral bands [6]. The primary ZnO based PD discussed in the literature are homojunction, MSM, heterojunction, and *p-i-n* structures, while each one is having their own individual advantages [7]. However, the most common PD structure is metal-semiconductor-metal (MSM), due to its ease of fabrication, inherently low capacitance, linear structure, improved speed in impact of metallization, and higher bandwidth for the same active area [8].

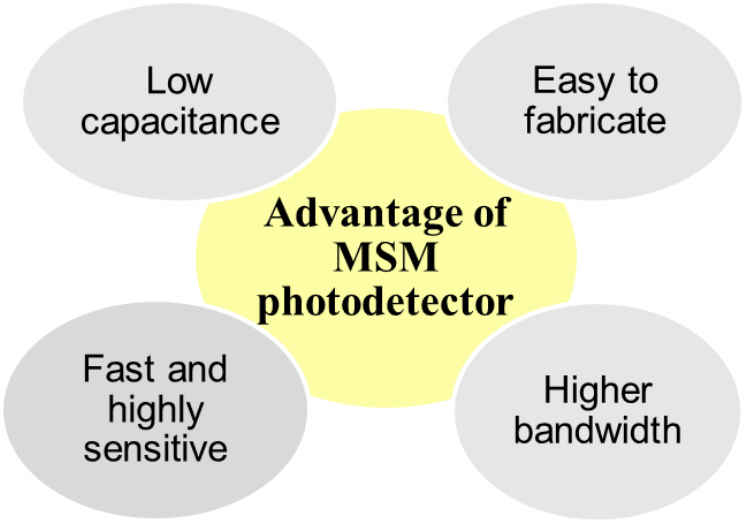

Figure 5.2 *Root map of Advantages of MSM Devices.*

Further, conventional PD structure with additional internal gain has also been explored, to enhance the efficiency of the device. As of now, various flexible substrates are employed such as polyethylene terephthalate (PET), polyimide (PI), polydimethylsiloxane (PDMS), paper, polyvinyl chloride (PVC), etc. have been explored for analyzing

flexible UV PD's [9-11]. Among these, PI is best suited owing to its significant temperature resistance, low thermal expansion, cost effectiveness and lightweight nature [12].

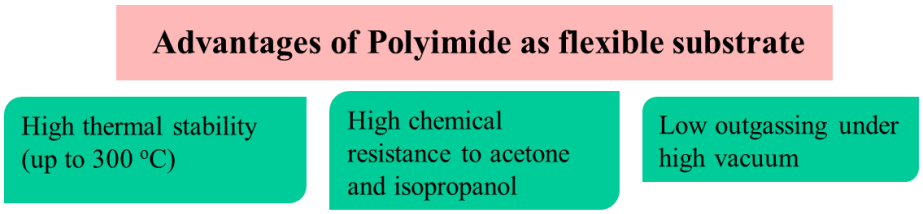

Figure 5.3 *Advantages of Polyimide Substrate in flexible Electronics.*

A new dimension in the research is added by regulating the interface and controlling the performance of the flexible PD under the piezo-phototronic effect [13]. Many literatures have tried to cover different scopes of flexible ZnO UV PD under different bending conditions, however, they lack in covering every aspect of the performance parameters of PD combining experimental and analytical analysis in a single subunit [12, 14]. In this work, an MSM based PD structure is developed over PI substrate by sputtering ZnO thin film on e-beam deposited interdigitated Cr/Au electrode (IDE). The PD is then evaluated for performance parameters such as dark and photo current, responsivity, temporal response, and quantum efficiency with bias voltage, both in normal and varying device bending conditions. Moreover, the classic thermionic emission model and the device physics of flexible PD, due to the combined effect of electric field and strain, are discussed in the work.

5.2. Experimental Details

The industrial grade PI substrate is plasma cleaned before patterning the IDE's on top of it. The IDEs are photo-lithographically patterned using 5214 E image reversal photoresist with an electrode width of 10 μm and spacing of 9 μm between them. Cr/Au electrode

with a thickness of 20/200 nm is deposited using an e-beam evaporation technique at room temperature with a working pressure of 1.5×10^{-7} Torr having a deposition rate of 0.3 Å/s. A 325 nm thick ZnO film is deposited on the top of IDEs using Kurt J. Lesker PVD75 Pro-line reactive magnetron sputtering technique. The deposition of the ZnO film is carried for 0.5 hours in 2:3, O2:Ar ambience at 250 °C [15]. The complete fabricated MSM PD device along with its camera image and dimension of IDEs are shown in Figure 5.4 (a), (b) and (c), respectively.

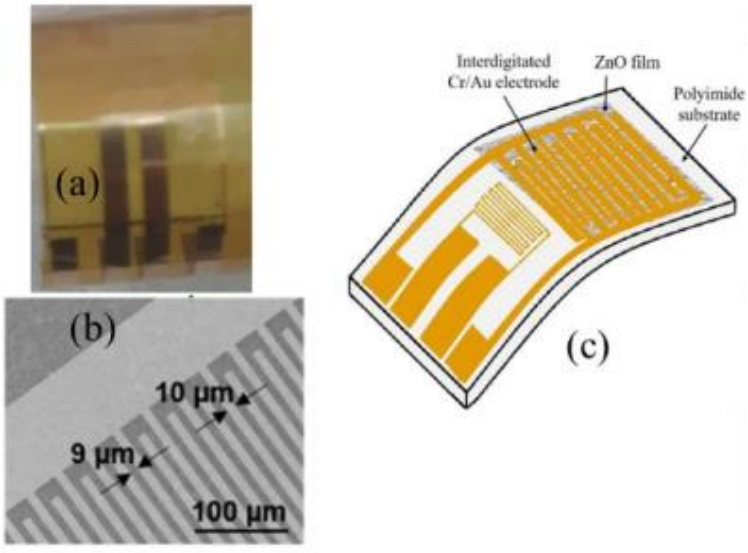

Figure 5.4 *(a) Camera image of Flexible MSM UV PD, (b) Dimension of IDEs, and (c) Fabricated ZnO based device over IDEs.*

The responsivity and quantum efficiency are measured using Bentham PV-300 photovoltaic characterization system. The temporal response of the device is analyzed by interfacing the Keithley DMM6500 digital multimeter, D.C. sourcemeter, and PV 300 system [16]. Furthermore, the PD results are analytically scrutinized and explained by classic thermionic emission theory and Schottky barrier height (SBH) variations, for various bending conditions [17]. Examination of the complete device is performed at normal (flat) and different bending conditions of 10 mm, 8 mm, and 5 mm diameter, respectively.

Thermionic Field Emission Theory:

Thermionic emission is a field emission-related phenomenon. The thermal energy provided to charge carriers overpowers the binding potential, also recognised as the work function of metals, allowing electrons to break free from the solid's surface. Electrons or ions can act as charge carriers. The Time - dependent model of metal, the triangular vacuum potential barrier, and the equilibrium electron emission are all-used in the basic theoretical model of thermionic emission [18-19]. The crucial point of thermionic emission is that high temperature drives electrons in the conduction band to highly excited states, where their kinetic energy overcomes the vacuum potential barrier.

Piezo-phototronic effect:

The piezoelectric potential (piezopotential) created by adding a strain to a semiconductor with piezoelectricity to govern carrier generation, transport, separation, and/or recombination at metal-semiconductor junction or *p-n* junction for enhancing the performance of optoelectronic devices is referred to as the piezo-phototronic effect [13-14].

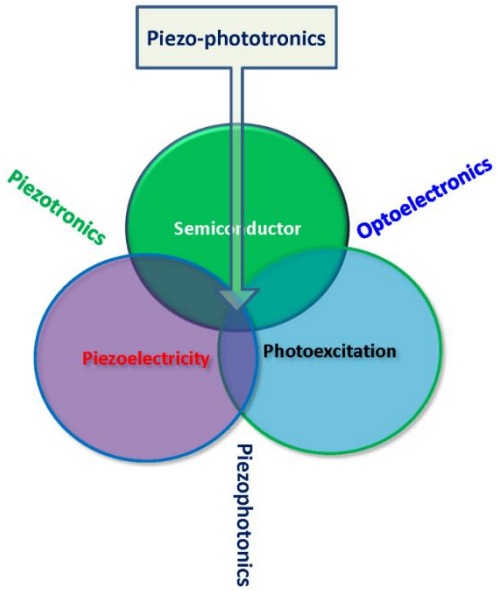

Figure 5.5 *Schematic of the Different Aspects of Semiconductor on the Basis of different Properties.*

5.3. Results and Discussion

The MSM PD is initially investigated for the dark and photo current with varying biased voltage (-10 V to +10 V) under exposure to different incident light wavelengths, shown in Figure 5.6. Interestingly, it is observed that the MSM device is selective for the light wavelength less than 375 nm which is in good agreement with the deposited thin film bandgap of ZnO i.e. 3.37 eV. This solidify that the fabricated MSM device is behaving as UV detector [20]. Moreover, the fabricated MSM based UV PD exhibits the highest selective behavior towards light wavelength of 325 nm which is attributed to the combined effect of material's bandgap and presence of unintentional growth defects. The analysis further confirms that for light wavelength higher than the 368 nm, corresponding to bandgap of ZnO, the device doesn't show any selectivity i.e. behaves as a transparent film and further no variations in photo current at those wavelengths compared to dark current is observed [21].

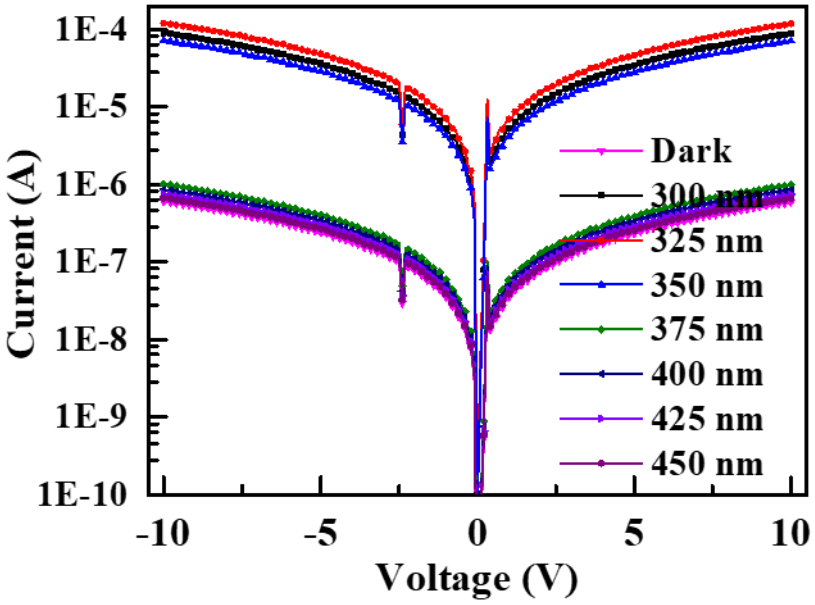

Figure 5.6 *I-V Analysis of the MSM Device at Dark and different Incident Wavelengths.*

The I-V performance of the MSM UV PD is investigated under normal (flat) and different bending conditions with an outward

bending of 10, 8, and 5 mm diameter, respectively. Figure 5.7 depicts the I-V analysis in both dark and incident light wavelength of 325 nm along with different bending conditions. It is evident from Figure 5.7 that the device bending under dark conditions doesn't significantly influence the performance, suggesting that the impact of the device bending is balanced by the mobility of carrier through the available trap states due to growth defects [22]. Figure 5.7 also exhibits that the photo current of the MSM device decreases as the bending increases for lower voltage (0-3.5 V) and for higher voltages, it approaches towards the photocurrent value of the device in normal (flat) condition.

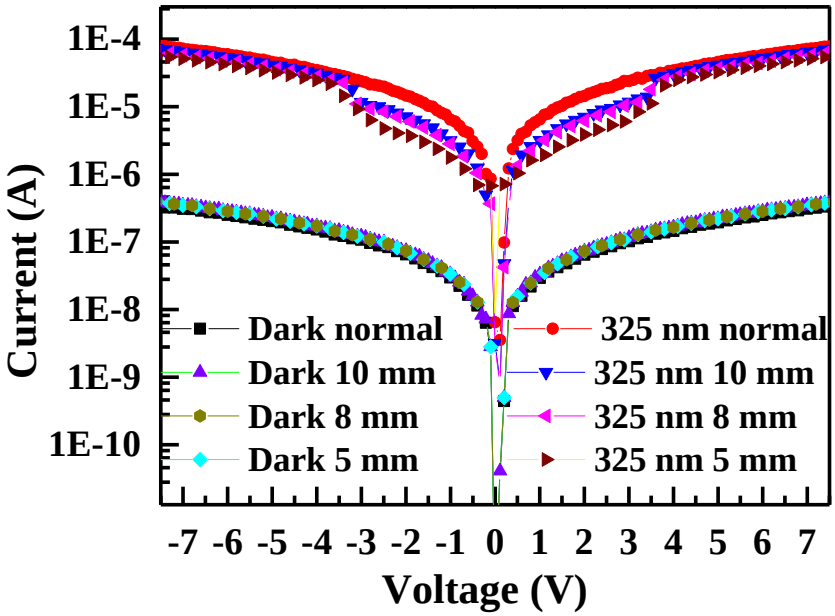

Figure 5.7 *I-V Analysis at Normal and Different Device Bending Conditions.*

This observation is explained by the classic thermionic field emission theory and piezo-phototronic effect [9, 23].

$$\varepsilon = \sqrt{\frac{2qN}{k_s}\left(V + V_{bi} - \frac{KT}{q}\right)} \tag{5.1}$$

$$ln\left(\frac{I_\varepsilon}{I_o}\right) = -\frac{q\,\Delta\emptyset}{KT} \tag{5.2}$$

The field emission theory explains the relation between strain (ε) and the biased voltage (V) is given by Equation 5.1. Where, q, k_s, N, V_{bi}, K,

and *T* are charge of electron, permittivity, carrier concentration, built-in potential, Boltzmann constant and temperature, respectively. The non-linear relation between the strain and biased voltage result in 33% reduction in slope of strain v/s voltage plot for the 3.5- 7 V compare to 0-3.5 V, suggesting that at higher voltage the impact of strain decreases as depicted in Figure 5.8.

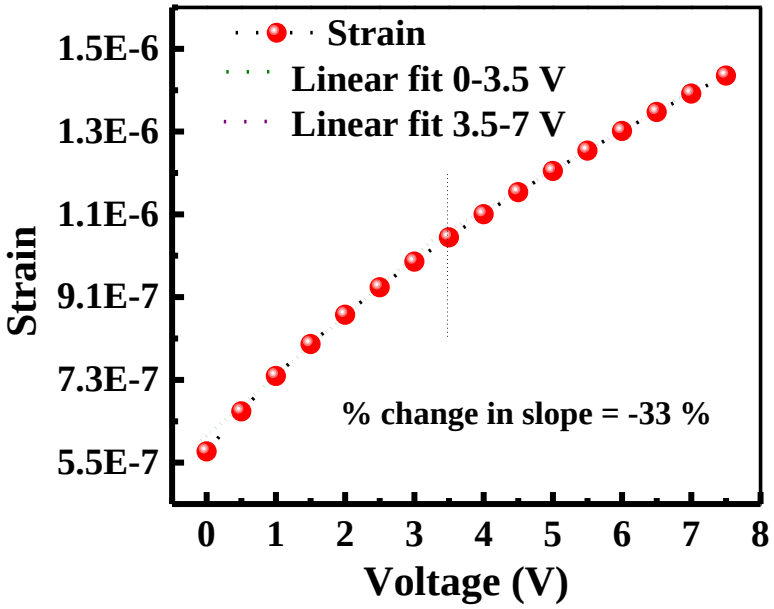

Figure 5.8 *Plot of Strain Variation with Voltage.*

Therefore, at higher voltage, performance of the device even in bended conditions is similar to the performance at normal condition, owing to negation of impact of strain to the device bending. This explanation is further supported by current dependence of Schottky contacts on Schottky Barrier Height ∅ (SBH) which is directly related with strain. The study of Zhang *et al.* suggests that for higher strain, change in SBH is high for lower voltages, resulting in significant reduction of photocurrent for bended conditions at lower voltages compared to normal condition [24]. The relation governing the relative change in SBH is given by Equation 5.2, where I_ε and I_o are current in bending and reference condition, and $\Delta\emptyset$ is change in SBH, respectively. By utilizing Equation 5.2, the change in SBH for photocurrent in bending conditions to the photocurrent at normal condition as reference is

calculated for different values of biased voltage. This relative change in the SBH (from normal to bending conditions) with varying biased voltage is plotted in Figure 5.9. The aforementioned Figure 5.9 confirms that for all the device bending conditions, relative change in SBH start saturating to a very lower value for the voltage above 3.5 V, justifying the approaching value of photocurrent to the normal condition.

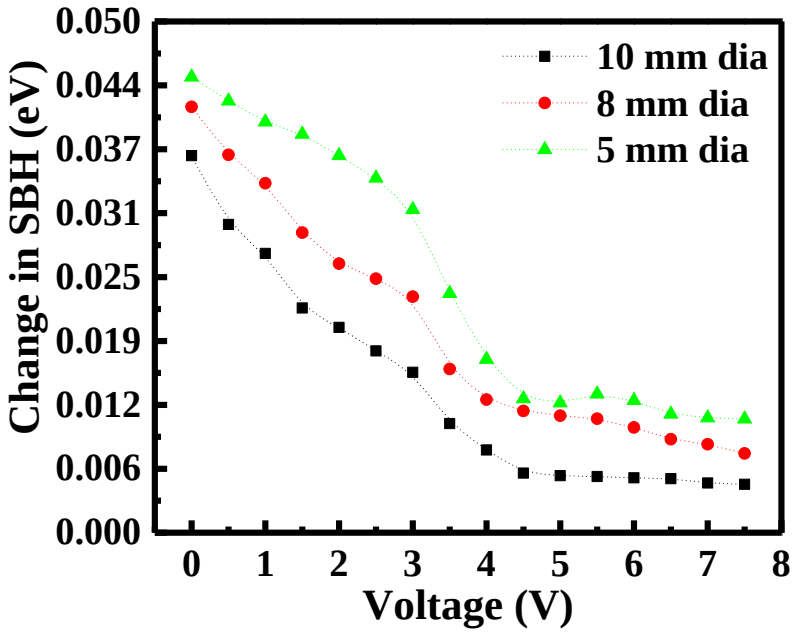

Figure 5.9 *Relative change in SBH with voltage.*

Furthermore, the combined effect of piezoelectric and photoexcitation properties of a semiconducting material, governs the physics of flexible PD under bending condition and termed as piezo-phototronic effect [10, 25]. As explained by the theoretical energy band diagram of the UV PD in Figure 5.10, this piezo-phototronic effect describe the impact of strain and the biased voltage on the change in SBH and charge carrier accumulation at the metal-semiconductor Schottky junction. The higher value in the relative change of SBH under bending results in reduction of photocurrent initially, which is compensated by increased electric field at higher biased voltage in the UV PD [23, 25]. Thus, the complete discussion of both, the thermionic field emission theory and piezo-phototronic effect explains photocurrent variation with voltage at different bending conditions of the PD.

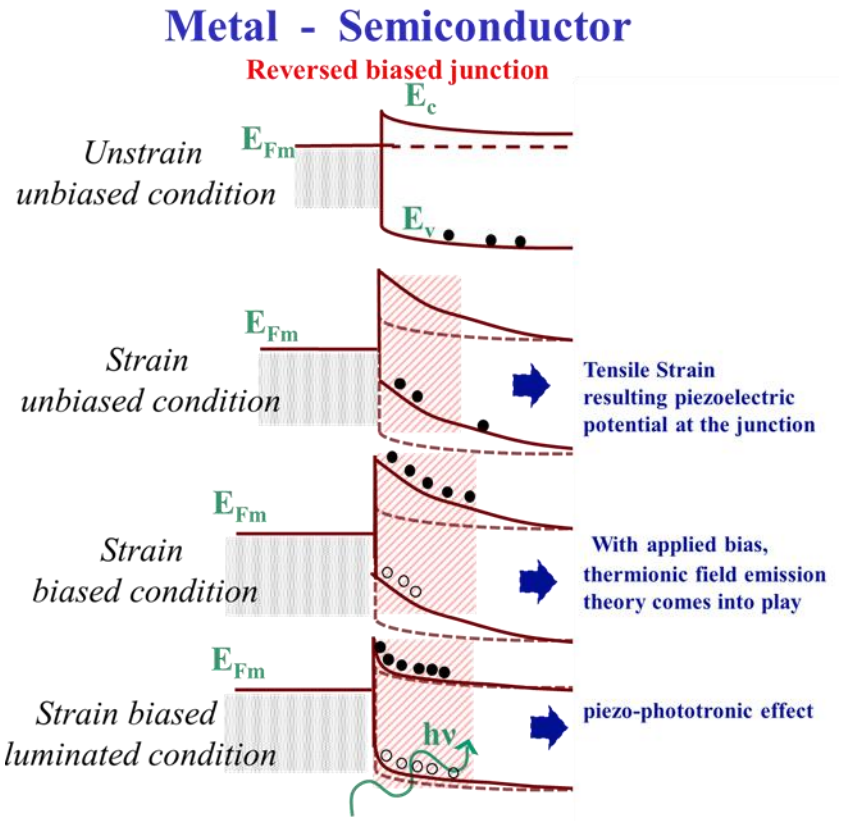

Figure 5.10 *Energy Band Diagram of Metal Semiconductor Junction under Different Condition.*

Hereafter, spectral response of the MSM PD which is another performance parameter of the PD is analyzed with varying voltages as shown in Figure 5.11 (a) and (b). As observed from the I-V analysis, the impact of strain completely dies out at 6 V, therefore, it is chosen for all the further analysis. The impact of spectral incidence at 0 V over the UV PD implies a narrow spectral selectivity of the device with a red shift with an increase in device bending conditions. This red shift in the spectral selectivity is attributed due to the decrease in the energy bandgap of the material with the increasing strain [27]. The inconsistent spectral response of the device is also expected due to dominating impact of strain at lower voltage during light illumination as explained in the I-V analysis. Figure 5.11 (b) portrays the spectral response of the PD at 6 V showing the broad selectivity of the PD with a slight impact of strain in different bending conditions. Both, Figure 5.11 (a) and (b) confirms that the device doesn't show any spectral selectivity above 350

nm concreating the observation of Figure 5.6 i.e. the performance of the device as UV PD.

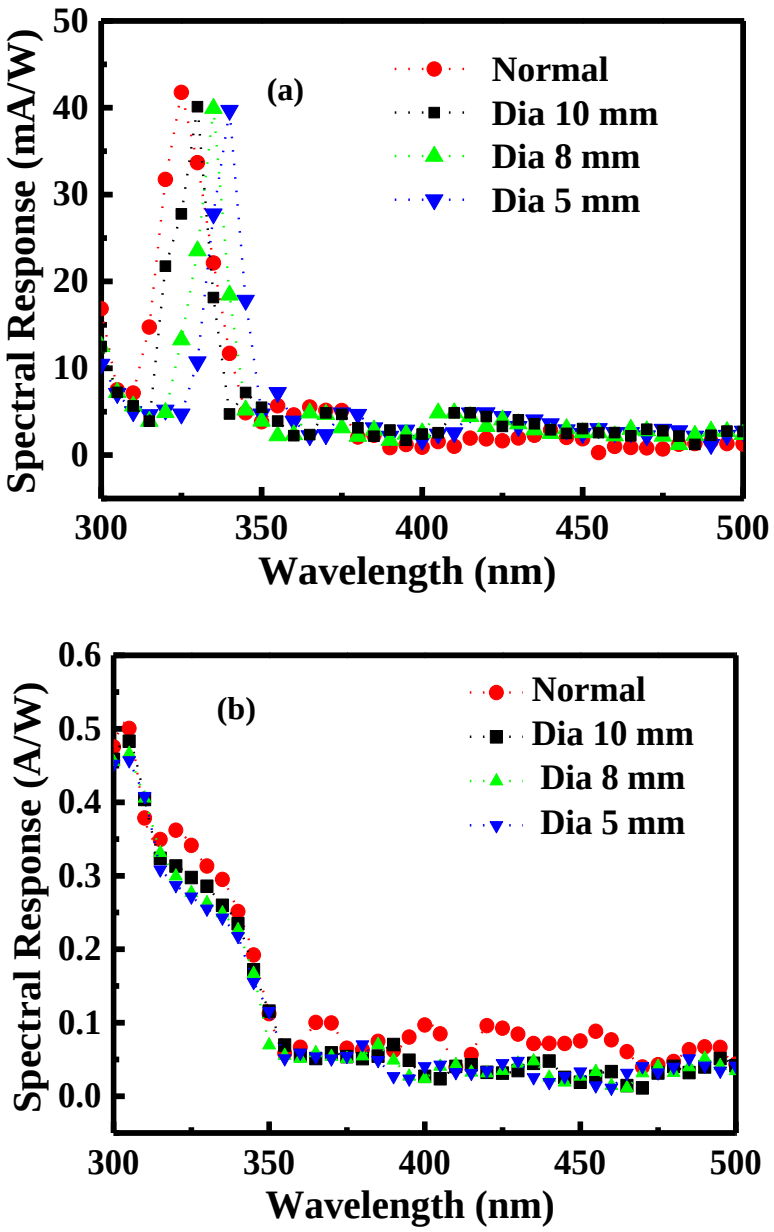

Figure 5.11 *Spectral Response at (a) 0 V, and (b) 6 V.*

The peak responsivity (R) variation with voltage for different bending conditions is shown in Figure 5.12 (a). The responsivity of the PD is defined as the ratio of generated photocurrent to the incident optical power [16]. The results are in line with our discussion of thermionic field emission theory and piezo-phototronic effect, explaining impact of strain with varying voltage under spectral incidence [23, 28]. The higher

value of the responsivity of the MSM device even under highest bended conditions confirms the reliability of the UV PD.

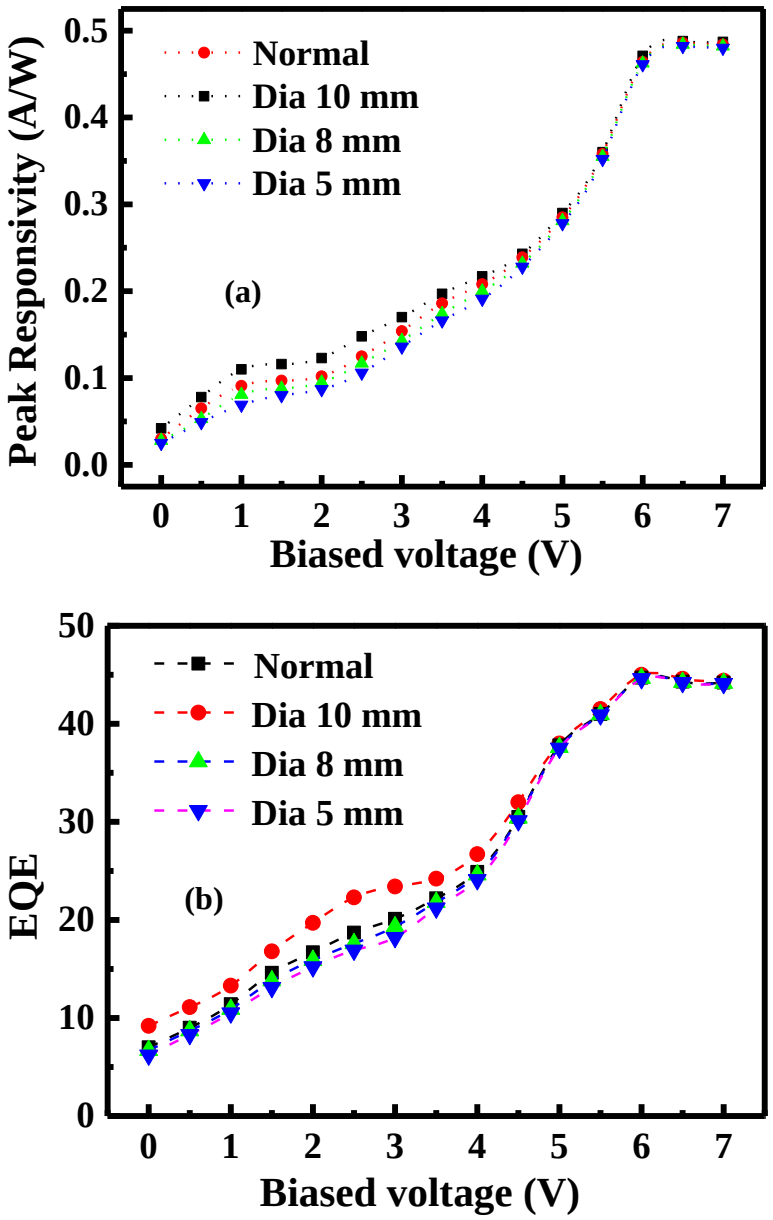

Figure 5.12 *Variation of (a) Peak Responsivity, and (d) External Quantum Efficiency with voltage.*

The external quantum efficiency (EQE) of a photodetector is defined as ratio of number of collected photocarriers at the output terminal to the number of incident photons on the PD. The EQE with the biased voltage is shown in Figure 5.12 (b) [16, 29]. The highest EQE obtained is 45.3 % for the UV PD at 6 V, which almost remains constant for any further

increase in voltage. The impact of strain dies out after 3.5 V with a maximum reduction of EQE of 5.24 % at 2.5 V from the normal condition.

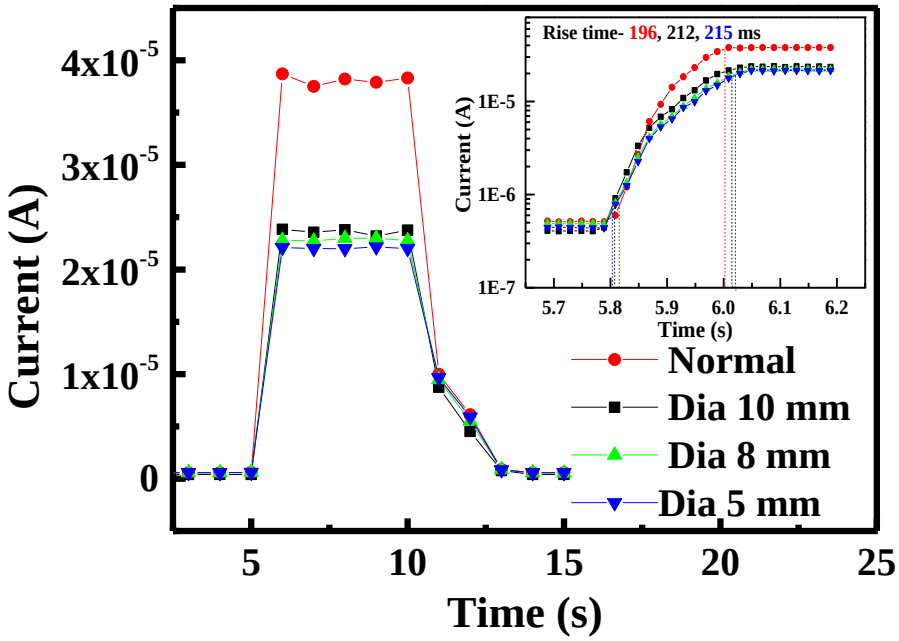

Figure 5.13 *Temporal Response of MSM UV PD and Inset of Figure is zoomed view to calculate rise time.*

Furthermore, the temporal-photoswitching response of the device is evaluated at 6 V shown in Figure 5.13. The I_{on}/I_{off} ratio in normal as well as in bending conditions are ~ 200 and the rise time in the normal condition is 196 ms which is increased to 215 ms in highest bended condition due to increase in interelectrode spacing. The fast response of the UV PD is attributed to the small dimension of the device leading to low value of RC constant due to small dimension of the device, and fast transition of photocarriers in depletion region because of high mobility under strong electric field [30]. The large fall time ~2.5 seconds is ascribed by the high relaxation time of generated photocarriers as the light illumination is vanished.

The photo to dark current ratio (PDCR) variation with different bending conditions at 6 V in Figure 5.14, illustrates that the performance of the flexible UV PD at higher voltage doesn't change considerably, due to the insignificant influence of strain. However, at 0 V the rapid rise in the

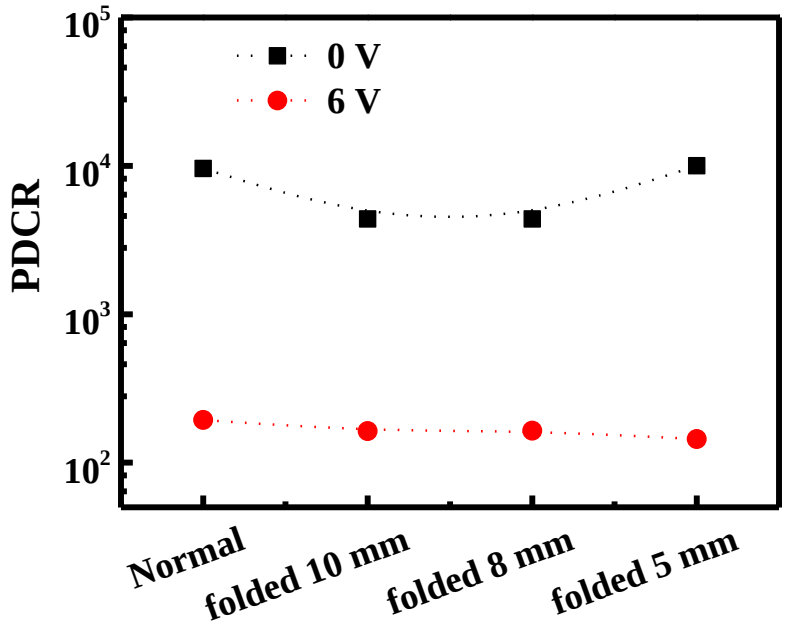

Figure 5.14 *PDCR of MSM UV PD at 0 and 6 V.*

photocurrent value under light illumination result in high PDCR value [31]. In comparison to the other similar work on flexible UV PD, this study covers the various performance parameters of PD and provides comparable results at a much lower voltage, proving its potential for the applications of wearable electronics [10, 12, 21].

Table 5.1: Comparison of the Present Work with Existing Literature

Ref. no.	Substrate	I_{pc}/I_D	Responsivity (A/W)	Rise time	Efficiency
[9]	PDMS	120 at 2 V	-	-	-
[23]	PET	10^3 at 20 V	0.36 at 30 V	-	-
[10]	PET	10^2 at 20 V	2.2 at 50 V	0.2 s	-
[29]	PET	10^2at 15 V	0.14 at 20 V	-	65 % at 20 V
[12]	PI	10^2at 20 V	0.045 at 20 V	-	0.7 % at 20 V
[11]	Paper	10^3at 10 V	0.9 at 10 V	2.1 s at 10 V	-
This work	**PI**	**10^2 at 6 V**	**0.5 at 6 V**	**0.215 s at 6 V**	**45.3 % at 6 V**

5.4. Conclusion

In this work, reactive magnetron sputtered ZnO based flexible UV PD in MSM structure is fabricated and investigated under various device bending conditions. The performance of the device is evaluated via I-V analysis, spectral response, EQE, detectivity, and photoswitching response. The mechanisms governing the physics of the flexible UV PD devices are discussed for bending and biased voltage conditions. The device performance in different bending conditions at high voltage is equivalent to the performance of the device under normal condition, which is a desirable for flexible electronics applications. The ZnO based UV PD provides the maximum photocurrent for 325 nm wavelength, with an I_{on}/I_{off} ratio of 215 at 6 V in normal condition. The spectral response of the device suggests its suitability as UV PD with a peak responsivity of 0.5 A/W. The EQE, PDCR, and photoswitching response of the device are quantified. This study highlights the potential of the UV PD for wearable electronic applications.

5.5. References

[1] A. Nathan et al., "Flexible Electronics: The Next Ubiquitous Platform," Proceedings of the IEEE, 100, Special Centennial Issue, 1486-1517, 2012.

[2] W. Gao, H. Ota, D. Kiriya, K. Takei, and A. Javey, “Flexible Electronics toward Wearable Sensing,” ACS Accounts of Chemical Research, 52, 3, 523-533, 2019.

[3] C. Pang, C. Lee, and K. Y.Suh, “Recent advances in flexible sensors for wearable and implantable devices,” Journal of Applied Polymer Science, 130, 3, 1429-41, 2013.

[4] H. Chen, K. Liu, L. Hu, A. A. A. Ghamdi, X. Fang, “New concept ultraviolet photodetectors,” Materials Today, 18, 9, 493-502, 2015.

[5] B. Kumar, and S. W. Kim, “Energy harvesting based on semiconducting piezoelectric ZnO nanostructures,” Nano Energy, 1, 3, 342-355, 2012.

[6] G. Siddharth et al., "Investigation of DIBS-deposited CdZnO/ZnO-based multiple quantum well for large-area photovoltaic application," IEEE Transactions on Electron Devices, 67, 12, 5587-5592, 2020.

[7] R. Singh, R. Bhardwaj, G. Siddharth, P. Kumar, and S. Mukherjee, "Analytical study of sputter-grown ZnO-based *p-i-n* homojunction UV photodetector," IEEE Sensors Journal, 21, 6, 7515-7521, 2021.

[8] K. Liu, M. Sakurai and M. Aono, "ZnO-Based ultraviolet photodetectors," Sensors, 10, 9, 8604-8634, 2010.

[9] J. Zhou et al., "Piezoelectric-potential-controlled polarity-reversible schottky diodes and switches of ZnO wires," Nano Letters, 8, 11, 3973-3977, 2008.

[10] W. Zhang et al., "Piezo-phototronic effect for enhanced sensitivity and response range of ZnO thin film flexible UV photodetectors", Journal of Applied Physics, 125, 024502, 2019.

[11] H. Li, J. Huang, Q. Zheng, and Y. Zheng, Flexible ultraviolet photodetector based ZnO film sputtered on paper," Vacuum, 172, 109089, 2020.

[12] J. Sun, M. Zhao, and D. Jiang, "Study on piezo-phototronic effect of AlZnO thin film flexible ultraviolet photodetector" Physica E: Low-dimensional Systems and Nanostructures, 140, 115149, 2022.

[13] Z. Gao, J. Zhou, Y. Gu, P. Fei, Y. Hao, G. Bao, and Z. L. Wang "Effects of piezoelectric potential on the transport characteristics of metal-ZnO nanowire-metal field effect transistor," Journal of Applied Physics, 106, 039901, 2009.

[14] C. W. Jeon, S. S. Lee, and I. K. Park, "Flexible visible-blind ultraviolet photodetectors based on ZnAl-layered double hydroxide nanosheet scroll," ACS Applied Materials & Interfaces, 11, 38, 35138-35145, 2019.

[15] B. Mandal et al., "π-conjugated amine-ZnO nanohybrids for the selective detection of CO2 gas at room temperature," ACS Applied Nano Materials, 1, 6912−6921, 2018.

[16] R. Bhardwaj, P. Sharma, R. Singh, M. Gupta and S. Mukherjee,

"High responsivity MgxZn1-xO based ultraviolet photodetector fabricated by dual ion beam sputtering," IEEE Sensors Journal, 18, 7, 2744-2750, 2018.

[17] Z. L. Wang et al., “Piezotronics and piezo-phototronics with third-generation semiconductors,” MRS Bulletin, 43, 922–927, 2018.

[18] “Chapter 15: Thermionic Emission Theory” Quantum Tunneling and Field Electron Emission Theories, 231-235,2014.

[19] https://en.wikipedia.org/wiki/Field_electron_emission.

[20] P. Sharma, R. Singh, V. Awasthi, S. K. Pandey, and S. Mukherjee, “Detection of a high photoresponse at zero bias from a highly conducting ZnO:Ga based UV photodetector,” RSC Advances, 5, 62603-62614, 2015.

[21] P. S. Shewale, N. K. Lee, S. H. Lee, K. Y. Kang, and Y. S. Yu, “Ti doped ZnO thin film based UV photodetector: Fabrication and characterization,” Journal of Alloys and Compounds, 624, 5, 251-257, 2015.

[22] B. Roul, R. Pant, S. Chirakkara, G. Chandan, K. K. Nanda and S. B. Krupanidhi, "Enhanced UV Photodetector Response of ZnO/Si With AlN Buffer Layer," in IEEE Transactions on Electron Devices, vol. 64, no. 10, pp. 4161-4166, Oct. 2017.

[23] Y. Duan et al., “ZnO thin film flexible UV photodetectors: regulation on the ZnO/Au interface by piezo-phototronic effect and performance outcomes,” Advanced Materials Interfaces, 1900470, 2019.

[24] Z. Zhang, Q. Liao, X. Zhang, G. Zhang, P. Li, S. Lu, S. Liu, and Y. Zhang, “Highly efficient piezotronic strain sensors with symmetrical Schottky contacts on the monopolar surface of ZnO nanobelts,” Nanoscale, 7, 1796-1801, 2015.

[25] W. Wu, and Z. Wang, “Piezotronics and piezo-phototronics for adaptive electronics and optoelectronics,” Nature Reviews Materials, 1, 16031 2016.

[26] Z. L. Wang, “The new field of nanopiezotronics,” Materials Today, 10, 5, 20-28, 2007.

[27] B. Wei, K. Zheng, Y. Ji, Y. Zhang, Z. Zhang, and X. Han, “Size-dependent bandgap modulation of ZnO nanowires by tensile strain,” Nano Letters, 12, 4595−4599, 2012.

[28] J. Nie, Y. Zhang, L. Li, and Jizheng Wang, “Piezo-phototronic effect enhanced photodetectors based on MAPbI3 perovskite,” Journal of Material Chemistry C, 8, 2709-2718, 2020.

[29] Y. Duan, S. Zhang, M. Cong, D. Jiang, Q. Liangb, and X. Zhao, “Performance modulation of a MgZnO/ZnO heterojunction flexible UV photodetector by the piezophototronic effect”, Journal of Material Chemistry C, 8, 12917-12926, 2020.

[30] C. Park, J. Lee, H.-M. Sob, and W. S. Chang, “An ultrafast response grating structural ZnO photodetector with back-to-back Schottky barriers produced by hydrothermal growth,” Journal of Material Chemistry C, 3, 2737-2343, 2015.

[31] W.C. Lien, D.S. Tsai, S.H. Chiu, D.G. Senesky, R. Maboudian, A.P. Pisano, and J.H. He, “Low-temperature, ion beam-assisted SiC thin films with antireflective ZnO nanorod arrays for high-temperature photodetection,” IEEE Electron Device Letters, 32, 1564-1566, 2011.

Chapter 6

Conclusion and Future Scope

The key objective of this research work is to analyse the different existing and emerging scopes of PD by analytically modelling and fabricating the PD. The analytical model is first time discussed and explored for wide bandgap semiconductor. The model highlighting the every aspects of the wide bandgap material based homojunction *p-i-n* PD is very limited.

The performance of the device in adverse thermal conditions are rarely explored for TMD materials and with this work authors have explored the variation of dark current for MoS_2 monolayer PD at different working temperature. The study propose the simple technique of surface assisted transfer dependent PD fabrication method. The sensitivity of the device for the entire visible spectrum is established by 2D TMD based PD.

The wearable and flexible electronics is current and future trend of semiconductor market globally and thermally stable flexible PD is studied here. The work open the inspiration for wideband wearable PD for health monitoring system and dosimetry application. An agile UV PD fabricated by reactive magnetron sputtered ZnO in an MSM configuration is evaluated under various device bending conditions, highlighting the UV PD's potential for different applications.

The major issues in these work are devolving an analytical model for *p-i-n* PD for wide band semiconductor; which was successfully resolved by suitable model development and verification. Moreover, analysing the MSM PD for future ready device are the key concern in the other works of this thesis.

6.1 Conclusions

The major conclusion of the work can be summarized as below:

- The analytical model access and estimate the performance of wide bandgap material for fabricating UV *p-i-n* PD of homojunction as well as heterojunction structure before actual fabrication of the PD.
- The model helps in optimising the thickness of the individual layers of *p-i-n* PD and helps in estimating the variation of the dark current and peak responsivity with varying reverse bias voltage.
- A detailed discussion of the various components of dark current and quantum efficiency of the *p-i-n* PD are summarized in the work.
- This research work also discusses a facile approach for the deposition of MoS_2 via CVD technique, followed by wet transfer process. The complete study of MoS_2 monolayer MSM device proves the potential of MoS_2 as a future optoelectronics material.
- The work discuss the spectral response of MoS_2 monolayer MSM PD for visible light spectrum with varying voltage.
- The study quantitatively estimate the detectivity and NEP with varying voltage of the MoS_2 monolayer device for the MSM device.
- The obtained value of the rise and fall time for the MoS_2 monolayer MSM PD is the least so far to the best of authors' knowledge.
- Reactive magnetron sputtered ZnO based flexible UV PD in MSM structure is investigated under various device bending conditions and which highlights the potential of the UV PD for wearable electronic applications.
- The device on the PI flexible substrate shows significant selectivity to the peak response wavelength even in the highest bending (strained) condition.
- The study analyse the effect of biased voltage with bending

condition to manipulate the performance of the flexible device.

- Various effects governing the physics of the flexible PD is discussed and investigation of the responsivity and temporal response of the PD is performed.

6.2 Future Scope

The following are the future work that can be focused:

- Fabrication of ZnO based *p*-*i*-*n* and quantum well homojunction UV PDs by using DIBS.
- Bandgap tailoring and analysis of incidence over intrinsic region of fabricated DIBS grown *p*-*i*-*n* UV PD.
- Characterizations and performance optimization of different PD structures based on emerging TMD materials.
- Fabrication of MoS_2 monolayer FET devices for photodetecting applications.
- Fabrication and investigation of ZnO/MoS_2 and MoS_2/WS_2 hybrid photodetector as broadband detector.
- Performance investigation of the noble metal doped MoS_2 PD.
- Analysis of flexible PD on different substrate for wearable electronic applications.
- Exploring the above discussed device structure over flexible substrate.
- Planning the commercial level fabrication and integration of the PD for dosimetry application and other UV monitoring systems.